Chemistry of Two-Dimensional Transition Metal Carbides (MXenes)

A Thesis

Submitted to the Faculty

of

Drexel University

by

Olha Mashtalir

in partial fulfillment of the

requirements for the degree

of

Doctor of Philosophy

June 2015

DEDICATIONS

To my beloved husband Sin and daughter Inanna who were my unfailing source of love, support and inspiration;

Mom and Dad whose encouragement has meant so much to me;

and my two kitties who were simply there to help me pass this writing endeavor

ACKNOWLEDGMENTS

I would like to sincerely thank my thesis advisors for all their help and guidance throughout my doctoral studies, Prof. Yury Gogotsi and Prof. Michel W. Barsoum, who introduced me to the fascinating world of two-dimensional materials. Thank you for being my mentors and my role models inside and outside of the lab. You gave me many opportunities to grow as a scientist, a professional and a person. You taught me to see the bigger picture and dream big, pursuing my goals, whatever it may take me.

I would like to thank my committee members: Dr. Steven May, Dr. Richard Knight, and Dr. Vivek Shenoy for taking time from their busy schedules to listen, guide and evaluate this work.

I would like to thank all the former and current members of Drexel Nanomaterials group and MXene group for their help. They all contributed to this work in countless ways, particularly Maria Lukatskaya, Michael Naguib, Michael Ghidiu, Mengqiang Zhao, Chang (Evelyn) Ren, Babak Anasori, Joseph Halim, Yohan Dallagnese, Boris Dyatkin, Kristy Jost, Yang Gao, Murat Kurtoglu, Ioannis Neitzel, Carlos Perez, John McDonough and others. I would especially like to thank Maria Lukatskaya and Boris Dyatkin for their friendship and support along the way. Separate thanks to Dr. Vadym Mochalin for the helpful discussions, and Martin Crowe for help with photocatalytic part of my research.

I give special thanks to the Drexel Nanomaterials Institute staff, particularly Wendy Thurman, Michelle Sipics, and especially Danielle Tadros Kopicko, for their patience and willingness to help. I am also very grateful to the staff members of Materials

Science and Engineering Department, particularly Keiko Nakazawa, Yenneeka Long, and Sarit Kunz, for their indispensable administrative support.

I thank the staff members of Drexel's Centralized Research Facility, Dmitri Barbash, Craig Johnson, and Ed Basgall, for their guidance and support with variety of characterization tools and analysis.

I would like to thank Prof. Patrice Simon for hosting me in his laboratory at Université Paul Sabatier (Toulouse, France); Prof. Masahiro Yoshimura for inviting me to his laboratory at National Cheng Kung University (Tainan, Taiwan) to participate in plasma research; Dr. Alex Bondarchuk for inviting me, training and helping with *in-situ* Raman study at CIC Energigune (Alava, Spain).

I would like to acknowledge the financial support of this work received from the Assistant Secretary for Energy Efficiency and Renewable Energy, Office of Vehicle Technologies of the U.S. Department of Energy under Contract No. DE-AC02-05CH11231, Subcontract 6951370 under the Batteries for Advanced Transportation Technologies (BATT) Program. Also, separate thanks to the Office of International Programs at Drexel University for the financial support for traveling to international conferences.

In addition, I want to thank to my former employer, Materials Research Center Ltd (Kyiv, Ukraine) and particularly Alexei Gogotsi, for opening the door for this opportunity of getting a PhD degree at Drexel University.

In conclusion, I would like to thank my family for all their love and support, especially my wonderful husband who has supported and encouraged me throughout my studies, my baby girl Inanna for being such a supportive low maintenance baby, my

mother for taking care of Inanna and keeping my sanity during the first few month after Inanna's birth.

TABLE OF CONTENTS

LIST OF TABLES

LIST OF FIGURES

LIST OF ABBREVIATIONS

AB80	acid blue 80
ACN	acetonitrile
Au-NPs	gold nanoparticles
CMA^+	cetyltrimethylammonium
CNTs	carbon nanotubes
CVD	chemical vapor deposition
DFT	density functional theory
DI water	deionized water
DMF	N,N-Dimethylformamide
DMSO	dimethylsulfoxide
EDX	energy dispersive X-ray spectroscopy
EMI-TFSI	1-ethyl-3-methylimidazolium bis(trifluoromethyl-sulfonyl)imide
HF	hydrofluoric acid
HM	hydrazine monohydrate
INS	inelastic neutron scattering
KOAc	potassium acetate
LiOAc	lithium acetate
MD	molecular dynamics
MB	methylene blue
NSLD	neutron scattering length density
ORNL	Oak Ridge National Laboratory
PC	propylene carbonate
PDF	pair distribution function
RT	room temperature
SAED	selected area electron diffraction

SANS	small-angle neutron scattering
SEM	scanning electron microscopy
SNS	Spallation Neutron Source
SSA	specific surface area
TEM	transmission electron microscopy
TBA^+	tetrabuthylammonium
TMA^+	tetramethylammonium
TGA	thermogravimetric analysis
THF	tetrahydrofuran
TMD	transition metal chalcogenide
TPD-MS	temperature programmed desorption mass spectroscopy
UFF	the Universal Force Field
XRD	X-ray diffraction
XPS	X-ray photoelectron spectroscopy
a-LP	*a*-lattice parameter
c-LP	*c*-lattice parameter
h-BN	hexagonal boronitride
i-PrA	isopropyl amine
2D	two-dimensional

ABSTRACT

Chemistry of Two-Dimensional Transition Metal Carbides (MXenes)

Olha Mashtalir

Advisor: Prof. Yury Gogotsi; Co-advisor: Prof. Michel W. Barsoum

With consumer trends pushing toward smaller, faster, more flexible, multitasking devices, researchers striving to meet these needs have targeted two-dimensional (2D) materials – and graphene in particular – as holding the most promise for use in advanced applications. But in 2011, a significant interest has been triggered by a newly discovered family of novel 2D materials – layered transitional metal carbides and carbonitrides, named MXenes. Those compounds were of general formula $M_{n+1}X_nT_x$, where M stands for metal atom, X is C and/or N, n = 1, 2 or 3, and T_x represents surface groups. Being initially suggested as a material for electrical energy storage systems, MXenes' properties and their potential applications have not been explored.

This work is the first complete study of MXenes' chemistry that sheds light on the chemical composition, structure and properties of these novel materials and possible routes of its modification. The research was focused on 2D titanium carbide, $Ti_3C_2T_x$, chosen as the representative of the MXene family. The kinetic study of $Ti_3C_2T_x$ synthesis discovered the main synthesis parameters, *viz.* temperature, time and particle size, that affect the etching process and define the quality of final product.

MXenes were found to be able to spontaneously accommodate various ions and small organic molecules between the layers leading to preopening of the structure. A major challenge of large scale production of delaminated, atomically thin 2D MXene

layers was solved with two delamination techniques involving dimethyl sulfoxide and isopropyl amine pre-intercalation followed by sonication in water.

$Ti_3C_2T_x$ was also found to possess adsorptive and photocatalytic properties, revealing its potential for environmental applications. It also showed limited stability in water and in the presence of oxygen, providing important practical information on proper handling and storage of MXene materials.

Completion of this work allowed the performance of energy storage devices to be improved significantly, *viz.* Li-ion batteries and electrochemical capacitors, and gave rise to many other potential applications such as MXene-polymer composites, sorption, and catalysis. More importantly, it opened a path to the large-scale synthesis of thin, single-layer MXene sheets and led to establishing MXenes as fully-fledged members of the growing family of 2D materials.

CHAPTER 1: INTRODUCTION

Over the last decade, 2D materials have attracted increasing attention due to their unique properties, with potential applications in pseudo- and double-layer capacitors [1], Li-ion batteries [2-4], and transistors [5, 6] among many others. Compared to bulk layered materials, 2D single layers exhibit higher specific surface areas and unique electronic, mechanical, optical and magnetic properties. These characteristics open up new 2D systems for exploration.

The most studied 2D material to date is graphene [7]. In 2004, Geim and Novosolov showed that graphite can be exfoliated into single atomic layers of graphene simply by using Scotch^{TM} tape, demonstrating the thinnest electronic device in scientific history. The interest in this material was further boosted when the Nobel prize was awarded for that discovery in 2010. Graphene is finding its way in many applications, from supercapacitor electrodes [1] to reinforcement in composites [8]. However, its simple chemistry and its propensity to oxidize, limits its use.

Beyond graphene, there are many other types of 2D materials of different chemistries. Those include but are not limited to hexagonal boronitride (*h*-BN), transition metal chalcogenides (TMDs), metal oxides and hydroxides among others. Similar to graphite, their multilayered counterparts have strong in-plane chemical bonds but weak out of plane Van der Waals, hydrogen and/or electrostatic bonding, and therefore the potential to be exfoliated into nanosheets. Their chemical diversity provides a large number of compositional variables that can be tuned for achieving specific properties.

A unique characteristic of those materials is their ability to accommodate various ions and molecules between their layers, a phenomenon known as intercalation. Intercalated compounds of inorganic hosts (graphite [9], clays, TMDs, etc.) have also gained renewed interest due to their unique chemical properties and physical characteristics [10-14]. De-intercalation of those compounds under certain conditions (*e.g.*, thermal shock, sonication or volume expansion reactions in the interlayer space) can sometime lead to their separation into atomically thin 2D layers of graphene [1, 15-18] and other materials [19-22].

The presence of weak interactions between the layers of the compounds is not a limiting factor any longer since the separation of nanosheets of strongly covalently/ionically bonded ternary carbides and carbonitrides, known as MAX phases, has been reported [23, 24]. The resulting compounds – MXenes – showed similar to exfoliated graphite structure, comprised of stacks of 2D early transitional metal carbides and carbonitrides of general formula $M_{n+1}X_nT_x$, where M stands for a metal atom, X stands for C and/or N, n = 1, 2 or 3, and T_x represents various surface terminations (OH, O and/or F groups). Since the discovery of the first MXene in 2011, this new family of layered compounds has been a hot research topic in the scientific community. It was initially proposed as an electrode material for Li-ion battery [25-27]. However, MXenes' properties and, consequently, potential applications are far from being fully explored.

Overall, the world of 2D materials is huge and its investigation has just started. Considering the potential of novel systems, many of which are unexplored still, for energy storage, electronic and structural applications, their exploration becomes central to nanotechnology for the 21st century.

CHAPTER 2: BACKGROUND AND LITERATURE SURVEY

2.1. Two-Dimensional Materials

Striving to meet the needs of the modern world, various 2D materials (Figure 1) have been targeted as holding the most promise for use in advanced applications. Graphene – a single hexagonal layer of sp^2 bonded carbon atoms – is a certain leader among others for the last decade. Its superior electron mobility of 2.5×10^5 $cm^2V^{-1}s^{-1}$ [28], high thermal conductivity (above 3,000 W mK^{-1} [29]), a Young's modulus of 1 TPa and intrinsic strength of 130 GPa [30], and the ability to adsorb white light [31] make graphene a desirable material for energy storage, electronic and optoelectronic applications, among others.

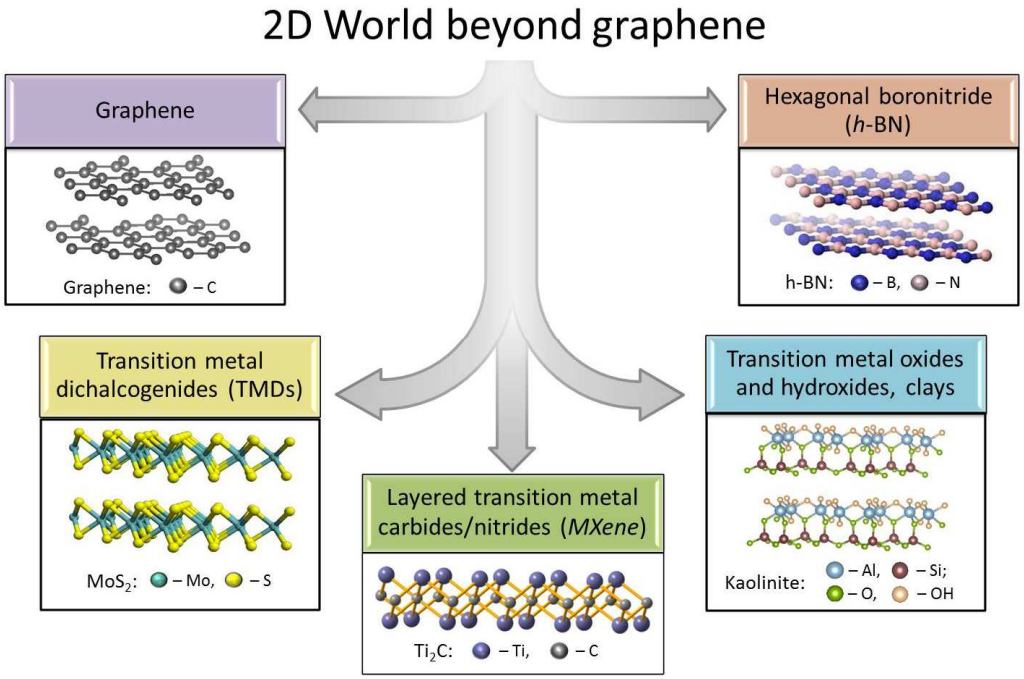

Figure 1. *Existing two-dimensional materials and their structures.*

Various other materials have been of a great interest to the research community (Figure 1). Those include *h*-BN [32], TMDs (MoS_2, WSe_2, *etc*.) and metal halides (CdI_2, $MgBr_2$, etc.) [19, 33]; layered metal oxides (*e.g*., MnO_2, MoO_3, $LaNb_2O_7$) and layered double hydroxides (*e.g.,* $Mg_6Al_2(OH)_{16}$) [13, 34]; layered silicates, or clays [35], and others. Each class of material exhibits certain exceptional properties, different from their multilayered counterparts. For example, bulk MoS_2 is an indirect-band-gap semiconductor (~1.2 eV). However, single-layered MoS_2 has a direct-band gap (~1.9 eV) and exhibits a strong photoluminescence that is absent in bulk that makes it a promising material for nanoelectronics and photoelectronics [22]. Excellent mechanical properties also make MoS_2 nanosheets attractive for flexible electronic devices' fabrication or in applications such as reinforcing elements in composites. Unlike MoS_2, single-sheet *h*-BN does not change its band gap greatly and remains highly insulating (~5.97 eV) [36], but possesses a high thermal conductivity, chemical stability, and mechanical strength [37]. This suggests potential applications of *h*-BN monolayers as fillers for composites, thermal radiators, ultraviolet-light lasers and emitter devices, etc.

A number of routes that can produce atomically thin monolayers of the above mentioned 2D materials, have been reported. The best known methods are micromechanical cleavage, chemical vapor deposition (CVD), liquid chemical exfoliation, surface-assisted epitaxial growth [38]. Each process has its pros and cons. For example, micromechanical cleavage is an easy and fast method to produce high quality isolated planes, but can only be used for weakly bonded layered materials (for instance, graphite, TMDs, *h*-BN [15]), is limited in size to its multilayered counterpart and cannot produce large quantities of 2D materials. In contrast, CVD method, reported

for the synthesis of graphene, *h*-BN [39], MoS_2, [40], and others, can easily produce large-area 2D thin sheets but the process is experimentally complicated and very costly.

Wet chemical exfoliation of layered compounds is probably the most commonly used method to produce single nanosheets [19, 41]. The method is cheap by itself but the quality and quantity of the product is not the best. The success of exfoliation is defined by interfacial processes that occur between layer surfaces and solvent or intercalant (electric double layer formation, osmosis, ion diffusion, capillary effects, *etc*.), and stabilization of monolayer dispersion.

Nicolosi *et al*. [41] outlined the main mechanisms of liquid chemical exfoliation (see schematic in Figure 2). Those are strongly affected by various factors, both intrinsic

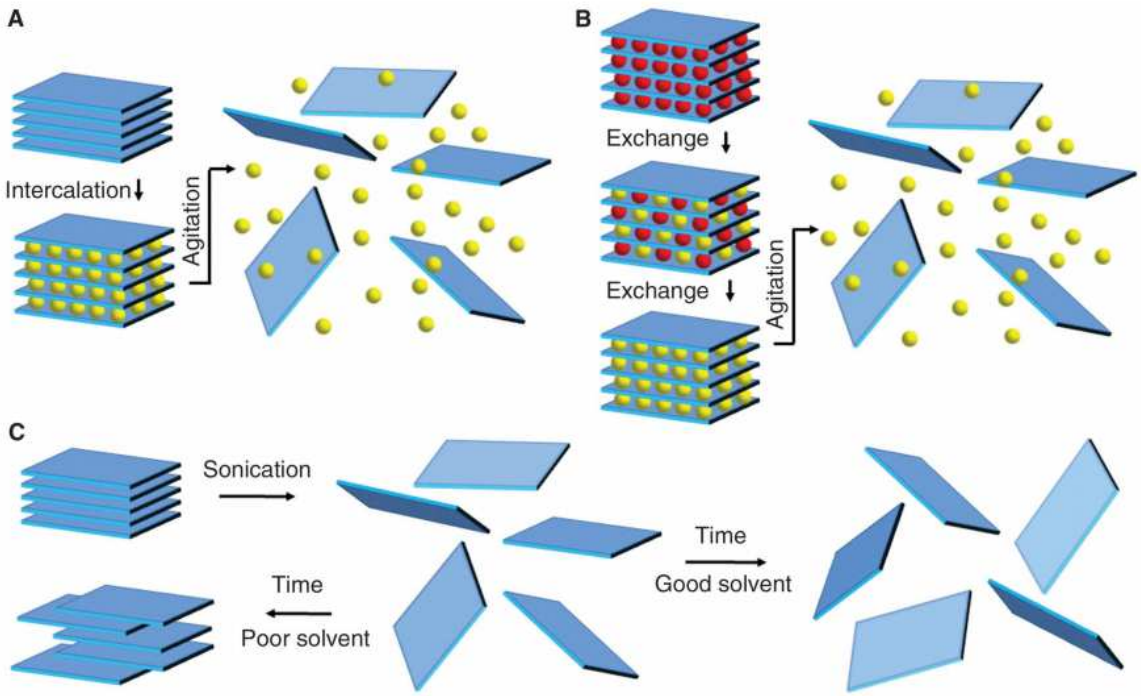

Figure 2. *Schematic of main liquid exfoliation mechanisms. (**A**) Intercalation followed by agitation. (**B**) Ion exchange in a liquid environment followed by agitation. (**C**) Sonication-assisted exfoliation in a solvent. [41]*

(*e.g.*, composition of multilayered compounds, surface charge density, nature of guest species between the layers, *etc.*) and extrinsic (properties of solvent such as polarity, dielectric, etc.). Thus, many layered compounds, such as graphite, *h*-BN, TMDs [19, 42], can be easily exfoliated in suitable solvents upon sonication (Figure 2C). They also readily intercalate various molecules, which can weaken the interlayer bonding, increase the interlayer distances and lead to exfoliation upon subsequent treatment such as thermal shock or sonication (Figure 2A) [16, 22, 43]. Finally, compounds which contain exchangeable interlayers of counterions (*e.g.*, layered oxides and hydroxides [2, 13], clays [44]) can be delaminated through ion exchange with larger ions leading to swelling and further exfoliation with, or without, additional force (Figure 2B).

2.2. MAX Phases

The MAX phases, a group of ternary carbides and nitrides are a relatively new class of hexagonal-structure (space group $P6_3/mmc$) materials with a general formula $M_{n+1}AX_n$ (n = 1 to 3), where M is an early transition metal, A an A-group (mostly groups 13 and 14) element, and X is C and/or N (Figure 3A) [45-47]. They correspond to a family of layered materials with more than 70 members, which possess an unusual combination of properties, exhibiting some characteristic of ceramics and others of metals. For example, some show resistance to oxidation and corrosion, high thermal stabilities, and are elastically stiff, but at the same time are readily machinable, thermally and electrically conductive, resistant to thermal shock and ductile at elevated temperatures [45, 48, 49].

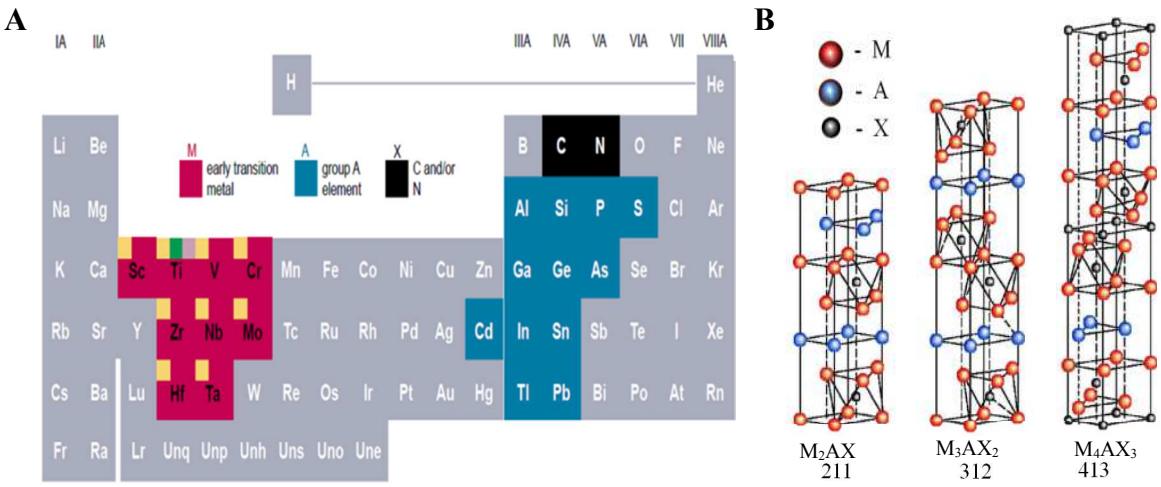

Figure 3. *(**A**) Elements in the periodic table (top) that react together to form the MAX phases. The red squares represent the M-elements; the blue, the A elements and black or X is C and/or N. (**B**) Unit cells of 211, 312 and 413 MAX phases.[46]*

Due to their layered nature and the fact that basal plane slip is operative at all temperatures [50], the MAX phases possess unique mechanical properties that are atypical for structural ceramics. The fracture toughness of Ti_3SiC_2 varies from 8-16 $MPa \cdot m^{1/2}$ which is one of the highest values ever reported for a single-phase, monolithic ceramic. Such good damage tolerance is attributed in part to kinking and the formation of the heavily deformed lamellar bridges in the crack wake that are reminiscent of those that form in layered composites [51].

Mechanical deformation of the MAX phases – which is mediated by basal dislocations and is very anisotropic - can lead to partial delamination and the formation of lamellae with thicknesses that range from tens to hundreds of nanometers [52]. However, mechanical exfoliation into single sheets would be difficult since the M-A bonds are, on an absolute scale, quite strong. For example, the decomposition temperature of many MAX phases is > 1400 °C.

Structurally, the MAX phases include two formula units per unit cell (Figure 3B) [45]. In each case near close-packed layers of the M atoms are interleaved with layers of the pure group A-element, with the X-atoms filling the edge, sharing octahedral sites between the former. The A-group elements are located at the centers of trigonal prisms that are larger than the octahedral sites and thus better able to accommodate the larger A-atoms. Depending on the number of M-layers separating the A-layers, they can be classified into 3 groups: 211, 312 and 413 corresponding to 2, 3 and 4 M-layers, respectively (Figure 3B).

MAX phases have the metallic-like nature of the bonding, combining the strong covalent M-X bonds together with relatively weak ionic M-A bonds [45]. As a result, the A-element atoms are much more reactive than the M and X atoms. Thus, Si was extracted from Ti_3SiC_2 structure by heating the MAX phase in a C-rich atmosphere [53] following the reaction:

$$Ti_3SiC_2 + (3x-2)C \rightarrow 3TiC_x\ (x<0.8) + Si. \quad (1)$$

Another example of Si removal from Ti_3SiC_2 was placing the MAX phase in molten cryolite [54] or molten aluminum [55], which also resulted in the formation of TiC_x. The following reactions were suggested as those happening at the Al/Ti_3SiC_2 interface:

$$Ti_3SiC_2 + Al_{(l)} \rightarrow 3TiC_x + Si(Al), \text{ and} \quad (2)$$

$$TiC_x + 3y\ Al \rightarrow y\ TiAl_3 + Ti_{(1-y)}C_x, \quad (3)$$

where Si was the material that dissolved in the molten Al and *x* was most probably ca. 0.67. Unlike Si, In was removed from the Ti_2InC structure simply by heating in vacuum at ~800 °C [56]. All the above mentioned processes led to a structural transformation from a hexagonal to a cubic lattice and a partial loss of layering. It was also reported that

not only the A-element but also the M-element could be removed from MAX phases by high-temperature chlorination resulting in the formation of a porous carbon known as carbide-derived carbon [56, 57]. Two years ago, selective etching of Al from T_3AlC_2 at room temperature (RT) with no structural transformations or damage of initial layered structure was reported [23]. It was a turning point toward establishing a new large family of 2D materials, known as *MXenes*.

2.3. MXenes

MXene is the common name for a large class of 2D layered carbides first synthesized in 2011 [23]. The first MXene was produced based on one of the most widely studied MAX phases: Ti_3AlC_2 [58]. This phase was discovered and first synthesized by Pietzka and Schuster [59]. As mentioned before, with respect to the M-X bonds, the M-A bonds are *relatively* weak. It follows that in Ti_3AlC_2, the Al atoms could be readily removed from the MAX structure as the most reactive species. It was shown that immersing Ti_3AlC_2 powders in a 50 wt.% aqueous hydrofluoric acid (HF) solution at RT for 2 h resulted in the complete selective etching of the Al layers according to the following reaction [23]:

$$Ti_3AlC_2 + 3HF = AlF_3 + 3/2H_2 + Ti_3C_2 \quad (4)$$

A schematic of the process is shown in Figure 4. In contrast to the MAX phases, which are 3-D crystals with chemical bonds between all atoms, MXene is made of stacked sheets (Figure 5D) of composition M-X with no chemical bonds between the sheets. Similar to “graphene” or “graphene oxide”, the name MXene refers to the class of materials that may have different surface terminations, reflecting the most distinctive

characteristic of the class – layered structures with weak interactions between the layers.

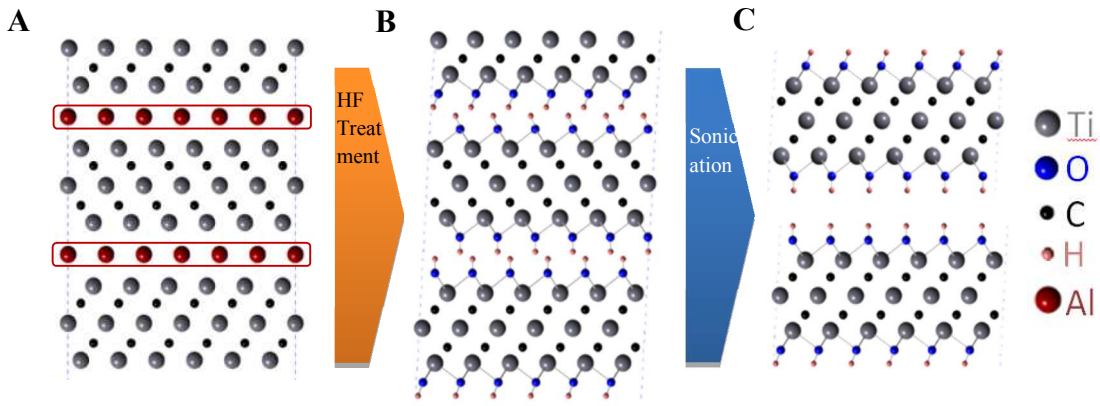

Figure 4. *Schematic of the exfoliation process for Ti_3AlC_2. (**A**) Ti_3AlC_2 structure. (**B**) Al atoms are replaced by OH after reaction with HF. (**C**) Breakage of the hydrogen bonds and separation of $Ti_3C_2T_x$ MXene nanosheets after sonication in methanol. [23]*

As evidence of MAX phase exfoliation by HF treatment, the majority of the X-ray diffraction (XRD) peaks – notably the most intense peak at $2\theta \approx 39°$ – associated with Ti_3AlC_2 (bottom curve in Figure 5A) disappeared (blue curve in Figure 5A) [23]. Comparing simulated XRD patterns of hydroxylated, $Ti_3C_2(OH)_2$ (red curve in Figure 5A) and fluorinated, $Ti_3C_2F_2$, (green curve in Figure 5A), it was clear that both simulated structures were in good agreement with the XRD patterns of the sample after HF treatment suggesting OH and F termination of the Ti_3C_2 surface. It was also shown that sonication of the reaction products for 5 min resulted in weakening of the 312 peaks and the appearance of a broad amorphous band at $2\theta \approx 24°$ (top spectrum in Figure 5A) that suggested that structural disorder occurred and delamination of single flakes was possible.

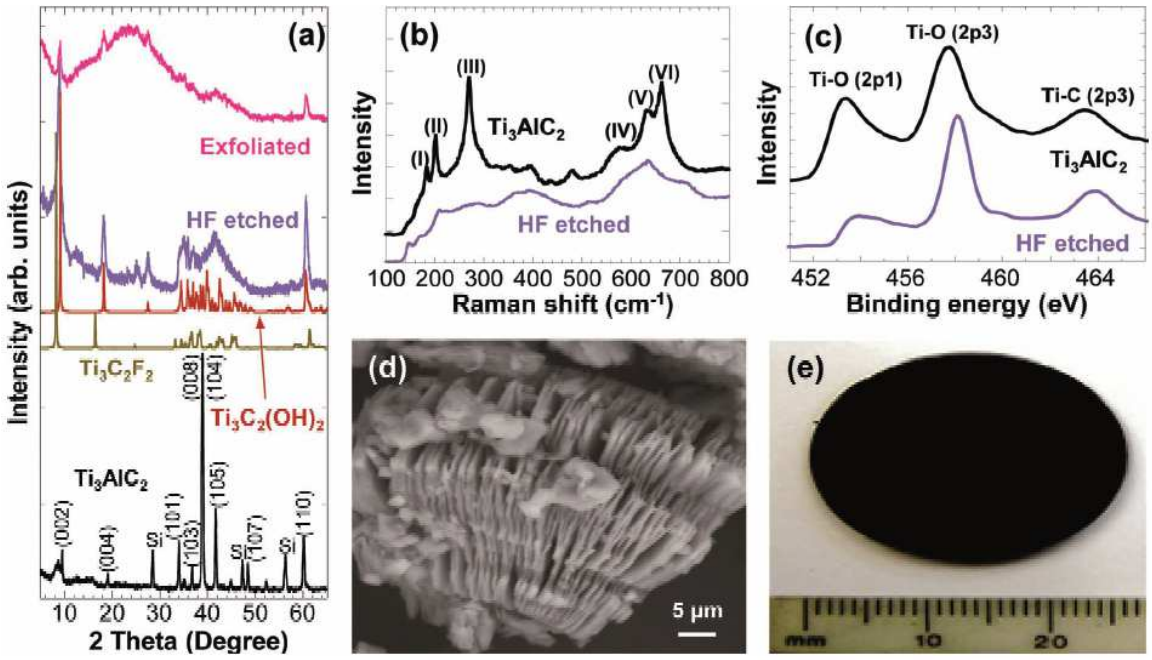

Figure 5. *Analysis of Ti_3AlC_2 before and after exfoliation. (**A**) XRD pattern for Ti_3AlC_2 before HF treatment, simulated XRD patterns of $Ti_3C_2F_2$ and $Ti_3C_2(OH)_2$, measured XRD patterns of Ti_3AlC_2 after HF treatment, and exfoliated nanosheets produced by sonication. (**B**) Raman spectra and (**C**) XPS spectra of Ti_3AlC_2 before and after HF treatment. (**D**) SEM image of a sample after HF treatment. (**E**) Cold-pressed 25 mm disk of etched and exfoliated material after HF treatment. [23]*

Raman spectroscopy also confirmed etching of Al out of Ti_3AlC_2 structure by the disappearance of peaks I, II, and III after HF treatment, while peaks V and VI merged, broadened and downshifted (Figure 5B) [23, 60]. The disappearance of the first three peaks was consistent with the assignment of these modes to the Ti-Al bonding. The emergence of modified peaks V and VI was also consistent with the assignment of these modes to the Ti-C bond vibrations. Such downshifting observed for the latter peaks has also been seen in Raman spectra of very thin layers of inorganic layered compounds [61]. The line broadening and spectral shifts in the Raman spectra were consistent with exfoliation, and were in agreement with the broadened XRD profiles.

In order to define the surface chemistry, X-ray photoelectron spectroscopy (XPS)

spectra, before and after treatment (Figure 5C), showed the presence of Ti-C and Ti-O bonds, indicating $Ti_3C_2(OH)_2$ formation after treatment. The O1s main signal found at ~530.3 cm^{-1} suggested the presence of OH groups [62]. The Al and F peaks were observed and assigned to the remains of unwashed AlF_3 and/or F-surface termination.

Transmission electron microscopy (TEM) confirmed the exfoliation of single MXene sheets by sonication in methanol showing thin electron transparent flakes [23]. Selected area electron diffraction (SAED) showed the hexagonal symmetry of the basal planes. The experimentally observed interplanar distances and angles were found to be in good agreement with a simulated structure of two adjacent OH-terminated Ti_3C_2 sheets structure [23]. Energy dispersive X-ray spectroscopy (EDX) also showed the presence of Ti, C, O, and F.

Based on the aforementioned results, it was concluded that the exfoliated 2D Ti_3C_2 layers were *not* M-terminated, but most probably covered with oxygen-containing groups, such as OH, and/or fluorine, F, introduced after etching with HF [23] according to:

$$Ti_3C_2 + 2H_2O = Ti_3C_2(OH)_2 + H_2 \quad (5)$$

and possibly

$$Ti_3C_2 + 2HF = Ti_3C_2F_2 + H_2 \quad (6)$$

Reactions (5) and (6) are simplified in that the assumption was that the terminations were OH or F, respectively, when it most probably was a combination of both. In fact, the chemistry of exfoliated MXene produced by HF etching of Ti_3AlC_2 was much closer to $Ti_3C_2(OH)_xO_yF_z$ than to Ti_3C_2. However, for brevity's sake, $Ti_3C_2T_x$ where T_x stands for surface termination was used instead of the more cumbersome chemical formula.

Overall, exfoliation of 9 MXenes of different groups has been reported [24] – 211 group: Nb_2C, V_2C, Ti_2C, TiNbC; 312 group: Ti_3C_2, Ti_3CN, $(V_{0.5}Cr_{0.5})_3C_2$; and 413 group: Nb_4C_3, Ta_4C_3. Similar to $Ti_3C_2T_x$, the A-element was etched out of corresponding Al-containing MAX phase structures by HF treatment under different conditions forming both electron and optically transparent sheets (see Ta_4C_3 and Ti_3CN_x in Figure 6 as an example). All of the exfoliated MXenes, including the previously reported $Ti_3C_2T_x$ [23], are, in many aspects, graphene-like, forming stacks of sheets and scrolls.

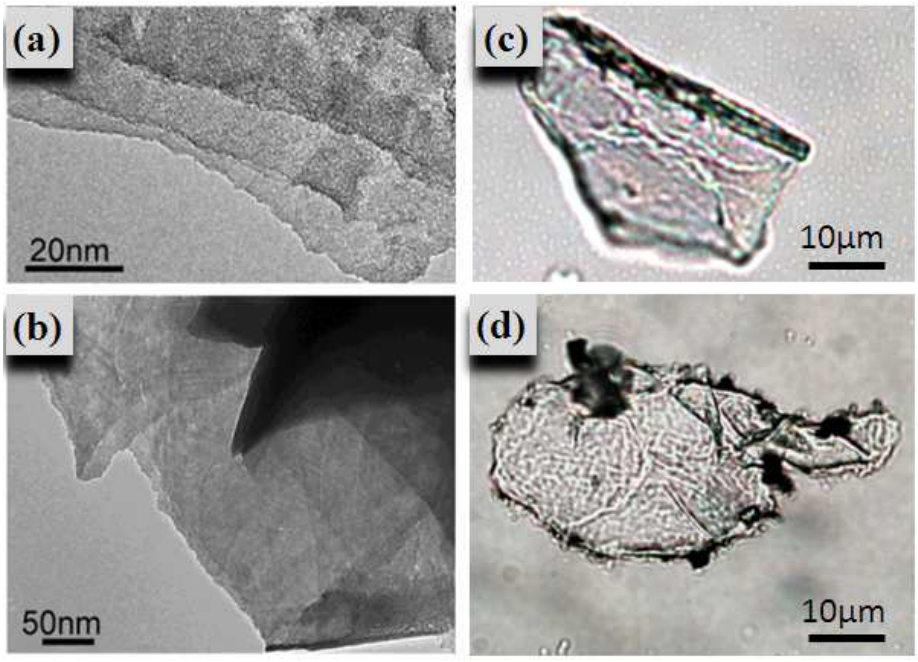

***Figure 6**. TEM images (**A** and **B**) and transmitted light micrographs (**C** and **D**) of exfoliated flakes of Ta_4C_3 and Ti_3CN_x, respectively. [63]*

Interestingly, the exfoliated particles maintained the pseudo-ductility of MAX phases and were easily cold pressed into freestanding disks ≈ 300 μm thick (see cold-pressed disc of $Ti_3C_2T_x$ in Figure 5E as an example). This property should prove crucial

in some potential applications, *e.g.* anodes for Li-ion batteries. Computational studies showed that they are expected to have high elastic moduli c_{11} (from 512 GPa for $Ti_4C_3T_x$ up to 788 GPa for Ta_2CT_x) [64]. They also are good electrical conductors showing sheet resistivity in the range of 22-339 Ω/□ (or 0.005-0.068 Ω·m) comparable to multilayer graphene [23, 24, 65-67]. Electrochemical intercalation of Li ions between the MXene sheets renders these solids promising materials for Li-ion battery anodes and hybrid electrochemical capacitors [25-27].

Surface chemistry of MXenes is of crucial importance for determining their properties and, consequently, potential applications. Thus, independent computational studies showed that all the bare MXene monolayers were metallic whereas most of the surface functionalized MXenes were semiconducting [23, 27, 67, 68]. In the same time, the scrolled nanotubes of $Ti_2C(OH)_2$ were predicted to have metallic-like characters while their monolayered analogs demonstrated either metallic-like or semiconducting behaviors depending on the arrangement of the surface OH groups [67]. Moreover, the bare Ti_3C_2 and OH-, F- and O-functionalized Cr_2C and Cr_2N were predicted to be magnetic [23, 68]. Such metallic and narrow-band semiconducting behavior suggests a good intrinsic conductivity, and hence favors their potential application as Li-ion battery electrode materials. At the same time, OH surface groups could be a reason for the decrease of capacity of Li-ion battery due to an irreversible reaction with electrolyte [25].

Overall, MXenes are promising new 2D layered materials with many exciting potential applications, but very little has been done to explore its properties experimentally. The study of MXenes is in its infancy with many questions, such as structure, properties, mechanisms involved in processing, still unanswered. Answering

those questions is of a great importance in order to establish MXenes as fully-fledged members of the growing family of 2D materials.

CHAPTER 3: MATERIALS AND METHODS

In this chapter information on the materials used in this work is presented; experimental procedures for MXene synthesis and chemical modification techniques are described in detail; characterization methods are presented together with technical details of analysis performed. Programs and theories used for theoretical predictions and simulations are also discussed.

3.1. Synthesis of MXene

Powder of Ti_3AlC_2 was prepared by ball-milling Ti_2AlC (> 92 wt.%, 3-ONE-2, Voorhees, NJ, USA) and TiC (99 %, Johnson Matthey Electronics, New York, NY, USA) powders in a 1:1 molar ratio for 24 h using zirconia balls [23]. The mixture was heated to 1350 °C for 2 h under argon, Ar. The resulting loosely held compact was crushed using a mortar and pestle. Hydrofluoric acid (HF, 48-51 wt.%) (Acros Organics, Morris Plains, NJ, USA) was used for etching of the synthesized MAX phase. All reagents and materials involved were used as-received, without further purification.

To investigate the kinetics of Al etching from Ti_3AlC_2, non-sieved Ti_3AlC_2 powders were immersed in HF solutions for various times and temperatures, as summarized in Table 1.

Table 1. *List of HF treatment runs carried out. In all cases the solution was a 50 wt.% HF.*

Run number	Time (h)	Temperature (°C)	Particle size (μm)
1.1	2	Room temperature (RT)	non-sieved
1.2	6	RT	non-sieved
1.3	10	RT	non-sieved
1.4	15	RT	non-sieved
1.5	19	RT	non-sieved
2.1	2	30	non-sieved
2.2	2	35	non-sieved
2.3	2	40	non-sieved
2.4	2	50	non-sieved
2.5	2	65	non-sieved
3.1	2	RT	< 38
3.2	2	RT	38 – 53

In order to study the effect of particle size on the exfoliation kinetics, one experiment involved the separation of powders into three fractions using sieves with openings of 38 μm and 53 μm. The fraction that passed through the 53 μm, but was retained by the 38 μm openings – i.e. with a mean particle size of ≈ 45 μm – was immersed in HF for 2 h at RT. The latter procedure was used to synthesize $Ti_3C_2T_x$ for all further experiments, not related to the kinetics study.

Table 2. *Summary of etching conditions for different MXenes using HF.*

MAX structure	MXene	MAX phase	Time (h)	HF conc. %	Temperature (°C)
211	Ti_2CT_x	Ti_2AlC	10	10	RT
	Nb_2CT_x	Nb_2AlC	48	50	55 ˚C
	V_2CT_x	V_2AlC	8	50	RT
	$(Ti_{0.5}Nb_{0.5})_2CT_x$	$(Ti_{0.5}Nb_{0.5})_2AlC$	28	50	RT
312	$Ti_3C_2T_x$	Ti_3AlC_2	2	50	RT
	Ti_3CNT_x	Ti_3AlCN	18	30	RT
413	$Ti_4C_3T_x$	Ti_4AlC_3	72	50	RT
	$Nb_4C_3T_x$	Nb_4AlC_3	90	50	RT

A summary of the synthesis conditions for different MXenes, including $Ti_3C_2T_x$, used in this work for comparison and/or proof of a concept is given in Table 2.

In all cases, after immersion in the HF solution for predetermined times (Table 2), the resulting MXene suspensions were repeatedly washed with deionized (DI) water water and centrifuged at 3500 rpm until the pH reached ~ 5. After decanting, the MXene was washed with ethanol (190 proof, Decon Laboratories, Inc., King of Prussia, PA) using a vacuum filtration setup and polyester membranes (47 mm diameter, 3.0 μm pore size, Osmonics Inc., Minnetonka, MN, USA). The latter was dried in a desiccator under vacuum, created by a water jet pump (the pressure in the desiccator was < 10 Torr) at RT for 24 h or in a vacuum oven (~10^{-2} Torr) at 100 °C for 22 h, placed into capped glass vials and stored in a desiccator at RT for further experiments.

3.2. MXene Modification

3.2.1. Intercalation

3.2.1.1. Intercalation with Hydrazine Monohydrate

To intercalate multilayered $Ti_3C_2T_x$ with hydrazine monohydrate, HM ($N_2H_4 \cdot H_2O$, > 98.0 wt.% purity, TCI America, Portland, OR, USA), the MXene powder was suspended either in HM or a 1:3 mixture of HM and DMF, and stirred for 24 h using a magnetic stirrer, either at RT or at 80 °C. Two types of powders were used: i) as-received, washed, wet $Ti_3C_2T_x$ and, ii) the powder prepared as in (i) and additionally dried in a desiccator under vacuum, created by a water jet pump (the pressure in the desiccator was < 10 Torr) at RT for 24 h or in a vacuum oven (~10^{-2} Torr) at 100 °C for

22 h. The weight ratio of HM:MXene was 10:1. When the treatment involved only HM, the suspensions were filtered and washed with ethanol. In the case of intercalation with HM/DMF mixture, DMF was used for washing instead of ethanol to avoid cross-contamination. The powders were then dried in a desiccator under vacuum (< 10 Torr) at RT for 24 h or in a vacuum oven (~10^{-2} Torr) at 120 °C for 24 h.

Following the same procedure, the intercalation of other multilayered MXenes – Ti_3CNT_x, $TiNbCT_x$, $Ta_4C_3T_x$ – with HM was attempted. The initial powders were previously dried in a desiccator under vacuum (< 10 Torr) at RT for 24 h; then suspended in HM in the weight ratio of HM:MXene of 10:1, stirred for 24 h using a magnetic stirrer at RT, filtered and washed with ethanol, and dried in a desiccator under vacuum (< 10 Torr) at RT.

To de-intercalate hydrazine and/or DMF, the intercalated $Ti_3C_2T_x$ powder was carefully weighed, placed in a graphite crucible and outgassed at RT in vacuum (~10^{-6} Torr) for 24 h. While under vacuum, the powder was heated to 200 °C at 10 °C/min, held at this temperature for 72 h, and cooled to RT. The powder remained under vacuum for another 48 h before it was retrieved. Between its removal from the furnace and re-weighing, the sample was exposed to ambient air for ~ 3 min.

3.2.1.2. Intercalation with Organic Compounds

After discovering the intercalation of HM into $Ti_3C_2T_x$, various neutral organic compounds of different polarity and molecular size (see a list of compounds and related information on purity and manufacturer in Table 3; see also Table 16) were chosen to understand the basic principles of MXene intercalation.

Table 3. *A list of organic chemical compounds used for intercalation.*

Organic compound (abbreviation, if any)	Chemical formula	Purity	Manufacturer
Acetic acid	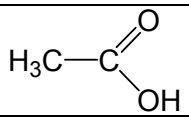	99.8%	Acros Organics, Fair Lawn, NJ, USA
Acetone	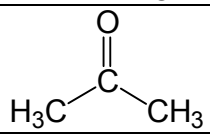	(≥ 99 wt.%	Acros Organics, Morris Plains, NJ, USA
Acetonitrile (ACN), anhydrous	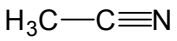	99.8 wt.%	Sigma Aldrich, St. Louis, MO, USA
Chloroform (stabilized in 0.5-1 % ethanol)	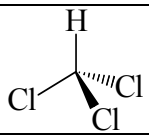	99.8 wt.%	Sigma Aldrich, St. Louis, MO, USA
Dimethylsulfoxide (DMSO)	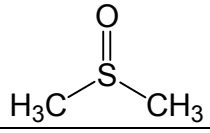	≥ 99.7 wt.%	Fisher Scientific, Fair Lawn, NJ, USA
Ethyl alcohol	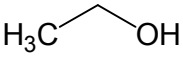	95 wt.%	Decon Laboratories, Inc., King of Prussia, PA, USA
Formaldehyde (stabilized with 10 to 15 wt.% methanol)	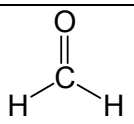	37 % w/w	Fisher Chemical, Fair Lawn, NJ, USA
Hexane	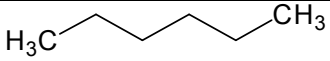	≥ 99 wt.%	Reagent Plus, Sigma Aldrich, St. Louis, MO, USA
Isopropyl amine (i-PrA)	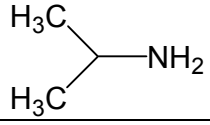	≥ 99.5 %	Sigma Aldrich, St. Louis, MO, USA
1-Methyl-2-pyrrolidinone	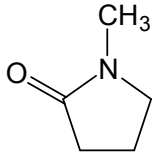	99.95 wt.%	Alfa Aesar, Ward Hill, MA, USA
N,N-Dimethyl-formamide (DMF)	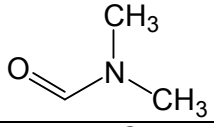	≥ 99 wt.%	Acros Organics, Morris Plains, NJ, USA
Propylene carbonate (PC), anhydrous	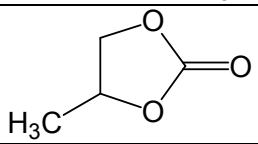	99.7 wt.%	Acros Organics, Morris Plains, NJ, USA

Tetrahydrofuran (THF)	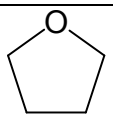	≥ 99 wt.%	Acros Organics, Morris Plains, NJ, USA
Thiophene	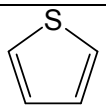	≥ 99 wt.%	Sigma Aldrich, St. Louis, MO, USA
Toluene	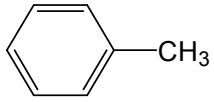	99.9 wt.%	Fisher Chemical, Fair Lawn, NJ, USA
Urea	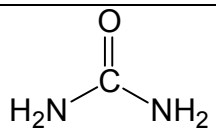	> 99 wt.%	Fisher Scientific, Fair Lawn, NJ, USA

Note: All chemicals were used as received without further purification.

To intercalate $Ti_3C_2T_x$ with above listed compounds, its powder was dried in a desiccator under vacuum (< 10 Torr) at RT for 24 h. In all cases the intercalation procedure was the same: i) 0.3 g of $Ti_3C_2T_x$ were mixed with 5 ml of each of the organic compounds listed below (excluding urea), then stirred for 24 h at RT; ii) in the case of urea, 5 ml of a 50 wt.% aqueous solution of urea was added to 0.3 g of $Ti_3C_2T_x$ and stirred for 24 h at 60 °C. Afterwards, the resulting colloidal solutions were filtered and dried in a desiccator under vacuum (< 10 Torr) at RT.

3.2.1.3. Intercalation with Ionic Compounds

The possibility of MXene intercalation with ionic compounds was studied. For this, various ionic chemicals (see list in Table 4) of different ion size, charge (mono- and multivalent), and nature (organic and inorganic; acidic, neutral and basic when dissolved in DI water) were chosen.

Table 4. *A list of ionic chemical compounds used for intercalation.*

Organic compound (abbreviation, if any)	Formula	Purity	Manufacturer
Ammonium hydroxide	NH_4OH	28-30 wt.% in water	Fisher Scientific, Fair Lawn, NJ, USA
Ammonium tetrafluoroborate	NH_4BF_4	97 %	Alfa Aesar, Ward Hill, MA, USA
Aluminum chloride	$AlCl_3$	> 95 %	Alfa Aesar, Ward Hill, MA, USA
Cetyltrimethylammonium (CMA) bromide	$(C_{16}H_{33})(CH_3)_3N$ Br	≥ 99 %	Sigma Aldrich, St. Louis, MO, USA
1-ethyl-3-methylimidazolium bis(trifluoromethyl-sulfonyl)imide (EMI-TFSI)	$C_8H_{11}F_6N_3O_4S_2$	≥ 97 %	Sigma Aldrich, St. Louis, MO, USA
Lithium acetate anhydrous (LiOAc)	CH_3COOLi	≥ 99 %	Acros Organics, Fair Lawn, NJ, USA
Magnesium sulfate	$MgSO_4$	≥ 99.5 %	Alfa Aesar, Ward Hill, MA, USA
Potassium acetate (KOAc)	CH_3COOK	ACS reagent grade	MP Biomedicals, LLC, Solon, OH, USA
Potassium hydroxide	KOH	≥85.0%	Fisher Chemical, Fair Lawn, NJ, USA
Potassium sulfate	K_2SO_4	certified ACS crystalline	Fisher Scientific, Fair Lawn, NJ, USA
Sodium acetate anhydrous	CH_3COONa	≥ 99.0 %	Alfa Aesar, Ward Hill, MA, USA
Sodium carbonate, anhydrous	Na_2CO_3	≥ 99.0 %	Fisher Chemical, Fair Lawn, NJ, USA
Sodium citrate tribasic dihydrate	$HOC(COONa)(CH_2COONa)_2 \cdot 2H_2O$	> 98 %	Sigma Aldrich, St. Louis, MO, USA
Sodium formate	HCOONa	> 99.0 %	Alfa Aesar, Ward Hill, MA, USA
Sodium hydroxide	NaOH	98 %	Alfa Aesar, Ward Hill, MA, USA
Sodium sulfate anhydrous	Na_2SO_4	99.7 %	Acros Organics, Fair Lawn, NJ, USA
Tetrabuthylammonium (TBA) tetrafluoroborate	$(C_4H_9)_4N\,BF_4$	99 %	Sigma Aldrich, St. Louis, MO, USA
Tetramethylammonium (TMA) hydroxide in methanol	$(CH_3)_4N\,OH$	25 %	Sigma Aldrich, St. Louis, MO, USA
Tetramethylammonium	$(CH_3)_3N\,BF_4$	97 %	Sigma Aldrich, St.

(TMA) tetrafluoroborate			Louis, MO, USA
Tetramethylammonium (TMA) chloride	$(CH_3)_4N$ Cl	97 %	Sigma Aldrich, St. Louis, MO, USA
Zinc sulfate heptahydrate	$ZnSO_4$	≥ 99.0 %	Sigma Aldrich, St. Louis, MO, USA

To intercalate $Ti_3C_2T_x$ with the compounds listed in Table 4, 0.15 g of the powder was immersed in 5 ml of 30 wt.% aqueous solutions of potassium hydroxide, potassium acetate, lithium acetate, sodium acetate, sodium formate, sodium citrate, and zinc sulfate; 25, 20 and 10 wt.% aqueous solution of magnesium sulfate, sodium sulfate and potassium sulfate, respectively; 30 % aqueous solutions of acetic acid, sulfuric acid, and ammonium hydroxide. Then, the mixtures were stirred for 24 h using a magnetic stirrer at RT. The resulting colloidal solutions were then filtered through a polyester membrane (25 mm diameter, 3.0 μm pore size, Osmonics Inc., Minnetonka, MN, USA) and dried in a desiccator under vacuum (< 10 Torr) at RT.

3.2.2. Delamination

3.2.2.1. Dimethyl Sulfoxide Technique

Dimethyl sulfoxide (DMSO) was principle compound used to delaminate $Ti_3C_2T_x$. To obtain a solution of delaminated $Ti_3C_2T_x$ sheets, multilayered $Ti_3C_2T_x$ was stirred with DMSO for 18 h at RT, and then the colloidal solution was centrifuged at 3500 rpm to separate the intercalated powder from the liquid DMSO. After decantation of the supernatant, deionized water was added to the residue in a weight ratio of MXene to water of 1:500. Then the suspension was sonicated under Ar for 4 h, and centrifuged for 1

h at 3500 rpm. At last, the supernatant, containing the delaminated $Ti_3C_2T_x$ sheets, was decanted and stored in bottles sealed under Ar for further experiments.

3.2.2.1. Isopropyl Amine Technique

Isopropyl Amine (i-PrA) method was the primarily compound used to delaminate Nb_2CT_x. To obtain a solution of delaminated Nb_2CT_x sheets, multilayered Nb_2CT_x was stirred with i-PrA in water in a 1:5 ratio for 18 h at RT, and then the colloidal solution was centrifuged to separate the intercalated powder from the liquid i-PrA. After decanting of the supernatant, deionized water was added to the residue in a weight ratio of MXene to water of 1:250. Then the suspension was sonicated under Ar for 1 h, and centrifuged at 1 h with 1250 rpm. Finally, the supernatant containing the delaminated Nb_2CT_x sheets was decanted and stored in bottles sealed under Ar for further experiments.

3.3. Characterization

Variety techniques (Table 5) were used to characterize MXene structure, morphology, chemistry, and properties.

Table 5. *A list of analytic techniques used for material characterization.*

Characterization	Method used
Crystal structure	• X-ray diffraction • Neutron diffraction • Raman spectroscopy • Selective area electron diffraction
Material morphology	• Transmission electron microscopy • Scanning electron microscopy
Elemental chemical composition	• Energy-dispersive X-ray spectroscopy • X-ray photoelectron spectroscopy • Inelastic neutron scattering analysis
Conductivity measurements	• 4-point probe
Other studies	• Thermogravimetric analysis • UV-Vis spectrophotometry

3.3.1. X-Ray Diffraction

X-ray diffraction (XRD) patterns were obtained with a powder diffractometer (Rigaku, SmartLab, Tokyo, Japan) using Cu K_α radiation (λ = 1.54 Å), an acceleration voltage of 40 kV and an anode current of 30 mA, and a step scan of 0.02° and 1 s per step (Figure 7A).

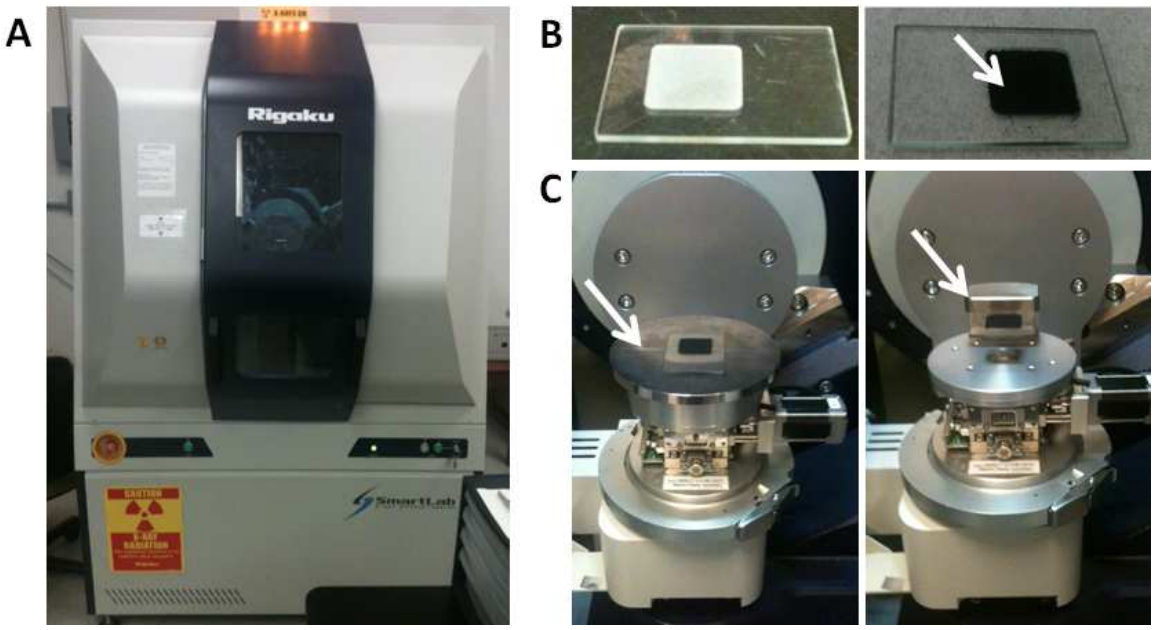

Figure 7. *(**A**) Rigaku X-ray powder diffractometer. (**B**) Glass sample holder: empty (to the left) and filled with finger-pressed powder (to the right). (**C**) Types of stage: flat stage for pressed pellets and films (to the left) and a glass holder stage for powders.*

To record XRD diffractograms, different sample preparation techniques were used. Due to the flakiness of the exfoliated powders, they were prone to settling with their basal planes parallel to the surface when the XRD samples were prepared. In such a situation, it is difficult to reproduce, and thus quantify, results. It was found that pressing the exfoliated powders resulted in: i) a large increase in the (00l) peak heights, ii) greater signal to noise ratios and, iii) much more reproducibility from sample to sample. Consequently, powdered samples were either cold pressed at 1 GPa into thin 25 mm diameter discs that were ≈ 300 μm thick, or hand pressed into a special glass holder with 20 ×20 mm opening of 1 mm deep (Figure 7B and C, respectively). In case of the free standing paper of delaminated MXene, the sample was used as is, simply by placing the paper on the flat stage of the XRD machine.

The Jade 5.0 software was used to analyze the diffractograms, identify peaks, find crystalline structures, index the patterns, calculate lattice parameters, etc. Peak deconvolution, if needed, was performed using the software LabSpec v4.02.

3.3.2. Electron Microscopy

3.3.2.1. Scanning Electron Microscopy

A scanning electron microscope (SEM, Zeiss Supra 50VP, Germany) was used to obtain images of the MXenes (Figure 8A).

Depending on material morphology, different techniques of sample preparation were used. In case of multilayered MXene powders, the material was fixed on a small specimen stage using carbon tape (Figure 8B). In case of delaminated flakes, a drop of supernatant containing flakes containing supernatant was placed on an anodic aluminium oxide membrane (47mm diameter, 0.2 μm pore size, Whatman Anodisc, Maidstone, Kent, UK) which was attached to a specimen stage using carbon tape. In case of *d*-MXene papers, free-standing or on alumina membranes, those were attached to one of the flat side of the hexagonal stainless steel nut using carbon tape. When the nut was mounted on the SEM stage, the sample was vertical so that an image of its cross-section could be taken (Figure 8C).

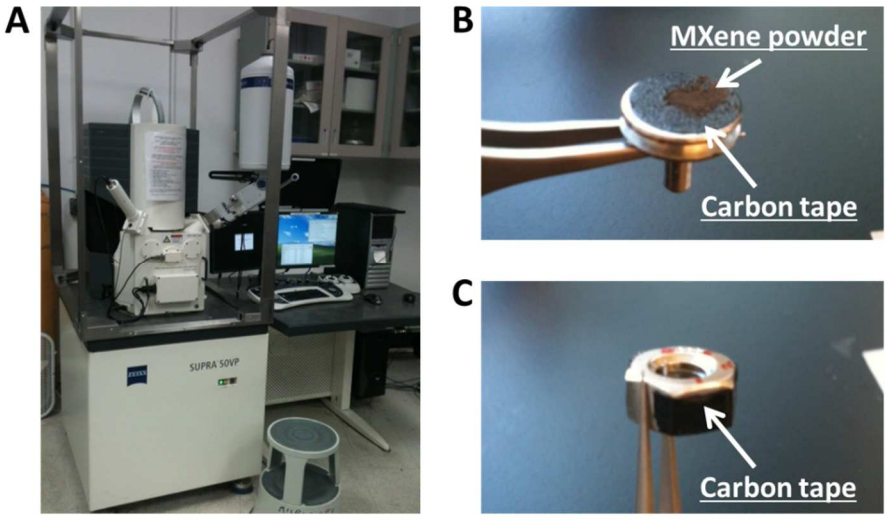

Figure 8. *(**A**) Zeiss Supra 50VP JEOL scanning electron microscope; (**B**) side view of a small specimen stage with MXene powder sample glued with carbon tape; (**C**) side view of a stainless steel nut with a carbon tape on the facets used to analyze the cross-section of MXene papers.*

3.3.2.2. Transmission Electron Microscopy

A transmission electron microscopy (TEM, JEOL JEM-2100, Japan) was used to analyze the structure and morphology of the MXene particles (Figure 9A). The TEM samples were prepared by suspending powders in isopropanol alcohol, sonicating for 10 min, and placing a drop of the mixture on a 200 mesh carbon-lacey-coated copper grid (Figure 9B and C). TEM images were taken using accelerating voltages of 120 or 200 kV depending on the sample sensitivity toward electron beam exposure.

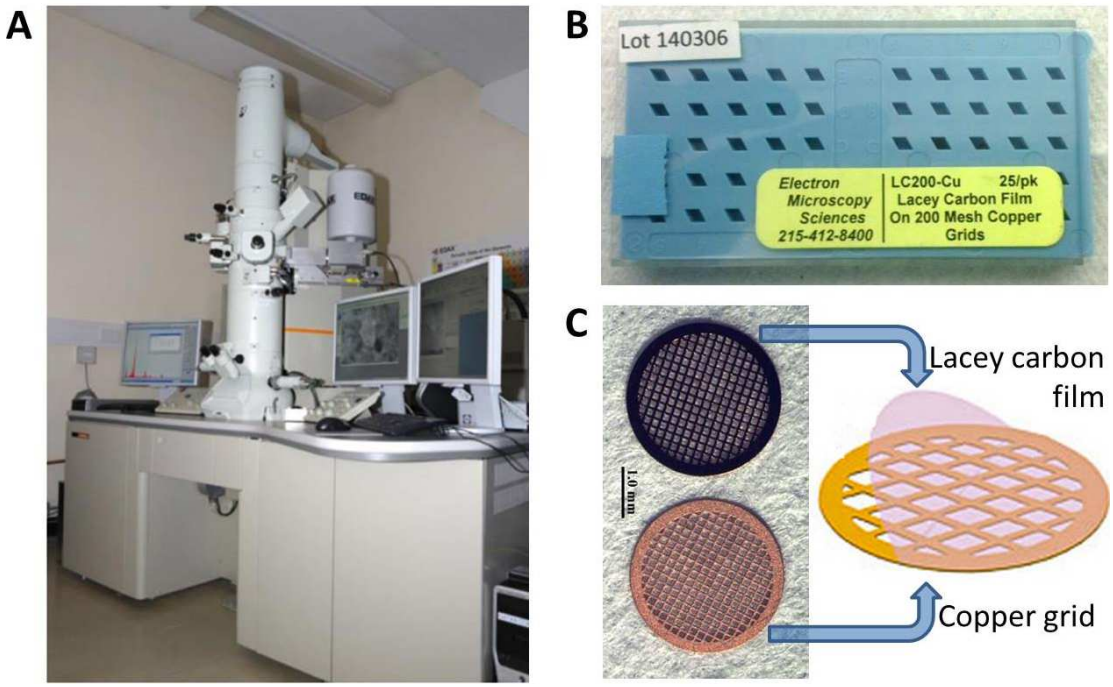

***Figure 9**. (**A**) JEOL JEM-2100 transmission electron microscope; (**B**) lacey- carbon-coated copper grids used for sample analysis in TEM; (**C**) top and bottom views of a lacey- carbon-coated copper grid and its representative schematics.*

3.3.3. Thermogravimetric Analysis

Thermogravimetric analysis (TGA) was performed using a thermogravimetric analyzer (TA Instruments TGA-Q50, USA) (Figure 10). The sample-containing chamber was first purged for 2 h with nitrogen, N_2, before heating to 500 °C in the same atmosphere at 5 °C/min heating rate. The N_2 flow rate was 60 ml /min.

Figure 10. *Q50 thermogravimetric analyzer*

3.3.4. X-Ray Photoelectron Spectroscopy

An X-ray photoelectron spectrometer, XPS, (VersaProbe 5000, Physical Electronics Inc., MN, USA) employing a 100 μm monochromatic Al K_α X-ray beam to irradiate the surface of the samples was used to obtain the XPS spectra (Figure 11A). Emitted photoelectrons were collected using a 180° hemispherical electron energy analyzer. Samples were analyzed at a 45° takeoff angle between the sample surface and the path to the analyzer. High-resolution spectra were taken at a pass energy of 23.50 eV and with a step size of 0.05 eV. The peak fitting was carried out using CasaXPS Version 2.3.16 RP 1.6. Adventitious C1s, C-C peak at 284.8eV, or Fermi energy were used as a charge reference for XPS spectra.

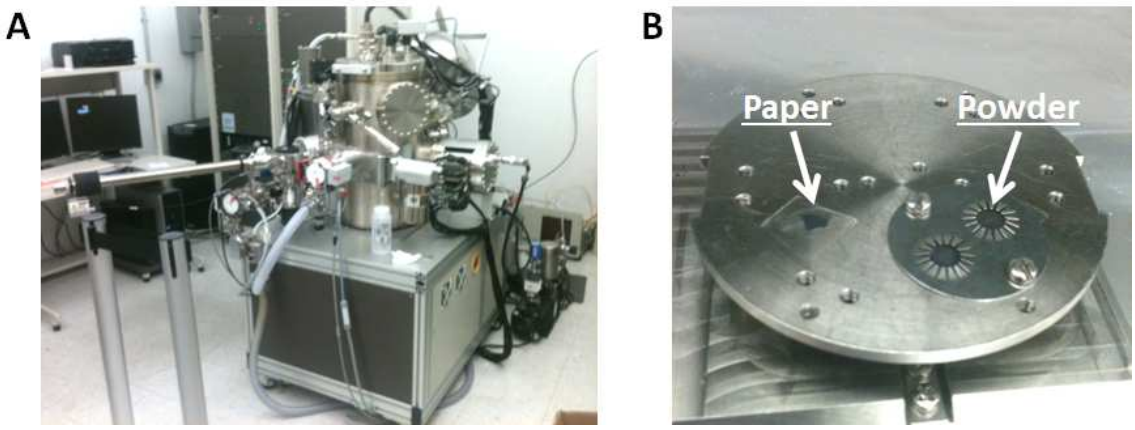

***Figure 11**. (**A**) VersaProbe 5000 X-ray photoelectron spectrometer. (**B**) Mounting of two different types of MXene sample, paper and powder, on XPS stage.*

No special preparation of samples by themselves was required. MXene samples could be mounted on the XPS stage in two different ways, as shown in Figure 11B. A mask with openings was used to mount the powders. The latter were gently pressed into the openings and purged with Ar to remove loose particles. If a film needed to be analyzed, it was fixed on the stage used sticky tape or a special metal holder attached to the stage by a screw (not shown).

3.3.5. UV-Vis Spectroscopy

The solution dye concentration in the adsorption and photodegradation tests was monitored at 664 nm wavelength using a UV-Vis spectrophotometer (Evolution 300, Thermo Fisher Scientific Inc., MA, USA) and PS disposable cuvettes with a 10 mm optical pathway (Brand Tech Scientific, Essex, CT, USA) (Figure 12A and B). A baseline was recorded using DI water and subtracted from all measured spectra.

Figure 12. *Photographs of (**A**) Thermo Scientific Evolution 300 UV-Vis spectrophotometer and (**B**) diposable BrandTech polystyrene cuvettes used for experimental work.*

3.3.6. Raman Spectroscopy

Raman spectra were recorded using a 514.5 nm Ar ion laser as the excitation source (Renishaw RM1000 Raman spectrometer, Renishaw plc, Gloucestershire, U.K.) focused to a spot size of ≈ 2 μm with a power of less than 1 mW (Figure 13).

Figure 13. *Renishaw RM1000 Raman spectrometer.*

3.3.7. Gas Sorption Analysis

Gas sorption analysis was carried out using a Quantachrome Autosorb-1 with nitrogen (N_2), carbon dioxide (CO_2), and Ar gases as adsorbates. Prior to the analysis, the samples were outgassed under vacuum at 200 ºC for 48 h. The specific surface area (SSA) was calculated from the volume absorbed at 77 K using the Brunauer-Emmet-Teller equation. The gas sorption measurements for the multilayered and delaminated $Ti_3C_2T_x$ were carried out on the MXene powder and paper that was synthesized by filtering the delaminated MXene suspension as described above, respectively.

3.3.8. Electrical Resistivity Measurements

The electrical resistances of some of the treated powders were measured by a four-point probe technique using: i) Cascade Probe Station CPS-1303-24 with a 4-point probe head Alessi C4S-57 (Cascade Microtech, Inc., Beaverton, OR, USA), or ii) Jandel MultiHeight Probe with a 4-point probe head of serial number LB33795 with a spacing of $s \approx 1$ mm (Jandel Engineering Limited, Linslade, UK) (Figure 14). The measurements were made on cold-pressed (1 GPa) discs 25 mm in diameter and ≈ 300 μm thick, or delaminated MXene paper ≈ 10 μm thick.

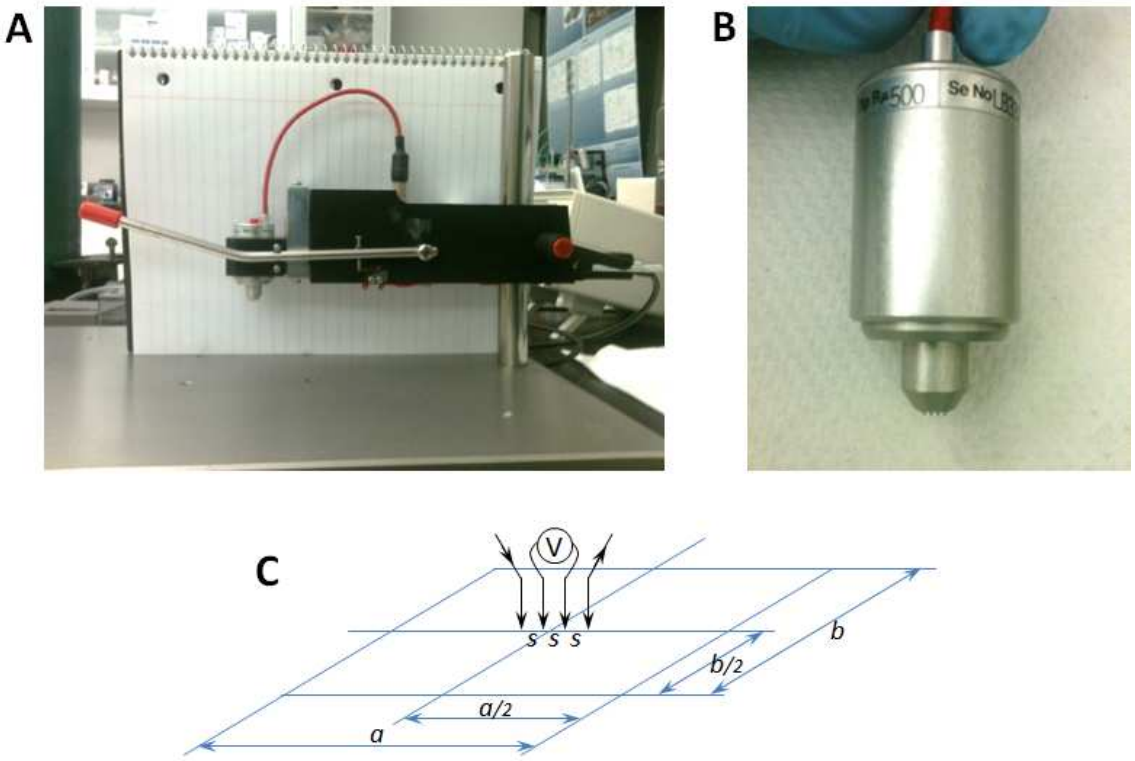

Figure 14. *Jandel MultiHeight Probe (**A**) with a 4-point probe head of serial number LB33795 (**B**). (**C**) Schematic of 4-point probe configuration.*

To measure sheet resistance R_s and bulk resistivity, ρ, of discs and films (those are considered to be "semi-infinite sheets"), the following formulae (7) and (8) were used, respectively:

$$R_S = \frac{\pi}{ln2} \cdot C_1 \cdot C_2 \cdot \frac{V}{I}\,, \tag{7}$$

$$\rho = R_S \cdot t = \frac{\pi}{ln2} \cdot C_1 \cdot C_2 \cdot \frac{V}{I} \cdot t\,, \tag{8}$$

where $\frac{\pi}{ln2} \cdot C_1 \cdot C_2 \cdot t = 4.5324 \cdot C_1 \cdot C_2 \cdot t$ is the geometric factor for a semi-infinite sheet of thickness t and correction factors C_1 and C_2 (see Table 6); V is the measured voltage, and I was the test current.

Table 6. *Correction factors for resistivity measurements.*

Correction factor for sample thickness *t*		**Correction factor for sample diameter *d***	
t/s	***C_1(t/s)***	***d/s***	***C_2(d/s)***
0.3	1.0000	10	0.9204
0.4	0.9995	20	0.9789
0.5	0.9974	30	0.9906
0.6	0.9919	40	0.9942
0.7	0.9816	50	0.9966
0.8	0.9662	60	0.9977
0.9	0.9459	70	0.9983
1.0	0.9215	80	0.9987
1.2	0.8643	90	0.9990
1.4	0.8026	100	0.9992
1.6	0.7419	200	0.9999
1.8	0.6852	∞	1.0000
2.0	0.6337		

3.3.9. Dynamic Light Scattering Analysis

Dynamic light scattering measurements were performed according the following procedure: A ~1.5 mL of delaminated *d*-$Ti_3C_2T_x$, dispersed in water, was transferred in a clear disposable particle size measurement cell (DTS0012, Malvern Instruments, Ltd. Malvern, Worcestershire, UK) (Figure 15B and C), equilibrated at 25 °C for 60 s, and then measured with a particle size analyzer (Zetasizer Nano ZS, Malvern Instruments, Ltd.) (Figure 15A) equipped with a 50 mW, 633 nm laser with scattered light detected at 173° to the direction of the incident light (173° Backscatter NIBS default), which is an optimal geometry for detecting small particles. Each sample was measured three times.

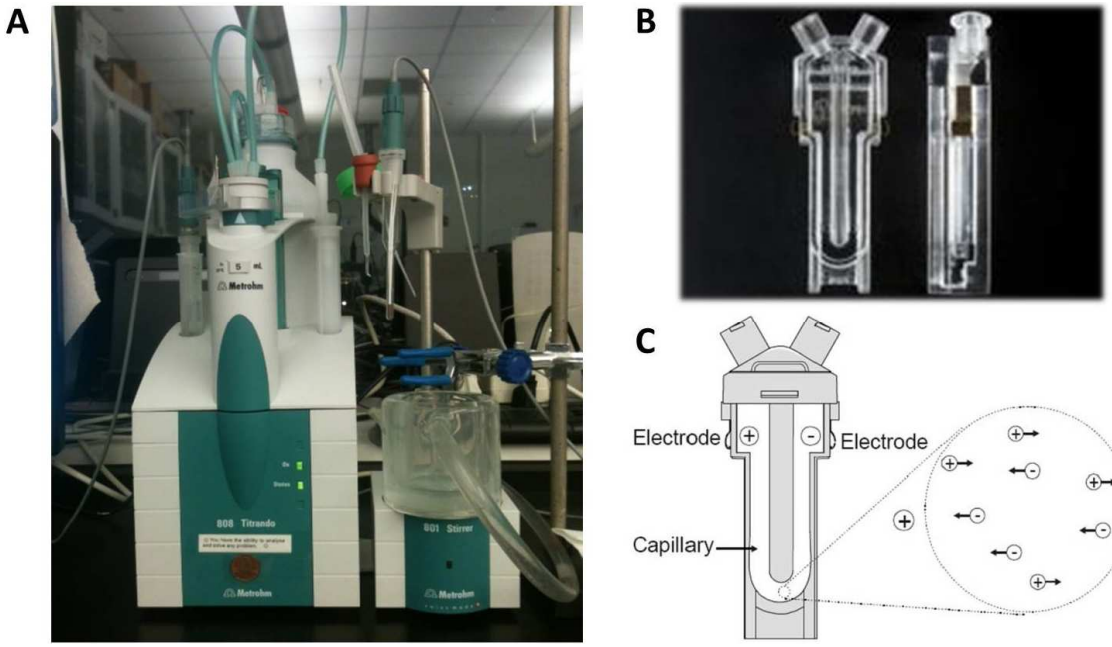

***Figure 15**. (**A**) Zetasizer Nano ZS instrument. (**B**) An image and (**C**) schematic of a folded capillary cell for zeta potential measurements.*

In its original form, used here, DLS approximates particles of any shape by equivalent spheres; therefore it is most suited for particles of nearly spherical shape. For *d*-$Ti_3C_2T_x$ flakes the approximation by spheres is quite strained and the "diameter" deduced from these measurements is an average of their lateral dimensions and thickness.

3.3.10. Small-Angle Neutron Scattering Diffraction

Small-angle neutron scattering (SANS) was used to investigate the effect of intercalation of several molecules into the $Ti_3C_2T_x$ interlayers on the resulting effect on the material's interlayer spacing, sheet thickness, domain size, and macroparticle surface roughness. The experiments were performed using EQ-SANS Diffractometer at the Spallation Neutron Source (SNS) at Oak Ridge National Laboratory (ORNL). The

research powders were loaded into the 50×50×1 mm cells under vacuum and sent to ORNL for analysis.

3.3.11. Inelastic Neutron Scattering Analysis

Inelastic neutron scattering (INS) experiments were performed using the fine resolution Fermi chopper spectrometer SEQUOIA at the SNS at ORNL [69]. INS measurements were made at T = 7 K, with four incident neutron energies: E_i = 50, 160, 250 and 600 meV, to provide high energy resolution (about 1-3% of E_i) in a wide range of energy transfer 2 meV < E < 550 meV. The collected neutron scattering data were transformed from time-of-flight and instrument coordinates to the dynamical structure factor $S(Q,E)$ using the mantidplot software package [70]. A generalized vibrational density of states $G(E)$ was then calculated. The INS spectra from the empty container were also measured under the same conditions and subtracted from the sample data.

3.3.12. High Energy Total X-Ray Scattering Analysis

Synchrotron X-ray total scattering experiments were conducted at beam line X17A at the National Synchrotron Light Source at Brookhaven National Laboratory. The samples were packed into Kapton® capillary tubes and measured at 100 K using a flowing nitrogen cryo-cooler.

3.3.12. Temperature-Programmed Desorption Mass Spectroscopy

Temperature-programmed desorption mass spectroscopy (TPD-MS) was performed under an inert atmosphere (He). The sample (10-20 mg) was placed in a thermo-balance

(STA 449C, Netzsch, Germany) and kept at RT for 1 h under a He flow of 150 mL min^{-1}. Then, the temperature was increased to 1200 °C at a rate of 10 °C min^{-1}. The decomposition products (gas evolution) were monitored by on-line mass spectrometry (QMS 403C, Netzsch, Germany). Mass-to-charge ratio (*M*/*z*) was screened between 2 and 300 a.m.u while heating the sample under a He flow.

3.4. Experimental Procedures

3.4.1. Preparation of Cold-Pressed Discs

As noted above, the non-intercalated and intercalated MXene powders were cold pressed under a load corresponding to a stress of 1 GPa using a manual hydraulic pellet press (Carver, Model 4350.L, Carver, Inc., Wabash, WI, USA). The resulting discs were 12.5 mm in diameter and 250-400 μm thick (Figure 16).

Figure 16*. Cold-pressed disc of $Ti_3C_2T_x$ powder.*

3.4.2. Adsorption Measurements

Adsorption and photodegradation experiments were performed using methylene blue, MB (0.1 w/v %, Ricca Chemical, Arlington, TX, USA), and acid blue, AB80 (40 wt.%, Sigma Aldrich, St. Louis, MO, USA), aqueous solutions. To eliminate dye

adsorption on the container walls, only polypropylene or polystyrene vials were used throughout the work.[71] For comparison of the photocatalytic activity, commercial titanium dioxide, TiO_2, P25 (ca. 25% rutile and 75% anatase; Evonik Degussa GmbH, Germany), was used.

To study the kinetics of dye adsorption, 100 mg of $Ti_3C_2T_x$ powders were suspended in 100 mL of the 0.05 mg/mL MB solution or the 0.06 mg/mL AB80 solution. After the addition of $Ti_3C_2T_x$, the solutions were kept in the dark while being continuously shaken. Aliquots of liquids were taken at certain intervals during the adsorption process in order to monitor the dye concentration *vs*. time. To build an adsorption isotherm for the MB–$Ti_3C_2T_x$ system, a series of solutions were prepared in which the amount of $Ti_3C_2T_x$ was kept constant (20 mg per 10 mL), while the MB concentration, C_0, was varied. These solutions of different concentrations were left shaking for 20 h in the dark to allow them to reach equilibrium, and then the MB equilibrium concentrations C_{Eq} in the solutions were measured.

3.4.3. Photodegradation

For the MB photodegradation tests, the same amount of each catalyst (10 mg) and volume of dye solutions (40 mL) were used for all experiments. Because of a large difference in adsorption properties of $Ti_3C_2T_x$ and TiO_2, different initial MB concentrations were used: 0.012 mg/mL in case of $Ti_3C_2T_x$ and 0.006 mg/mL in case of TiO_2. Experiments were carried out either in ambient or under Ar atmospheres.

For the AB80 photodegradation tests, 0.025 g of either $Ti_3C_2T_x$ or TiO_2, was added to 40 mL of the 0.06 mg/mL AB80 aqueous solution. The mixtures were held in

the dark for 2 h, while under continuous magnetic stirring, then illuminated using a UV-C lamp (254 nm, G16T5, China) with an irradiance of 52 μW/cm^2. Aliquots of 1.5 mL were then taken for analysis to monitor the changes in dye concentration. In all experiments described above, the aliquots were centrifuged at 3500 rpm in polypropylene Eppendorf tubes for 15 min to remove the $Ti_3C_2T_x$ particles before recording the UV-Vis spectra of the liquid phase. When necessary, MB solutions were diluted with DI water prior to recording their spectra to ensure that the maximum measured absorbance was always below 0.6. This was done in order to suppress the dimerization of MB in water that occurs at concentrations > $7 \cdot 10^{-6}$ mole/L [71]. The dye concentration was calculated using a calibration plot (see Figure 17). The experimental adsorption data were fit to the Freundlich and Langmuir isotherms using a nonlinear least-squares fit procedure.

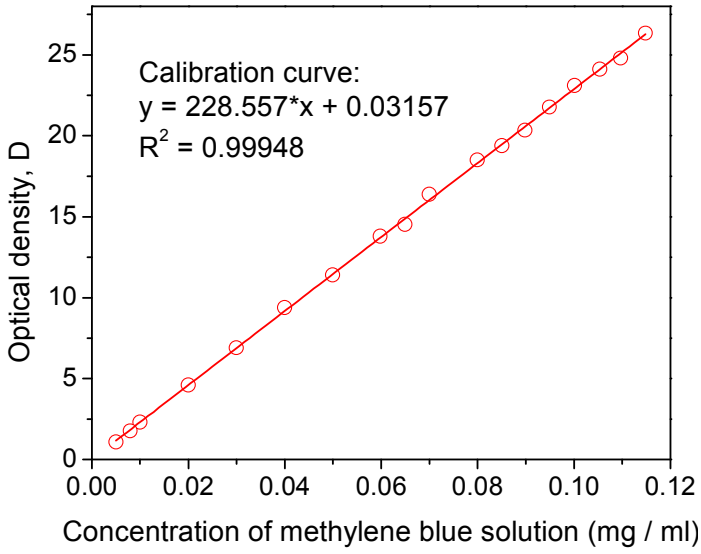

Figure 17*. Calibration curve for aqueous solutions of MB. All values of optical density were taken at the adsorption peak at 664 nm. Note: The molar extinction coefficient for MB recalculated from the calibration curve was 73,200 dm^3/(mole·cm) which was in excellent agreement with coefficients described in a first non-patent document by S. Prahl [72].*

3.4.4. Annealing in NH_3 atmosphere

$Ti_3C_2T_x$ powder was placed in a horizontal quartz tube furnace (Carbolite MTF 12/38/400), purged in an Ar flow (20 cm^3/min) for 1 h, and treated in the range from RT up to 450 ˚C under flowing NH_3 (10 – 15 cm^3/min) for 3 h (see schematic in Figure 18).

Figure 18. *Schematic of the tube furnace set up used for NH_3 annealing of $Ti_3C_2T_x$.*

3.5. Thermodynamic Calculations

Thermodynamic calculations were performed using FactSage6.2 software. To generate Eh *vs*. pH (Pourbaix) diagrams for the oxidation of $Ti_3C_2T_x$, the "EpH" module was used. All calculations were carried out for the 5-element system Ti-C-F-O-H at a pressure of 1 atm, temperature 298.15 K, and fluorine molality m[F^-] of 0.1.

3.6. Molecular Dynamics Simulations

Molecular dynamics (MD) simulations were performed using the Forcite module in Materials Studio suite (Accelrys, San Diego, CA, USA). Due to the unusual composition of the system, including C, Ti, O, N, and H, the Universal Force Field (UFF) [73] was used to calculate the system's energy (see Appendix A for details). Before simulations, 4x2x1 (*a* x *b* x *c*) OH-terminated Ti_3C_2 periodic supercells with different numbers of N_2H_4 molecules were constructed using the unit cell structure of $Ti_3C_2(OH)_2$ from previous density functional theory (DFT) simulations [23]. The supercells,

subjected to an isostatic external pressure of 0.1 MPa (1 atm), were first relaxed by geometry optimization (Convergence tolerance: Energy = 0.02 cal/mol, Force = 1 cal/mol/Å, stress = 1 MPa, displacement = 0.00001Å) with no constraints allowing for all atom positions in the cell, as well as the cell parameters, to be optimized. Charge distribution was calculated using the charge equilibration method (Initial charge = 0, Maximum iterations = 100, Convergence limit = 0.0005 $\bar{e}$, Parameter set = QEq_charged1.1) [73].

Once optimized, the supercells were used as initial structures in the MD runs. Isobaric-isothermal ensemble MD was performed at 298 K (Nosé thermostat with Q ratio = 1.0) with random initial velocities and 0.1 MPa external isostatic pressure (Berendsen barostat with decay constant = 0.1 ps) for 300 ps in 1 fs steps (300000 steps in total). Snapshots of the system were saved every 3000 MD steps (100 snapshots in total) of which only the last 50 snapshots were used for analysis. This procedure allowed for >100 ps in the beginning of each run for thermal equilibration of the system with the analysis being performed on the part of the trajectory corresponding to a system in an equilibrium state (Figure 19B and C), where all energy terms and the density of the system remained nearly constant. No constrains on atom positions or cell parameters were applied during the MD run. During both the geometry optimization step and the MD run, the electrostatic interactions were summed using an Ewald scheme and the van der Waals interactions were summed using the atom based scheme.

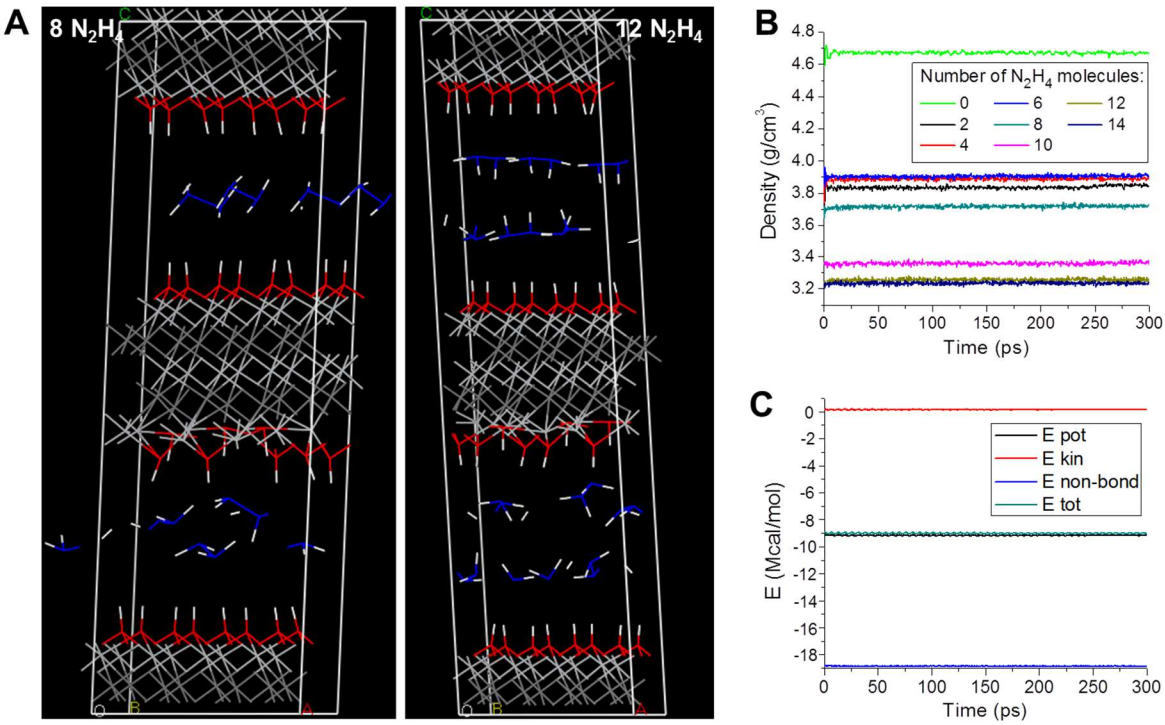

Figure 19. *Molecular dynamics simulations. (**A**) Representative molecular dynamics (MD) snapshots of 4x2x1 $Ti_3C_2(OH)_2$ MXene supercells with 8 and 12 molecules of N_2H_4. Carbon is shown in dark grey, titanium in light grey, oxygen in red, nitrogen in blue, hydrogen in white. Analysis of MD trajectories revealed that the steps were due to the onset, formation, and completion of N_2H_4 monolayers. The transition from monolayer to bilayer of intercalate was observed in the structure with 8 N_2H_4 molecules while the supercell with 12 N_2H_4 in the interlayer space of MXene showed distinct bilayers of the intercalate molecules. (**B**) Density evolution of 4x2x1 MXene supercell intercalated with different numbers of N_2H_4 molecules. (**C**) Energy evolution of 4x2x1 MXene supercell with 6 molecules of N_2H_4 showing that the energy is conserved during the MD run.*

CHAPTER 4: RESULTS AND DISCUSSION

4.1. Kinetics of $Ti_3C_2T_x$ Exfoliation

The diffractograms of the treated powders (Figure 20A and B) showed that the degree of Al etching depended on reaction temperature and time. This was best seen by focusing on the most intense peak at $2\theta \approx 39°$ – that corresponded to the (104) peak of Ti_3AlC_2. This peak diminished with increasing temperature and time, disappearing altogether above 50 °C and after 15 h, respectively, indicating the etching of the Al from the structure [74]. Concomitantly, the intensity of the (002) diffraction peak at $2\theta \approx 9^{\circ}$ which corresponded to the basal planes of the 2D $Ti_3C_2T_x$-based layers, most likely terminated with OH groups – increased. The fact that this peak shifted to lower angles, compared to the (002) peak of non-exfoliated Ti_3AlC_2 was evidence for the expansion along (00l), as the Al was replaced by OH or F [74]. Because of the relatively wide particle size distribution range (from hundreds of nano- up to tens of micrometers with a ~75 wt.% fraction for particles within the 1-20 μm size range) and diffusion-limited etching, the expansion was not uniform. Consequently, the position of the (002) MXene peaks varied slightly from sample to sample resulting in different values of *c*-lattice parameters, *c*-LPs (Table 7).

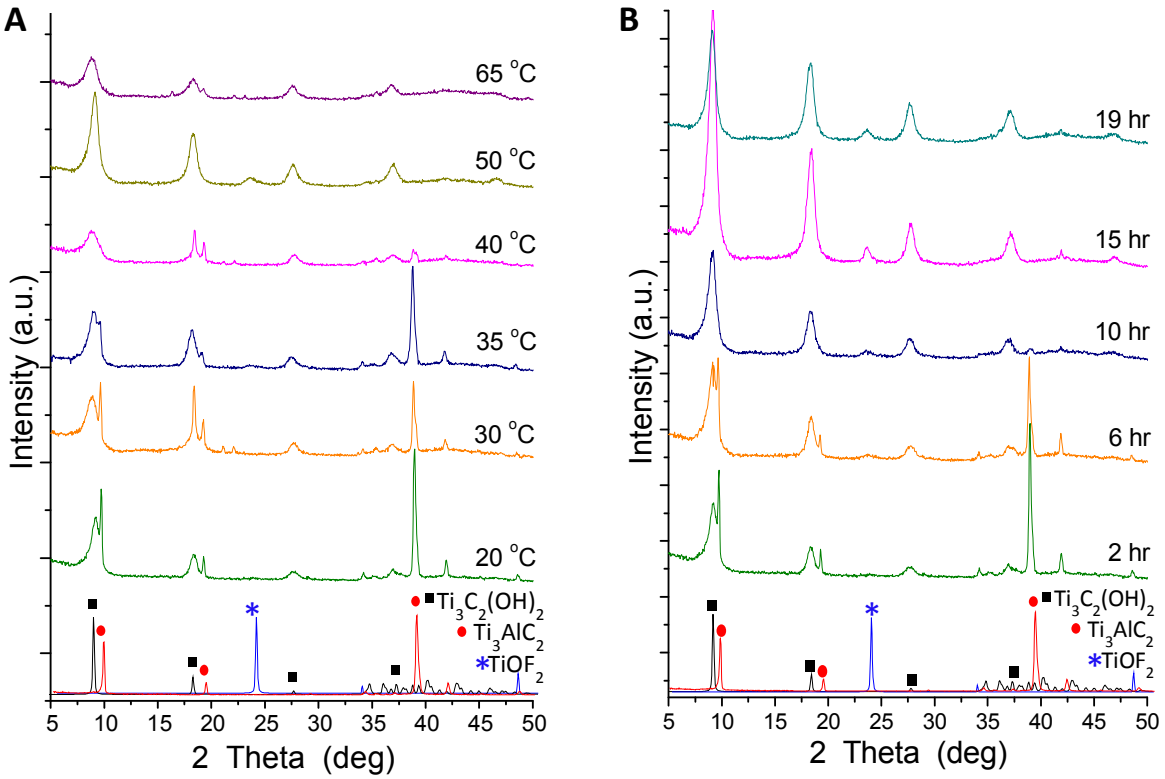

Figure 20. *Diffractograms obtained after etching Ti_3AlC_2 powders a 50 wt.% HF solution as a function of (**A**) temperature after 2 h of etching and, (**B**) time at room temperature. The diffractograms at the bottom of each panel show the XRD patterns of $Ti_3C_2(OH)_2$ (black lines) and Ti_3AlC_2 (red lines) previously predicted by DFT-based geometry optimizations [74]; XRD pattern of $TiOF_2$ was taken from MDI Jade 5.0 database.[75]*

A calibration curve (Figure 21B) was plotted from the XRD results (Figure 21A) of samples with known ratios of fully reacted to unreacted Ti_3AlC_2. Polynomial fitting of the calibration curve (shown as a solid line in Figure 21B) yielded:

$$y = 1 - 0.2\,x + 0.013\,x^2,$$

where y was the weight fraction of $Ti_3C_2T_x$ and x the intensity ratio of the Ti_3AlC_2 (104) peak to the $Ti_3C_2T_x$ (002) peak. Using this calibration curve, y was determined for each run shown in Figure 21 and plotted it as functions of temperature and time in Figure 22.

Here again, clearly, the degree of exfoliation increased with increasing time and temperature. At temperatures above 50 ºC, complete exfoliation of Ti_3AlC_2 with HF occured after 2 h. At RT, the process could take as long as 15 h.

Table 7. *List of HF treatment runs carried out. In all cases the etching solution was a 50 wt.% HF. The last column lists the c-lattice parameters of the resulting cold-pressed powders as measured from XRD diffractograms.*

Run number	**Time (h)**	**Temperature (°C)**	**Particle size (µm)**	***c*-lattice parameter, Å**
1.1	2	Room temperature (RT)	non-sieved	19.30
1.2	6	RT	non-sieved	19.38
1.3	10	RT	non-sieved	19.46
1.4	15	RT	non-sieved	19.39
1.5	19	RT	non-sieved	19.49
2.1	2	30	non-sieved	19.84
2.2	2	35	non-sieved	19.61
2.3	2	40	non-sieved	19.89
2.4	2	50	non-sieved	19.44
2.5	2	65	non-sieved	19.92
3.1	2	RT	< 38	19.55
3.2	2	RT	38 – 53	19.64

Note: To separate the contributions from two superimposed MXene and MAX phase peaks around $2\theta \approx 9°$ and calculate *c*-LP value, the crystal lattice parameters and intensity ratios were estimated using a summed Gaussian/Lorentzian peak-fitting after baseline correction. *(See Appendix B for more details)*

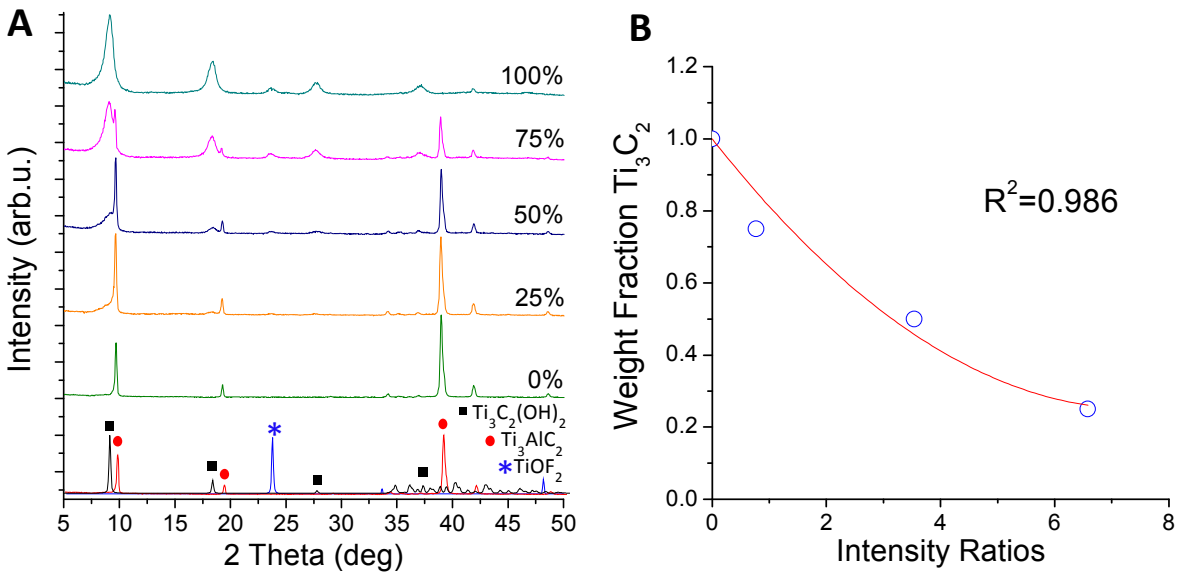

***Figure 21**. (**A**) Diffractograms taken from cold pressed mixtures of $Ti_3AlC_2/Ti_3C_2T_x$ of known ratios used to generate the calibration curve shown in (B). Percentage values indicated weight fraction of $Ti_3C_2T_x$ in the powder mixture; (**B**) $Ti_3C_2T_x$ weight fraction vs. the (104) peak for Ti_3AlC_2 /(002) peak of $Ti_3C_2T_x$, intensity ratio. These results were used to generate the results shown in Figure 22. [75]*

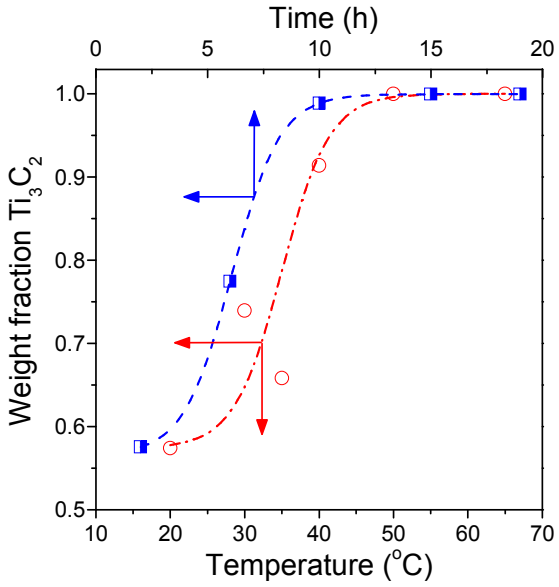

***Figure 22**. Effect of temperature (red, bottom x-axis) and time (blue, top x-axis) on exfoliation kinetics. In all cases the powders were immersed in a 50 wt.% HF solution. The temperature dependence was obtained after 2 h treatment in the acid. The time dependence was obtained at room temperature. [75]*

The powders with particle sizes within 38-53 μm range were completely exfoliated by stirring in a 50 wt.% aqueous HF at RT for 2 h. However, these conditions were insufficient to exfoliate particles larger than 53 μm. Assuming the reaction is diffusion controlled, this implied a diffusion coefficient of ≈ 10^{-13} m^2/s.

4.2. Morphology and Structure of $Ti_3C_2T_x$

4.2.1. Macro- and Microstructure

Figure 23A shows a typical SEM image of an as-received Ti_3AlC_2 particle. After HF treatment, the resulting particles were clearly exfoliated (Figure 23B). At this stage, the $Ti_3C_2T_x$ layers were presumably joined together by weak van der Waals or hydrogen forces. This was indirectly confirmed by recent Li intercalation studies [76]. Further (see Section 4.4.2), it was found that $Ti_3C_2T_x$ layers held some charge on the surface suggesting that electrostatic forces might also contribute to interactions between the layers.

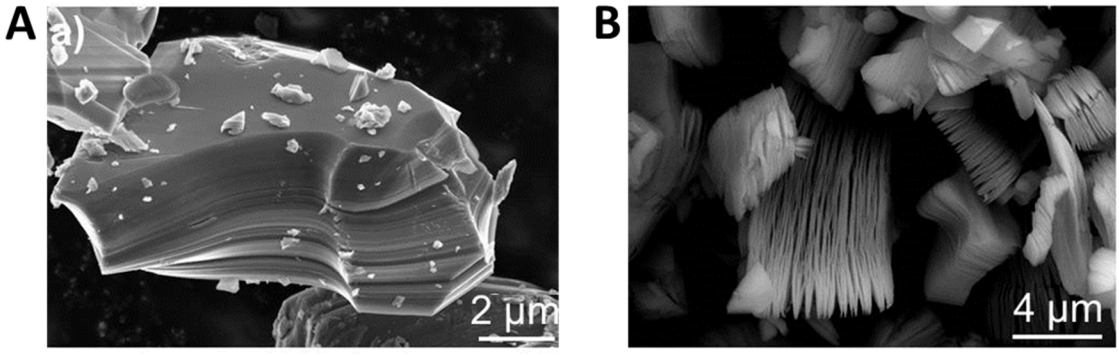

Figure 23. *Typical SEM images of Ti_3AlC_2 particles, (**A**) before and, (**B**) after HF treatment at 65 °C for 2 h, where exfoliation was evident.[75]*

As confirmed by TEM micrographs, the $Ti_3C_2T_x$ stacks were formed of electronically transparent single layers (Figure 24A), which could be further separated into single flakes following the liquid approach delamination technique discussed in Section 4.5.3.

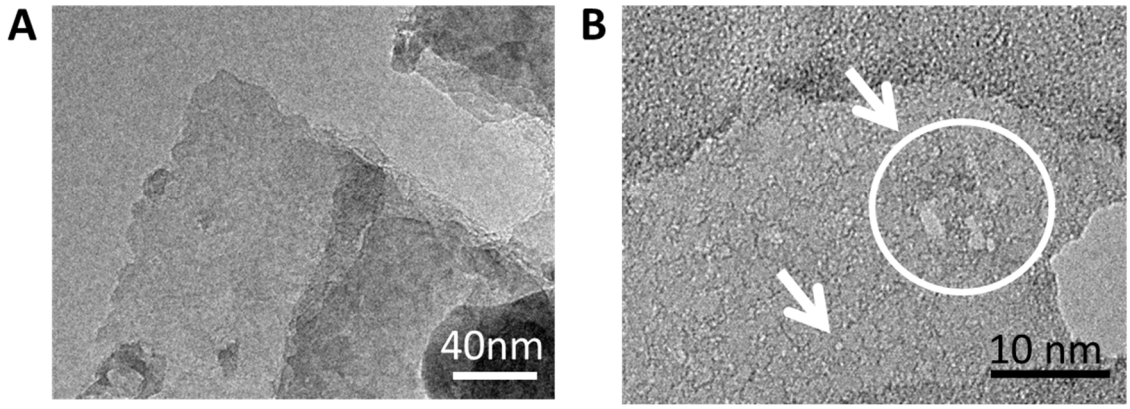

Figure 24. *TEM micrographs of $Ti_3C_2T_x$ etched at RT for (**A**) 20 h and, (**B**) over 22 h of etching at RT. Defect formation in the layers is marked with arrows in B.*

For some applications, it is important to produce high quality material with no surface defects. The formation of nanometer sized holes in $Ti_3C_2T_x$ MXene layers was observed when non-sieved Ti_3AlC_2 powder was etched with 50 wt.% HF for over 22 h (Figure 24B). Similar atomic defects were reported in functionalized graphene [77] and other MXenes [63]. The latter could act as nucleation sites for metal oxides which are useful in many applications [78, 79].

Interestingly, the TEM images also showed evidence for nano-arches at the edges of the exfoliated $Ti_3C_2T_x$ planes (Figure 25A and B). Similar folding of single graphitic layers which result in the formation of zipped edges – that were quite similar to those

shown here – has been reported previously [80, 81]. The mechanism of edge termination was explained by the van der Waals cohesion of the graphene sheets [82]. Figure 25A shows the formation of separated domains of $Ti_3C_2T_x$ sheets, presumably due to capillary and electrostatic forces arising after the removal of the Al layer and drying of the samples. A schematic for how this process could occur is shown in Figure 25C.

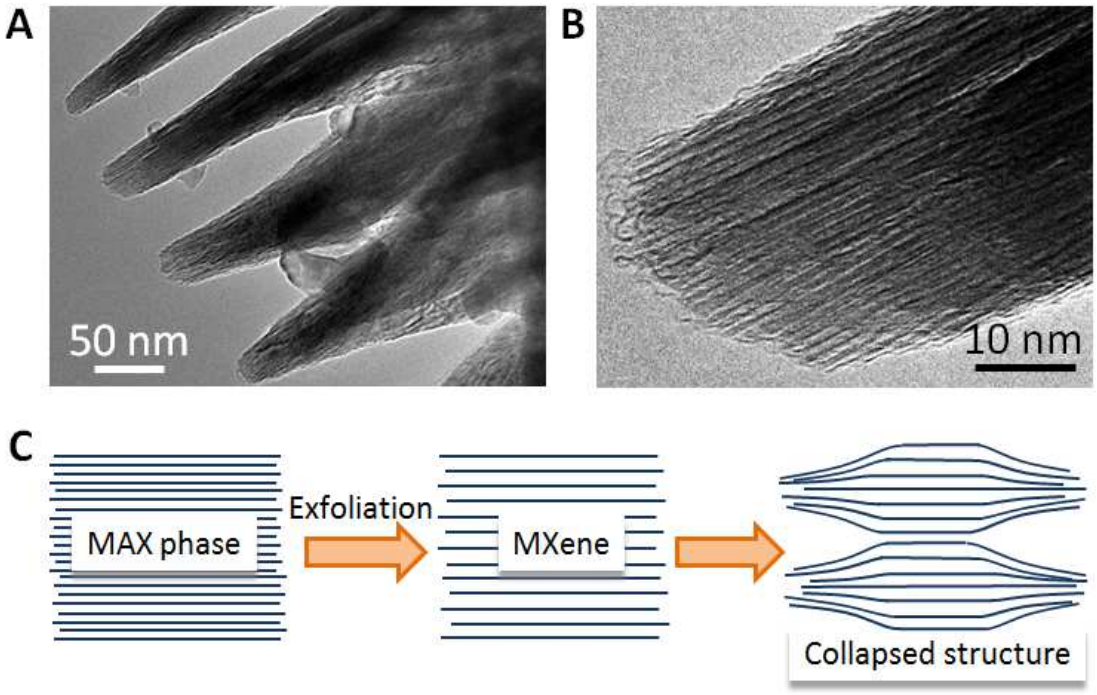

***Figure 25**. TEM micrographs of side view at the edges of the exfoliated $Ti_3C_2T_x$ planes, (**A**) general view and (**B**) zoom-in of (A); (**C**) schematic explaining how the sheet ends (seen in (A)) can stick together.[75]*

4.2.2. Crystallinity and Lattice Parameters

Side view TEM micrographs confirmed that $Ti_3C_2T_x$ maintained its layered structure after exfoliation showing interlayer separation of 9.8 Å (Figure 26A). Considering that a single unit cell of MXene consists of two interlayer distances, the

experimental *c*-LP calculated from TEM image is ≈ 19.6 Å. The latter was in very good agreement with the experimental *c*-LP value found from XRD patterns (see Run #3.2 in Table 7) and the theoretical value determined for simulated structure of hydroxylated $Ti_3C_2(OH)_2$ – 19.5 Å [74]. It was also in good agreement with the SANS results discussed in Section 4.2.2.

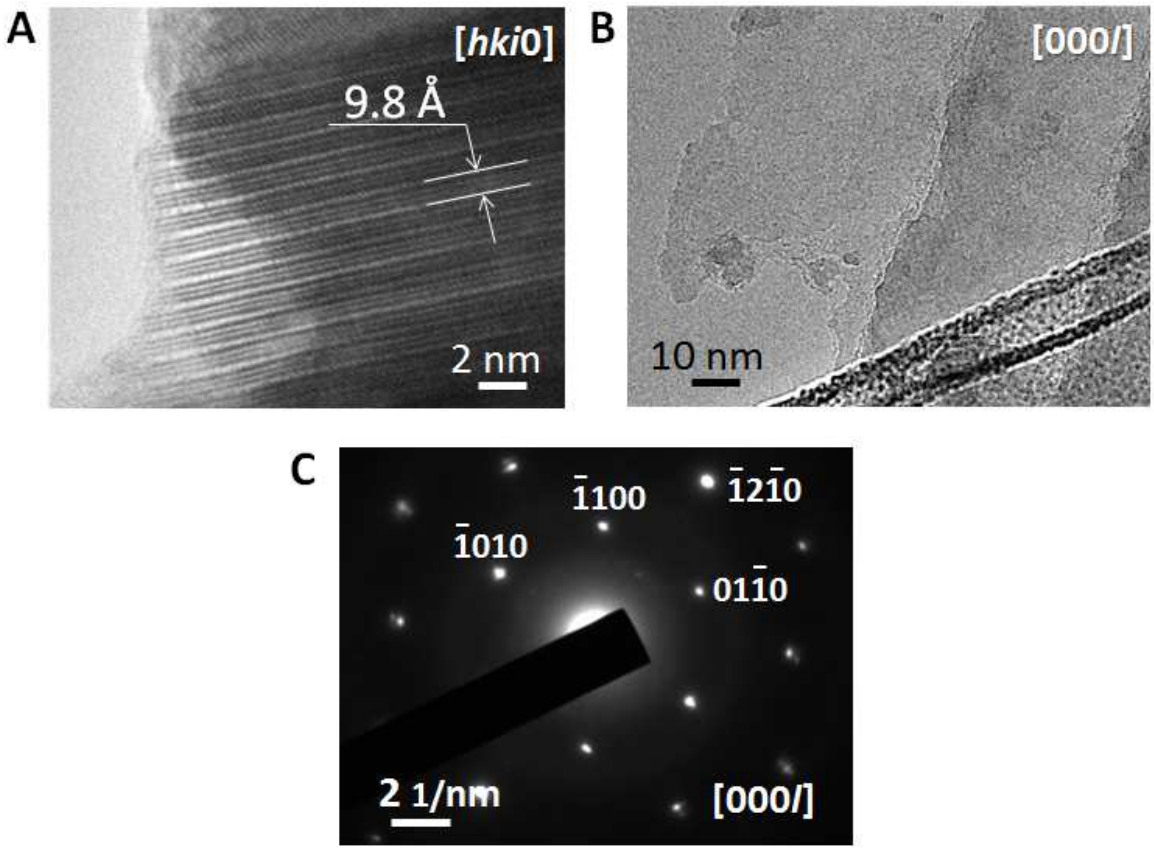

Figure 26. *Typical TEM micrographs for $Ti_3C_2T_x$ particles, (**A**) side view after HF treatment for 22 h at room temperature, (**B**) top view of exfoliated particles after 2-hour sonication, and, (**C**) a corresponding SAED pattern.*

The SAED pattern (Figure 26C) taken from the region shown in Figure 26B showed that the MXene layers maintained the hexagonal symmetry of the parent MAX phase. It implies that no degradation of the structure occurred upon etching.

An *a* lattice parameter (*a*-LP) was determine based on Bragg's Law [83] using the following equation (9) found for hexagonal structures:

$$\frac{1}{d_{hkl}^2} = \frac{4}{3}\left(\frac{h^2+hk+k^2}{a^2}\right) + \frac{l^2}{c^2} \quad (9)$$

where *h*, *k* and *l* are theMiller indices of various lattice planes, and d_{hkl} corresponds to the spacing distance between adjacent (*hkl*) lattice planes. Using SAED pattern (Figure 26C), the *d* spacing for $(\bar{1}100)$ lattice plane was found to be 2.634 Å. By substituting this value into Eq. (3), the resulting *a*-LP is equal 3.041 Å. Given that a typical error for SAED-based calculations is known to be within 5 % of the final value, the latter is in a good agreement with the *a*-LP found for DFT simulated structures of Ti_3AlC_2 and $Ti_3C_2T_x$, viz. 3.058 and 3.048, respectively [74]. It is thus reasonable to conclude that the MXene flakes maintain the crystallinity of the basal places of the parental MAX phase.

4.2.3. Lateral Morphology of Layers

Each $Ti_3C_2T_x$ particle can be considered as a complex structural unit with the hierarchy shown in Figure 27. Thus, a MXene particle (Figure 27-I) consisted of multiple stacks of exfoliated, or individual, $Ti_3C_2T_x$ flakes. A single stacking - marked as a blue line in Figure 27-II - consists of a number of $Ti_3C_2T_x$ layers of thickness *A*. The lateral morphology of the stack can be also represented by smaller microdomains of thickness *A* and surface *B*×*C* (marked in Figure 27-II and shown as a separate unit in Figure 27-III and IV).

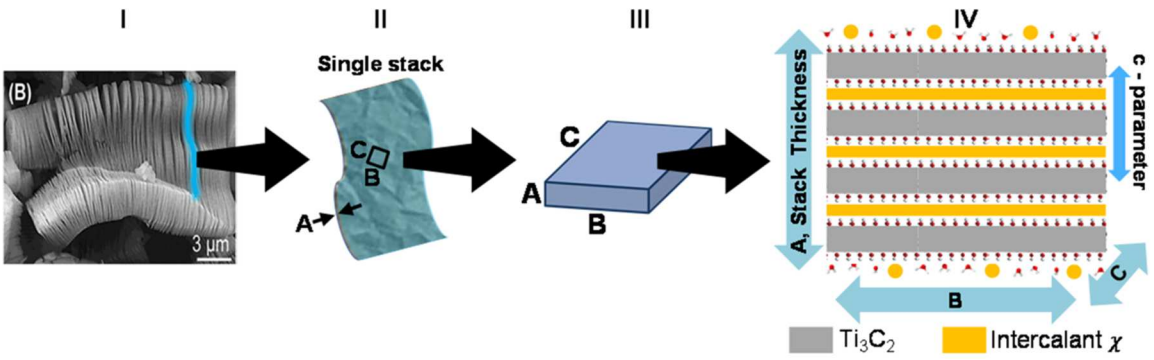

Figure 27*. Structural hierarchy of MXene. (I) Exfoliation of initial Ti_3AlC_2 structure with HF etching; (II) Single MXene stacking with thickness A consisted of several $Ti_3C_2T_x$. layers. The area BC denotes a characteristic microdomain size; (III) parallelepiped microdomain model used in the SANS analysis; (IV) Structural schematic model of a microdomain of thickness A and surface B×C of c-lattice parameter varied according to intercalant species* χ.

SANS analysis was used to investigate $Ti_3C_2T_x$ morphology. The experiment was carried in the low Q range, 0.01-0.2 $Å^{-1}$, in order to better understand the material's interlayer spacings, layer densities, sheet thicknesses, domain sizes, and macroparticle surface roughness values.

4.2.3.1. Interlayer Spacing and Layer Density

The scattering curve collected for $Ti_3C_2T_x$ powder in the 0.4 – 0.1 $Å^{-1}$ range is shown in Figure 28. The pattern for a corresponding MAX phase was also recorded and is shown in Figure 28 as a reference. The positions of the Q_1 peaks, *viz.* 0.618 and 0.718 $Å^{-1}$, corresponded to the *c*-LPs of $Ti_3C_2T_x$ and Ti_3AlC_2 giving the values of 20.33 Å (±0.11) and 17.5 Å (±0.03), respectively. Those were in a very good agreement with the values calculated using the position of (0002) XRD peaks of the corresponding samples (Table 8).

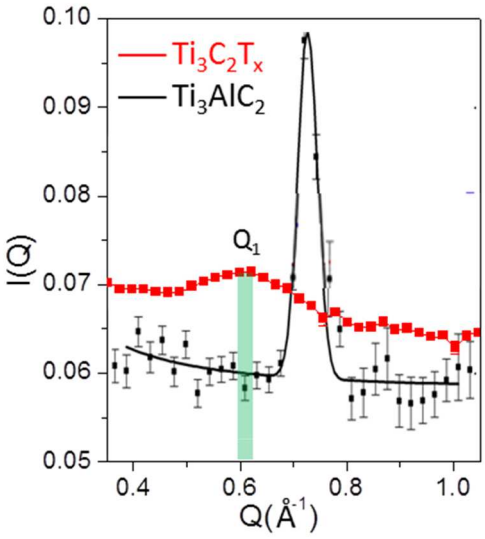

Figure 28. *SANS curves of $Ti_3C_2T_x$ and Ti_3AlC_2 in the 0.4 – 1.0 $Å^{-1}$ region which show the ordering of the $Ti_3C_2T_x$ layers at Q_1.*

Table 8. *Lattice parameter information for $Ti_3C_2T_x$ and Ti_3AlC_2 samples calculated from SANS and XRD data.*

Sample	Q_1 ($Å^{-1}$)	*c*-LP (Å)	Error (Å)	*c*-LP (XRD) (Å)
Ti_3AlC_2	0.718	17.50	±0.03	18.4
$Ti_3C_2T_x$	0.618	20.33	±0.11	20.3
$Ti_3C_2T_x/D_2O$	0.653	19.25	±0.19	–

While the position of the Q_1 peak arises from the *c*-LP of MXene, its intensity is sensitive to the material's density at the nanoscale, being able to recognize and distinguish the difference between the intercalant species χ and *MX* layers.

Two MXene samples, one as-synthesized $Ti_3C_2T_x$ (Figure 28) and one soaked in D_2O (not shown), were used to estimate the skeletal density of the individual $Ti_3C_2T_x$ layer (see Appendix C for more details on calculations). A composition of $Ti_3C_2 + 2(OH)$ and the presence of a layer of water molecules between the layers were assumed for the

as-synthesized $Ti_3C_2T_x$. For the deuterated sample, the assumption was that surface OH groups were replaced by OD groups after soaking for 5 days, and skeletal density of a layer $\Delta\rho_{layer}$ was the neutron scattering length density (NSLD) between D_2O and the MXene. As a result, comparison of $I(Q)$ for the H_2O- and D_2O-hydrated MXene samples gave a MXene density of 5.15 g/cm^3, in close agreement with a theoretical estimate of 5.2 g/cm^3, which was derived using experimental *c*-LP value assuming OH termination of $Ti_3C_2T_x$ surfaces [24].

4.2.3.2. Surface Roughness, Sheet Thickness, and Domain Size

The low Q range, 0.01-0.1 Å^{-1} was used to estimate surface roughness, individual $Ti_3C_2T_x$ sheet thicknesses and the nanosized domain edge lengths A, B, and C, corresponding to the $Ti_3C_2T_x$ stack height and lateral dimensions, respectively (see Figure 27-III for schematic). For this, a SANS pattern was recorded for $Ti_3C_2T_x$ (synthesized by HF etching of Ti_3AlC_2 at RT for 18 hours and then dried in a desiccator for 1 week) over the range of 0.01 – 1.0 Å^{-1} (Figure 29). It revealed a dominant feature (marked as □) at Q-values below 0.1 Å^{-1} – a signal arising from Porod surface scattering factor [84] from the micron-sized $Ti_3C_2T_x$ particles. The value of the exponent – Porod coefficient – in this Q-range was used to characterize the surface roughness (values of 3 and 4 correspond to rough and smooth surfaces, respectively). From the experimental data shown in Figure 29, the Porod coefficient was calculated to be p = 3.43 indicating a relatively rough external surface for the micron-sized $Ti_3C_2T_x$ particles.

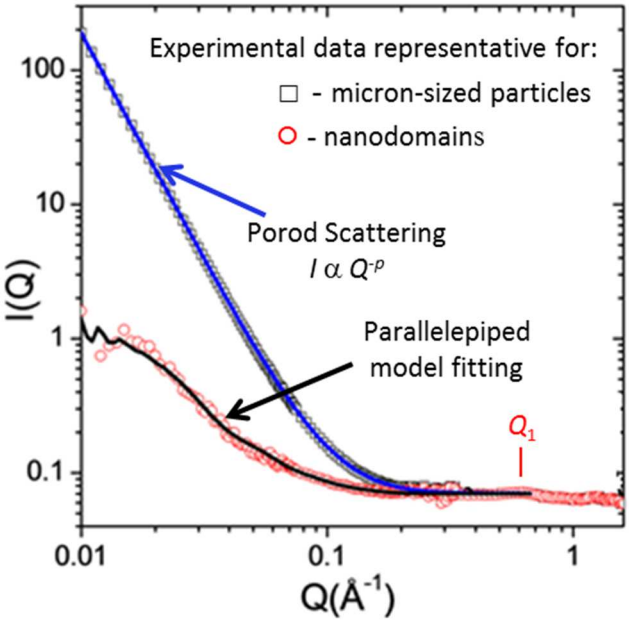

Figure 29. *SANS curve of $Ti_3C_2T_x$. Experimental data are shown by symbols (□ and ○ stands for Porod surface scattering from the micron-sized $Ti_3C_2T_x$ particles and for the shape of the nanodomains, respectively) and solid curves are model fits described in main text.*

Further, subtraction of the Porod scattering revealed the shape of the nanodomains (○) which was modeled by a parallelepiped form factor with edge lengths A, B, and C (see Appendix C for modeling details). The resulting fit (—) was plotted along with the experimental data (○), with the Porod contribution removed in order to highlight the material nanoscale features (bottom curve in Figure 29). The A, B, and C lateral dimensions were found to be 22.9(±1.3), 169(±6) and 196(±7) Å, respectively. Considering that the length A is a measure of the $Ti_3C_2T_x$ stack thickness, the number of layers which comprise each individual domain was thus obtained by dividing edge A by ½ the *c*-LP and found to be ≈ 2 layers per domain.

4.3. Chemical Composition of $Ti_3C_2T_x$

In the early paper first describing the discovery of MXenes [23], it was found that its chemical composition was not controlled. At that time, it was poorly understood why EDX analysis detected O and F elements which varied from sample to sample and how to control them. The only conclusion at that time was that the $Ti_3C_2T_x$ surface was not bare, but terminated primarily by OH groups and some F groups. Thus, more fundamental analysis was performed to better understand the chemical composition of $Ti_3C_2T_x$.

4.3.1. Multilayer Stacks Composition

As mentioned earlier in Chapter 2, reactions (3), (4) and (5) can potentially occur during etching of Ti_3AlC_2. According to reaction 1, the theoretical weight loss after exfoliation should be ≈ 13.9 wt. %. However, if reaction 2 is operative, then a 3.6 % overall weight *gain* should be expected. Experimentally there was essentially no weight change (yield ≈ 100%) after reaction with HF. The actual value was most probably higher because of some material loss during washing and drying of the powders. Assuming that little or no $Ti_3C_2(OH)_2$ dissolved in the HF, this was consistent with the formation of $Ti_3C_2(OH)_2$ and consistent with the conclusion that the overall reaction yield was high [63]. However, this was not always the case; for example, when Ti_2AlC powders were immersed in 50 wt.% HF for extended periods they readily dissolved [63]. It follows that $Ti_3C_2T_x$ could possibly include some secondary phases such as reaction products (*e.g.*, AlF_3) or oxidation products (*e.g.*, $TiOF_2$, TiO_2, etc).

EDX of the exfoliated $Ti_3C_2T_x$ samples dried at RT showed that the average Ti:C:O:F atomic ratios were 37:25:15:25 (Table 9) implying complicated chemistry discussed in Section 4.3.2.

Table 9. *EDX analysis of $Ti_3C_2T_x$ powders etched at room temperature (RT) for 20 h and dried in a desiccator under vacuum, created by a water jet pump (P < 10 Torr) at RT.*

Sample #	Atomic %			
	Ti K	C K	O K	F K
1	36.4	27.6	16.8	15.8
2	37.4	28.2	15.7	14.6
3	40.5	25.9	15.8	16.2
4	41.6	25.1	16.6	14.7
5	33.8	27.4	19.0	17.0
6	35.7	26.6	18.0	16.9
7	38.0	20.7	27.9	13.4
8	36.4	21.6	28.0	11.1
Average	**37.5**	**25.4**	**19.7**	**15.0**

4.3.2. Surface Terminations

4.3.2.1. Chemical Bonding

To gain more insight into the surface chemistry, freshly prepared $Ti_3C_2T_x$ samples (etched in 50 wt.% HF for 18 hours and dried in a desiccator for 24 hours) were analyzed using XPS. Survey showed strong signals from Ti, C, O, and F elements (Figure 30A), which agreed with the EDX results. It also showed the presence of small amount of Al, which was most likely due to unwashed by-products (AlF_x or AlO_xF_y) of the Ti_3AlC_2 etching reaction. High resolution spectra were recorded for those elements in the corresponding regions to understand the nature of the chemical bonding in the sample.

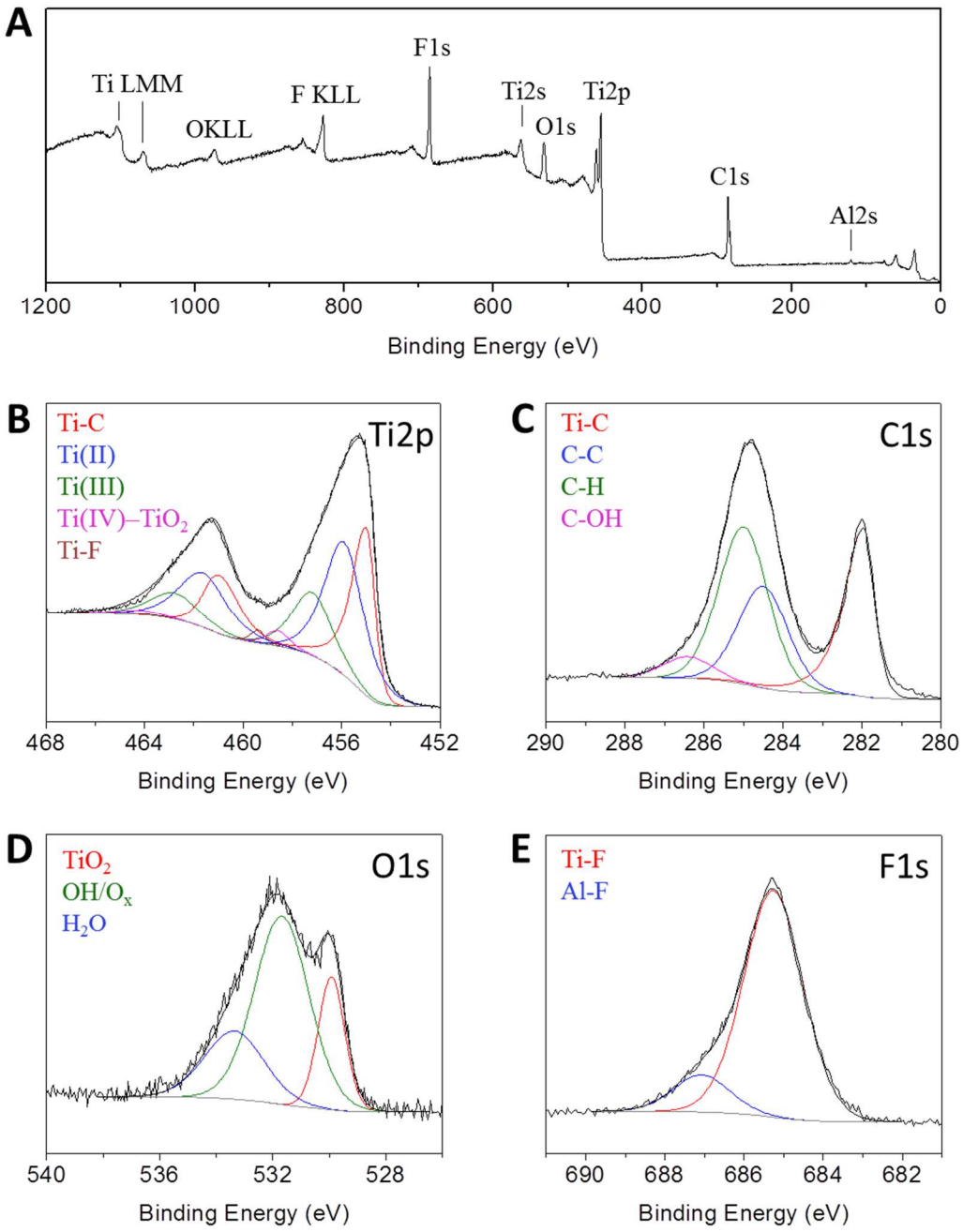

Figure 30. *XPS spectra for $Ti_3C_2T_x$ powder: (**A**) survey, (**B-E**) high resolution spectra of Ti2p, C1s, O1s, and F1s regions, respectively.*

High-resolution XPS spectra in the Ti2p region of the powder revealed peaks that could be deconvoluted into components corresponding to Ti bound to C, Ti (II), Ti (III),

Ti (IV) and/or Ti bound to F (Figure 30B). The Ti-C signal arises from Ti atoms in the interior of the MXene layers [85-87]. Ti signals with oxidation states ranging from II to IV indicated the formation of different mixed oxides (TiO_xF_y) and carboxides (TiC_xO_y) evidencing the non-uniform termination of the $Ti_3C_2T_x$ surface. A Ti(IV)-O signal arose due to oxidation of $Ti_3C_2T_x$ layers at their edges or at the sites of defect formation, which was expected to occur when materials were exposed to oxidative media (see Section 4.6.3 for more details). Ti-F signals were observed in both Ti2p and F1s regions (Figure 30B and E, respectively) confirming F termination of $Ti_3C_2T_x$ surface due to HF etching.

The high resolution spectrum in the O1s regions (Figure 30D) confirmed the formation of Ti(IV) oxide, and showed the presence of OH/O_x groups, most likely bound to the MXene surfaces.

Besides the Ti-C signal from the MXene's inner layers, C-C, C-H, and C-OH signals were detected in the C1s region (Figure 30B). Those may arise from hydrocarbons trapped at the $Ti_3C_2T_x$ surface during washing/drying procedure after HF etching. C-C could also be detected due to $Ti_3C_2T_x$ oxidation resulting in the formation of TiO_2 and leaving carbon atoms' network behind.

Overall, XPS analysis suggested $Ti_3C_2T_x$ termination with primarily O and some F containing groups and the formation of various Ti oxides, indicating a very complicated chemistry of this material.

4.3.2.2. Position of Surface Groups

Considering that MXene properties were predicted to depend on the positions of surface groups, atomic pair distribution function (PDF) analysis of $Ti_3C_2T_x$ was carried

out to define their coordinates (see Appendix D for more details). Following a trial and error approach, different positions of Ti_3C_2 layers with respect to each other in a unit cell and different special positions for surface terminating groups (F and OH) were systematically analyzed aiming to find those of the best fit to the structure with *c*-LP of 19.8 Å, based on the lowest agreement factor R_w.

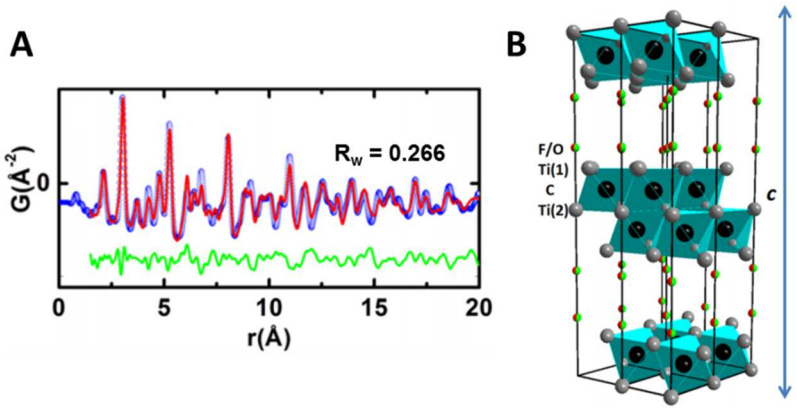

***Figure 31**. (**A**) PDF fits of pristine $Ti_3C_2T_x$: blue circles are the measured data, red solid lines are the calculated PDFs of the best-fit structural models, and the green solid lines offset below are difference solid lines. (**B**) The polyhedral representation of optimized $Ti_3C_2T_x$ structure: Ti, C, O/F atoms are in grey, black, and red and green colors. Different Ti atoms are marked with numbers for convenience.[88]*

Figure 31A shows the optimum fit to the experimental PDF for pristine $Ti_3C_2T_x$. The structure of $Ti_3C_2T_x$, where Ti1 stands for the top and bottom Ti atoms of a Ti_3C_2 layer, is shown schematically in Figure 31B. The best agreement with the experimental PDF ($R_w \approx 0.266$) was thus obtained for the structure where C, Ti1 and Ti2 atoms were sitting at the (1/3, 2/3, *z*), (2/3, 1/3, *z*), and (0, 0, 0) positions, respectively, and surface functionalities were at the (0, 0, *z*) position. The fit (red solid line in Figure 31A) indicated that the peaks were in the right positions, suggesting that the overall structure is

correct. However, the R_w values (0.266) were high, and there were a lot of unfit signal in the residuals (see green solid line) suggesting that this structural model was not complete. The likely reason was unaccounted for disorder in the structure, either of the interlayer stacking or in the form of defects in the layers themselves due to bending, for example. These effects are common in lamellar materials but were not included in the structural model which assumed a perfectly ordered 3D structure.

4.4. Properties of $Ti_3C_2T_x$

4.4.1. Electrical Resistivity

Changes in resistivity were expected upon A-element etching from MAX phase structures. The resistivity values are very important for any application in energy storage. A detailed study was thus conducted to determine how the resistivity changed upon MXene exfoliation.

Measurements were conducted on cold pressed discs of powders (1 GPa) etched for different periods of time at RT. Changes in the sheet resistivities of cold pressed MXene as a function of etching time are shown in Figure 32. A dramatic increase of resistivity was observed during the first 2 h of reaction. This was due to the replacement of the metallic-like bonded Al layers with more insulating O or OH ligands, which were presumably covalently bonded to the $Ti_3C_2T_x$ layers and interacted only via weak hydrogen and/or van der Waals bonds. Following the sudden increase, no large changes were observed for the next 8 h. However, after 10 h of etching, another increase in resistivity was observed. These results are not too surprising since MXenes were expected to have good in-plane, but poor out of plane, conductivities. The results also

suggested that a MXene percolation threshold was reached after the first 2 h of etching. Based on the results of Figure 22, 2 h of etching corresponded to ~ 60 wt.% fraction of $Ti_3C_2T_x$ present in the etched Ti_3AlC_2 sample. The second increase in resistivity was probably caused by the formation of an insulating titanium oxyfluoride ($TiOF_2$) phase on the MXene surface (see Figure 20B). The presence of this phase was confirmed by the presence of an XRD peak at 23.6° corresponding to a major (100) peak of $TiOF_2$ (Figure 20B).

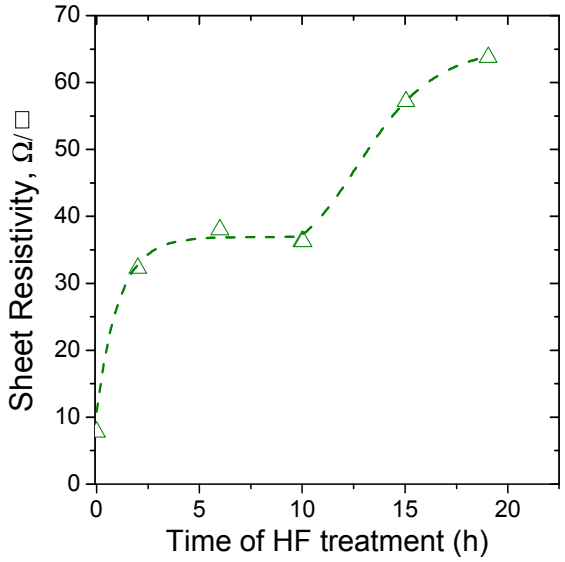

Figure 32. *Effect of reaction time at RT on sheet resistivity of cold pressed discs; with increasing reaction time, the sheet resistivity increased.[75]*

4.4.2. Surface Charges

Figure 33 shows the Zeta potential of $Ti_3C_2T_x$ flakes in aqueous colloidal solution measured using dynamic light scattering. The value of the zeta potential was found to be

around -45 eV indicative of negatively charged particles and suggesting a very stable colloidal solution.

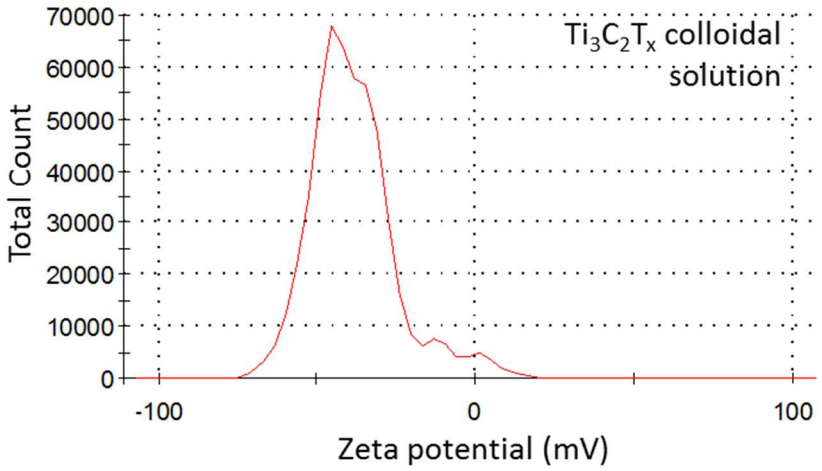

Figure 33. *Zeta potential of $Ti_3C_2T_x$ flakes in aqueous colloidal solution.*

4.4.3. Adsorptive Properties

4.4.3.1. Adsorption Capacity toward Organic Dyes

The adsorption kinetics of the dyes onto $Ti_3C_2T_x$ was studied in a set of experiments. Since $Ti_3C_2T_x$ was reported to have negatively charged surfaces [89], the effects of the adsorptive charge in this process were investigated. For this, methylene blue, MB (a cationic dye), and acid blue, AB80 (an anionic dye), were selected (their chemical structures are shown as insets in Figure 34A).

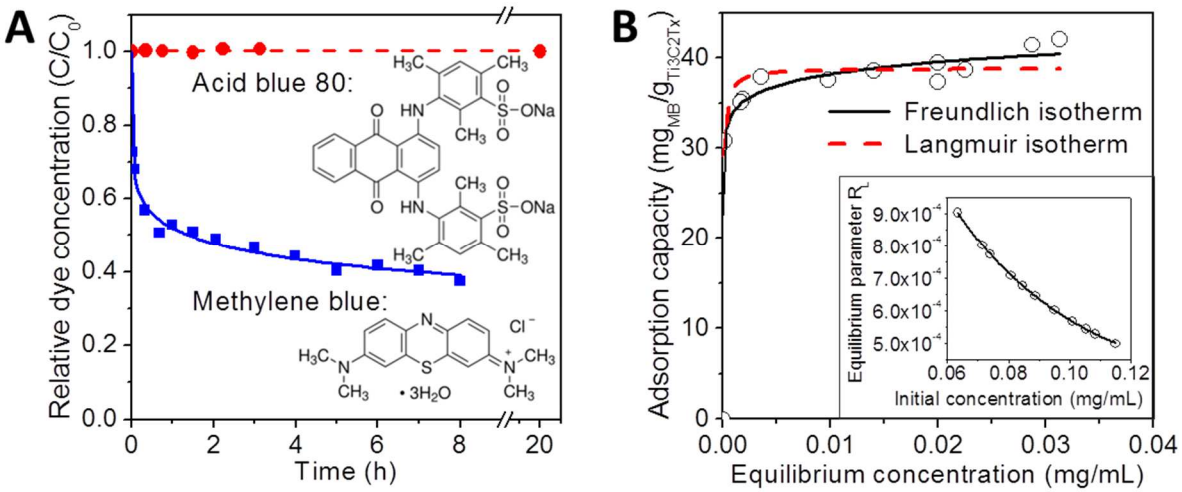

***Figure 34**. (**A**) Time dependence of methylene blue (C_0 = 0.05 mg/mL) and acid blue 80 (C_0 = 0.06 mg/mL) concentrations in aqueous solutions with suspended $Ti_3C_2T_x$ particles in the dark. Chemical structures of corresponding dyes are shown as insets. (**B**) Adsorption isotherms of methylene blue on $Ti_3C_2T_x$. Inset shows dependence of the equilibrium parameter R_L (see Eq. E-2, Appendix E) on initial concentration, C_0, of a dye.[90]*

Figure 34A shows the time dependence of the $Ti_3C_2T_x$-mediated removal of each dye from solution in the dark. While, even after 20 h, there were no changes in the AB80 concentration, a dramatic decrease of MB concentration was observed within the first 8 h. From these results, it is reasonable to assume that the preferential adsorption of the cationic dye, MB, over the anionic dye, AB80, in the dark was primarily due to favorable electrostatic interactions between the MB molecules and the MXene surfaces.

Adsorption isotherms of MB on $Ti_3C_2T_x$ are shown in Figure 34B. Two models, Langmuir [91, 92] and Freundlich [93], were used to fit the experimental data (details on the models and corresponding equations can be found in Appendix E). The best fitting parameters of both the Langmuir and Freundlich isotherms (Figure 34B) together with their correlation coefficients are presented in Table 10. High values of K_L, a constant

which characterizes the strength of adsorbate binding to the adsorbent, suggested that MB binds strongly to $Ti_3C_2T_x$. The separation factor, R_L, calculated from the Langmuir isotherm using Eq. E-2 (Appendix E) was plotted *vs.* initial MB concentrations (inset in Figure 34B). The R_L values were close to zero (10^{-5}–10^{-4} for the range of MB concentrations explored), suggesting nearly irreversible adsorption [92]. Pearson's correlation coefficient, *R*, for the Freundlich isotherm was higher than the corresponding value for the Langmuir isotherm (Table 10), meaning that the Freundlich model was an overall better fit of the experimental data (Figure 34B). The value of the constant *v* (Eq. E-3, Appendix E) was larger than 1 which also indicated favorable adsorption in the Freundlich model [93]. The fact that the Freundlich model better described adsorption was consistent with the presence of heterogeneous adsorption sites on the MXene surfaces, a reasonable conclusion given that, as noted above, the MXenes were primarily terminated by a mix of OH, O and F.

Table 10. *Fitting parameters for Langmuir and Freundlich isotherms for methylene blue on $Ti_3C_2T_x$. [90]*

Langmuir isotherm	Freundlich isotherm
A_{max} = 38.851 mg/g	ν[b)] = 19.963
K_L = 1.743 × 104 mL/mg	K_F[b)] = 48.152
R[a)] = 0.811	R[a)] = 0.928

[a)] Pearson's correlation coefficient.
[b)] Values calculated for C expressed in mg/mL and A in mg/g.

The adsorption capacity of $Ti_3C_2T_x$ for MB was ~ 39 mg/g (Table 10). This value was smaller than typically observed for commercial activated carbons (up to 1000 mg/g) [94] but comparable with other materials of similar structure and surface areas (from ~14 mg/g for raw kaolinite [95], up to ~ 290 mg/g for commercial montmorillonite clays [96]). This suggested that MXenes, with their tailorable compositions and surface chemistries, might be better adsorbents than other 2D materials.

4.4.3.2. Structural Changes Upon Adsorption

When an aqueous 0.05 mg/mL MB solution was kept in contact with suspended $Ti_3C_2T_x$ particles in the dark, the MB concentration continued to decrease steadily over a period of days after the initial rapid drop during the first 2 h (Figure 34A). To better understand the reason for this slow concentration decrease, the $Ti_3C_2T_x$ structure after MB adsorption was studied. According to XRD analysis of recovered MXene powders (Figure 35), after the 2 h adsorption in the dark, no changes in the position of the (0002) XRD peak were observed. In contrast, after 20 h of adsorption, a small shift of the (0002) peak toward lower angles was detected. In addition, this peak broadened, suggesting imperfect stacking in the [000l] direction. Because of the ability of cations to intercalate MXenes [89], and the intercalation of dyes reported for many layered materials [97, 98], the possibility of MB intercalation into $Ti_3C_2T_x$ was considered. According to XRD (Figure 35) the value of the *c*-LP increased by 2.0 Å. The MB molecule dimensions are ≈ 17.0×7.6×3.25 $Å^3$ ($l \times w \times h$) [99]. Assuming that one MB molecule intercalated into the interlayer space between the $Ti_3C_2T_x$ sheets in an orientation parallel to the surfaces, the anticipated increase in *c*-LP should be at least 3.25 Å, i.e. 1.5 times the observed

increase. Thus, the 2 Å increase in the interlayer space of $Ti_3C_2T_x$ was not enough to accommodate a MB molecule. Still, partial wedging-in of MB molecules at the particles' edges, could in principle cause their opening and result in the observed increase of the *c*-LP.

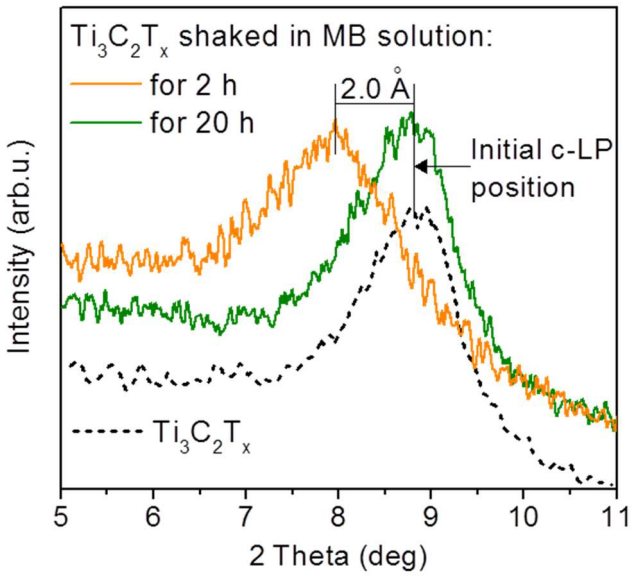

***Figure 35**. XRD patterns around the $Ti_3C_2T_x$ (0002) peak after soaking in aqueous 0.05 mg/mL methylene blue solution for 2 h and 20 h.[90]*

As discussed in Section 4.6.3.1, $Ti_3C_2T_x$ sheets in aqueous solutions slowly react with water, and transform into titanium hydroxide. This intrinsic instability in water provides an alternative explanation for the observed increase in *c*-LP. This transformation, that initiates at the particles' edges, could again wedge open the layers resulting in broader 0002 peaks. Interestingly, keeping the $Ti_3C_2T_x$ powder in a MB

solution for up to 7 days had no further effect on the *c*-LP values. Clearly, more work is needed to better understand the reasons for the shifts in LPs.

4.4.4. Photocatalytic Properties

To shed light on whether MXene can assist in degradation of the organic pollutants and, as a result, be suitable for environmental applications, the study of its photocatalytic property was carried out.

Figure 36 compares the time dependencies of the relative concentrations of MB and AB80 (cationic and anionic dyes, respectively) in water in the presence of $Ti_3C_2T_x$, while exposed to UV irradiation, with those for samples held in the dark. In particular, in the case of AB80 in the presence of $Ti_3C_2T_x$ – where no changes in dye concentration were observed over 20 h in the dark – fast photodegradation occurred under UV light (Figure 36B). As a result, 5 h irradiation led to a decrease of the solution concentration of AB80 by 62 %. Similarly, 81 % of the MB was degraded while in contact with suspended $Ti_3C_2T_x$ during UV irradiation over 5 h, whereas only 18 % (almost 4 times less) of MB was removed in the dark (Figure 36A). Photolysis of the dyes under UV light was excluded by running separate experiments with dye solutions of the same concentrations, containing no $Ti_3C_2T_x$ (see Figure 37).

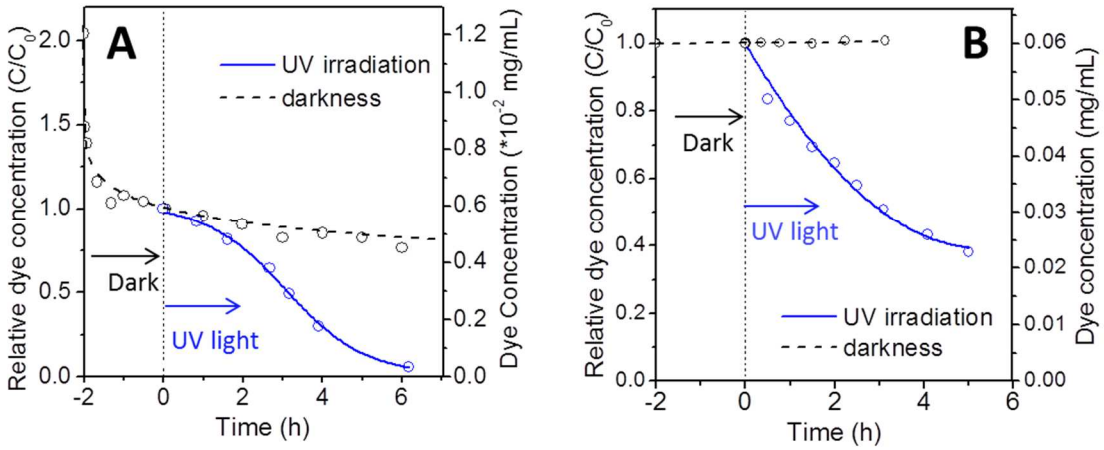

***Figure 36**. Time dependence of relative concentrations, C/C_0, of, (**A**) methylene blue and, (**B**) acid blue 80 in $Ti_3C_2T_x$ containing solutions. Solid and dashed lines correspond to measurements taken under UV light and in the dark, respectively.[90]*

Considering the instability of $Ti_3C_2T_x$ in water, it was likely that the formation of titanium hydroxide and/or TiO_2 – both known to have distinct photocatalytic activities [100-103], – on the MXene surfaces contributed to the photocatalytic effect observed under UV illumination. This again implied that the photocatalytic mechanisms in the presence of $Ti_3C_2T_x$ were quite complicated and warrant deeper study. These comments notwithstanding, the metallic character and the electrical conductivity of $Ti_3C_2T_x$ observed in thin film measurements [104] suggested the presence of free electrons in the carbide layer underneath the oxide surface. Therefore, similar to graphene-titania composites [105-108], this suggested that $Ti_3C_2T_x$ supported TiO_2 composites may be a promising material for catalysis, energy conversion and energy storage applications.

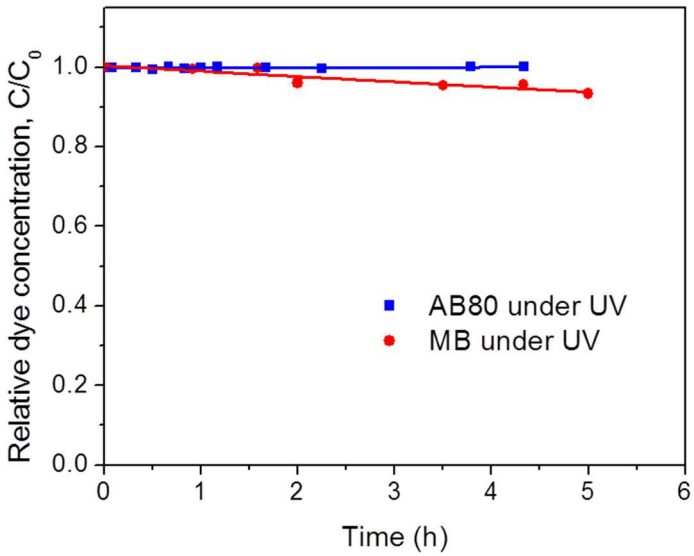

Figure 37*. Time dependence of photolysis – i.e., light induced degradation in the absence of* $Ti_3C_2T_x$ *– of methylene blue and acid blue 80 in aqueous solutions under UV irradiation. Each sample was measured three times.*

4.5. Intercalation and Delamination

4.5.1. Intercalation of Ionic Species

To gain insight into MXenes' potential in the energy storage field, their ability to accommodate ions between the layers was explored, which has been neither theoretically predicted nor experimentally demonstrated yet.

4.5.1.1. Intercalation of Metal Cations

A large number of salts and bases were explored (see Table 11). As an example, XRD patterns (Figure 38A-C) showed that, after placing the $Ti_3C_2T_x$ multilayered stacks in solutions of the salts, there was a downshift in the (0002) peak position. This downshift showed that in all cases there was an increase in the *c*-LP. For example, the *c*-

LP of $Ti_3C_2T_x$ changed from 20.3 Å to up to 25.4 Å, in the case of KOH and NH_4OH (Figure 38A).

Table 11. *Changes in c-lattice parameters (c-LPs) after intercalation of $Ti_3C_2T_x$ with ions. Value of Δ (fourth column) indicates the increase of the c-LP of $Ti_3C_2T_x$ after intercalation (third column) compared to initial c-LP of 20.3 Å.*

Intercalant	Chemical formula	*c*-LP, Å	Δ, Å
Intercalants which possess a basic character when dissolved in water			
Potassium hydroxide	KOH	25.4	5.1
Ammonium hydroxide	NH_4OH	25.3	5.0
Sodium carbonate	Na_2CO_3	25.3	5.0
Sodium hydroxide	NaOH	25.1	4.8
Sodium formate	HCOONa	24.9	4.6
Sodium citrate	$Na_3C_6H_5O_7$	24.9	4.6
Sodium acetate	CH_3COONa	24.8	4.5
Potassium acetate	CH_3COOK	24.6	4.3
Lithium acetate	CH_3COOLi	24.5	4.2
Intercalants which possess a nearly neutral or acidic character when dissolved in water			
Zinc sulfate	$ZnSO_4$	21.7	1.4
Potassium sulfate	K_2SO_4	21.4	1.1
Magnesium sulfate	$MgSO_4$	21.3	1.0
Ammonium tetrafluoroborate	NH_4BF_4		1.0
Sodium sulfate	Na_2SO_4	21.0	0.7
Potassium chloride	KCl	20.5	0.2
Magnesium chloride	$MgCl_2$	20.5	0.2
Sodium chloride	NaCl	20.5	0.2
Potassium iodide	KI	20.4	0.1
Aluminum chloride	$AlCl_3$	20.3	0

Not all salts behaved similarly. In the case of high-pH solutions, such as KOH, NH_4OH, NaOH, and several others (Figure 38A and C; also see Table 11), the changes in *c*-LPs were large. Conversely, close-to-neutral solutions – such as Na-, K-, and Mg-

sulfates, resulted in significantly smaller changes in *c*-LPs (Figure 38B; also see Table 11). No shifts in the (0002) peaks were observed when $Ti_3C_2T_x$ was immersed in acetic or sulfuric acid. These observations strongly suggested a *pH dependent* interaction.

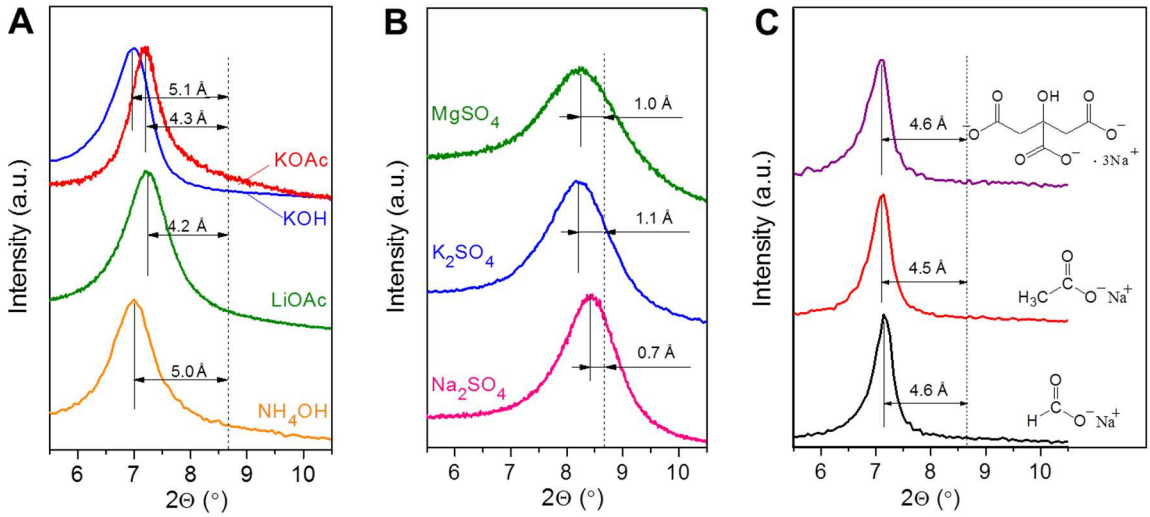

Figure 38. *XRD patterns of various salts and bases: (**A**) compounds which form basic solutions when dissolved in water, (**B**) sulfate salts which form nearly neutral solutions when dissolved in water and, (**C**) Na-salts with different organic anions. In all figures the location of the $Ti_3C_2T_x$ peak before immersion in the salt solutions is depicted by dashed vertical line. In all cases, the c-lattice parameter increased by the values shown and ranged from a high of 5 Å to a low of 0.7 Å. [89]*

In order to shed light on whether the cations or anions intercalated the $Ti_3C_2T_x$ layers, three Na-salts – with differing anion radii – were tested. The results (Figure 38C) showed that the expansions in *c*-LPs were comparable and independent of anion radius. Furthermore, EDX analysis of $Ti_3C_2T_x$ after treatment in the different sulfate salts, shown in Figure 38B, confirmed the presence of the cations; sulfur was not detected (Table 12), confirming that the cations intercalated between the $Ti_3C_2T_x$ layers, while the anions

stayed in the solution. Moreover, the process appeared to be *cation nature dependent* – monovalent cations readily intercalated into the MXene structure whereas multivalent, *viz.* Al^{3+}, did not. However, it is important to note that the intercalation of multivalent ions could be promoted electrochemically [89].

***Table 12**. EDX analysis of $Ti_3C_2T_x$ powder before and after intercalation.[89]*

Material	Atomic %					
	Ti	C	O	F	Cation of electrolyte	S
$Ti_3C_2T_x$	30.0	14.8	16.0	18.9	-	-
$Ti_3C_2T_x$ + KOH	30.0	21.2	30.9	11.4	3.2	-
$Ti_3C_2T_x$ + NaOAc	30.0	16.2	18.2	27.4	5.5	-
$Ti_3C_2T_x$ + K_2SO_4	30.0	17.8	8.4	15.4	1.4	0.0
$Ti_3C_2T_x$ + Na_2SO_4	30.0	17.5	12.9	15.8	1.0	0.0
$Ti_3C_2T_x$ + $MgSO_4$	30.0	29.7	17.0	18.5	0.5	0.1

*Values of the carbon, oxygen and fluorine content are unreliable, since EDX was collected from rolled $Ti_3C_2T_x$ electrodes, which contained carbon additive (which contributed to the C and O content) and PTFE binder (which contributed to the C, O and F content)

It was also found that the *c*-LPs of intercalated material depended on how dry the sample was. Thus, the *c*-LP values of as-prepared wet material were much larger compared to the one found for samples dried in a desiccator. Figure 39 shows the case for Na intercalated $Ti_3C_2T_x$ revealing an upshift of (0002) XRD peak by 4.9 Å after drying the sample for 5 days. It is thus reasonable to assume that *co-intercalation of water* molecules occurred together with Na^+ entering the MXene structure, most likely appearing as a hydration shell of water molecules around the cation.

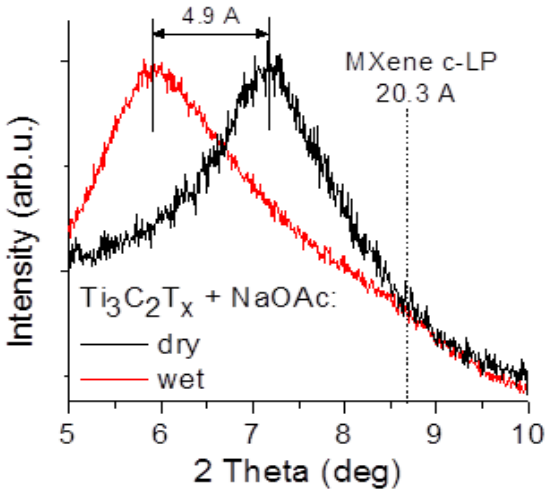

Figure 39. *Effect of 5-day drying on c-LP value of $Ti_3C_2T_x$ intercalated using 1M NaOAc aqueous solution.*

The above observations can be illustrated by the schematic shown in Figure 40, showing spontaneous intercalation of cations, co-intercalated with water, from aqueous salt solutions between the 2D $Ti_3C_2T_x$ layers, resulting in the increase in interlayer distance.

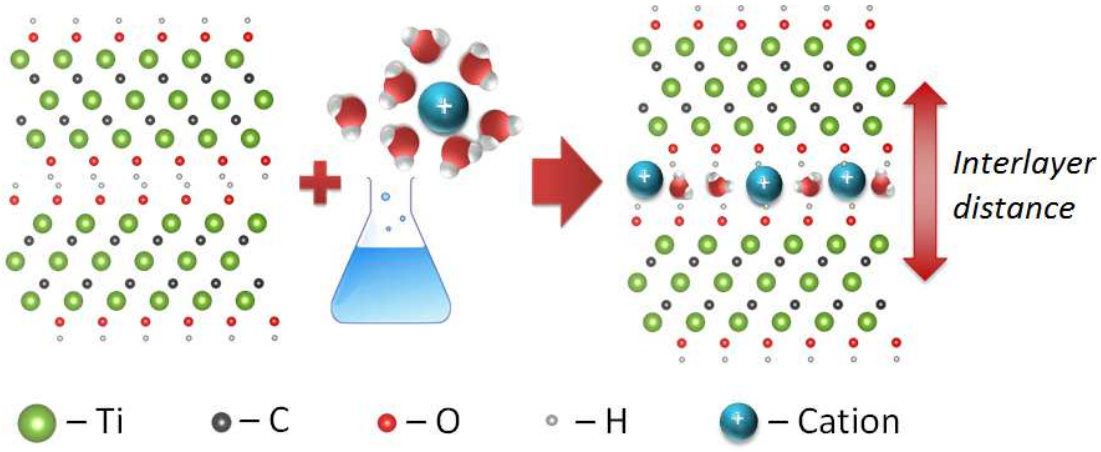

Figure 40. *Schematic of the intercalation of cations between $Ti_3C_2T_x$ layers.[89]*

To understand whether any structural changes beyond the increase in *c*-LP value occurred upon ion intercalation, PDF analysis of the KOH and NaOAc intercalated $Ti_3C_2T_x$ samples was performed. The left panel in Figure 41 compared the experimental PDFs of the intercalated compounds (blue and red for KOH- and NaOAc-$Ti_3C_2T_x$, respectively) with the PDF of the pristine compound (black curve). As is evident in the high-*r* region, the intercalation shifted the PDF peaks to lower *r* value, that was more obvious for the K^+ insertion. Considering that the PDF peaks were predominantly intralayer peaks, the shift indicated contraction of the in-plane *a*-LPs upon intercalation – 3.0399(4) and 3.0301(4) Å for K^+ and Na^+ intercalated compared to 3.0505(5) Å for the pristine $Ti_3C_2T_x$ (Numbers in parentheses are the estimated uncertainties on the last reported digit).

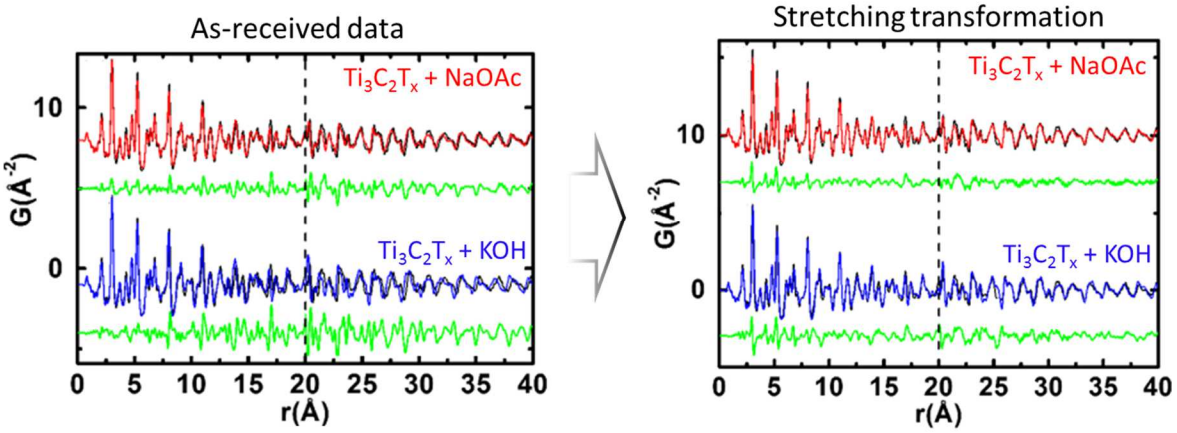

Figure 41. *Comparison between experimental PDFs of pristine and intercalated $Ti_3C_2T_x$. The black curve is the PDF from the pristine sample; red and blue is the PDF of the NaOAc and KOH intercalated samples, respectively. The green curve offset below is the difference curve. Data in the high-r region from 20 to 40 Å are magnified 2 times for clarity. On the left, the stretching transformation was not applied to the intercalated samples and the difference curve was dominated by the effects of the change in lattice parameters. On the right, the measured PDFs of the intercalated $Ti_3C_2T_x$ have had a stretching algorithm applied to minimize the effects of lattice parameter variation in order to search in the difference curve for a clear signal coming from the intercalants themselves. [88]*

When a stretching algorithm was applied to minimize the effects of lattice parameter variation (right panel in Figure 41), small features were observed in the residual at low *r*, even as the intermediate and higher-*r* regions become well accounted for. The stretch that fixes the high-*r* region overcompensated for small differences at low r suggesting that the near-neighbor bonds were not much perturbed by the intercalation, but there was a larger contraction over a wider range. It was not clear what produced this effect. It might be explained if doped charge from the intercalant ions was trapped in localized defect states rather than in the chemical bonds of the Ti-C network itself. The localized charges produce an electric field which resulted in an overall contraction of the lattice but taking advantage of weaker bond-bending relaxations rather than shortening stiff covalent bonds themselves. Similar effects have been seen in covalent alloys [109, 110]. Despite these issues, the PDF fits carried out on the K^+ and Na^+ intercalated $Ti_3C_2T_x$ samples (Figure 41) revealed no additional features originating from the intercalant ions, indicating that these ions were disordered and did not sit at well-defined locations. Their presence in the actual structure was indicated by the presence of a long wavelength dip in the residual function of the fits to the intercalated data

It is also worth of noting that Raman spectra taken for pristine and K^+, Na^+ and Mg^{2+} intercalated $Ti_3C_2T_x$ also indicated some structural changes upon intercalation. The spectra for K^+ and Na^+ intercalated samples (Figure 42) showed a noticeable blue shift of the modes around 700 cm^{-1} and significant changes in the intensities of other modes in the lower wavelength number range. It can be indicative of some compressive strain in the material, changes in chemical interaction, *etc.* but much deeper analysis, together with

theoretical simulations for modes assignments, would be required to get a better understanding of Raman signals from MXenes.

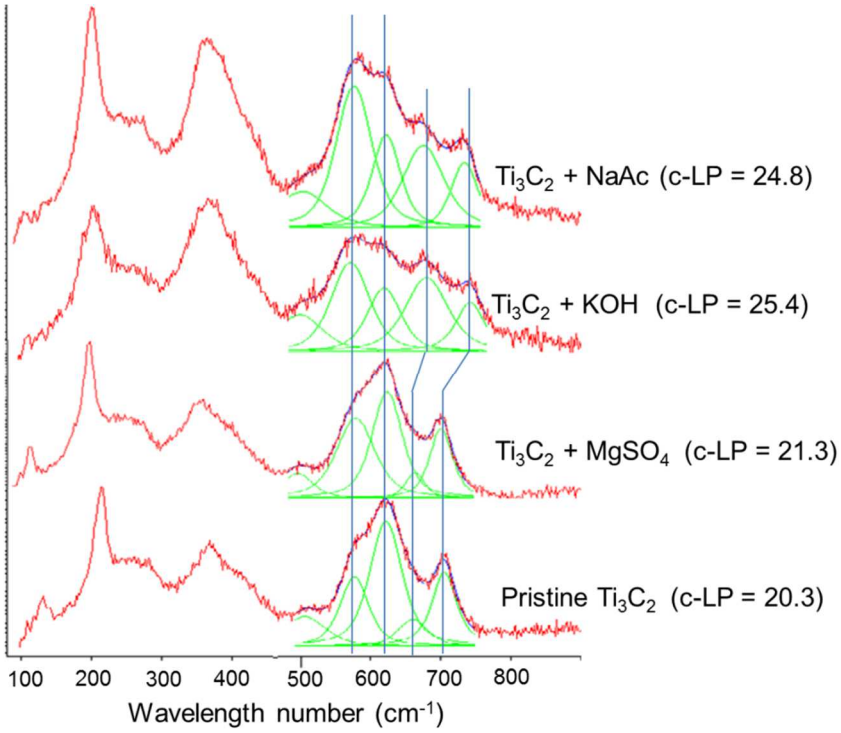

***Figure 42**. Raman spectra for pristine $Ti_3C_2T_x$ and K^+, Na^+ and Mg^{2+} intercalated $Ti_3C_2T_x$.*

4.5.1.2. Intercalation of Organic Cations

Following the idea of cation intercalation, it was expected that insertion of larger species into MXene structure would weaken the intralayer bonding and lead to delamination of multilayered MXene into single sheets. Thus, the feasibility of large organic cations insertion into $Ti_3C_2T_x$ structure was studied using tetraalkylammonium salts (see Table 13). Among those, only TMA-OH/methanol treatment of $Ti_3C_2T_x$ for 1 day led to a significant expansion of the structure with an increased *c*-LP value by 9.3 Å.

Considering that TMA-OH was the only compound in the list which possessed strong basic behavior, the result agreed with previously made conclusion about the *pH dependent* interactions and better cation intercalation from high-pH solutions.

Table 13. *Changes in c-lattice parameters (c-LPs) after intercalation of $Ti_3C_2T_x$ with organic cations. Value of Δ (sixth column) indicated the increase of the c-LP of $Ti_3C_2T_x$ after intercalation compared to initial c-LP of 20.3 Å.*

Chemical compound		Solvent	Treatment time	Chemical formula of the compound	Δ *c*-LP, Å
TMA^+	OH^-	Methanol	1 day	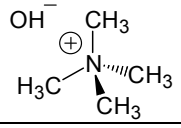	9.3
	BF_4^-	ACN	1 day	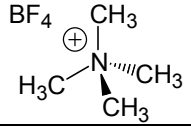	1.7
	Cl^-	Methanol	1 day	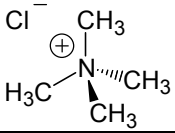	2.5
TBA^+	BF_4^-	Methanol ACN ACN	1 day 1 day 7 days	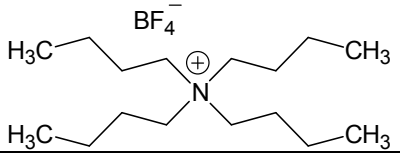	1.5 1.5 22.6
CMA^+	Br^-	Methanol	1 day	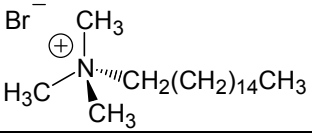	0 broadening
NH_4^+	BF_4^-	Methanol	1 day	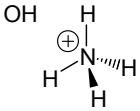	1.0
EMI^+	$TFSI^-$	–	5 days	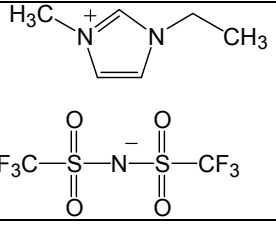	0

<u>*Note*</u>: TMA^+, TBA^+, and CMA^+ stand for tetramethylammonium, etrabuthylammonium, and cetyltrimethylammonium cations; EMI-TFSI stands for 1-ethyl-3-methylimidazolium bis(trifluoromethyl-sulfonyl)imide, respectively.

In addition, $Ti_3C_2T_x$ treatment with TBA-BF_4 in ACN for different periods clearly showed that intercalation was *time dependent*. Thus, small preopening of the structure by 1.5 Å was observed after 1 day of treatment while complete intercalation occurred after 7 days of treatment showing an increase of *c*-LP by 22.6 Å (Table 13). This implied that intercalation of other large cations may be possible when prolonged treatments are applied.

No intercalation occurred when $Ti_3C_2T_x$ was mixed with the ionic liquid, EMI-TFSI, and shaken for 5 days which might be due to high viscosity of the reactive liquid at RT.

4.5.2. Intercalation of Neutral Molecules

Hydrazine, N_2H_4, was the first non-ionic chemical compound which exhibited the intercalation property of $Ti_3C_2T_x$. The original aim of the hydrazine work was to reduce the $Ti_3C_2T_x$ surfaces to create Ti-terminated surfaces that theory predicted would be magnetic [27]. A review of the graphene literature made it clear that hydrazine monohydrate $N_2H_4{\cdot}H_2O$ (HM) dissolved in DMF was the reactant of choice [111]. However, in this case HM was found to primarily act as an intercalant rather than a reducing agent. Furthermore, since the layered structure of MXenes retained some similarities to clays [23], the intercalation chemistries of the latter were reviewed. Numerous compounds, such as formamide and its derivatives, dimethyl sulfoxide (DMSO), urea, long-chain alkylamines, among others have been shown to intercalate clays [112]. While searching for other potential intercalants for $Ti_3C_2T_x$, the research was focused on the first agent, *viz*. hydrazine.

4.5.2.1. Hydrazine Intercalation

4.5.2.1.1. Intercalation of $Ti_3C_2T_x$

A schematic of the intercalation of HM into $Ti_3C_2T_x$ is shown in Figure 43.

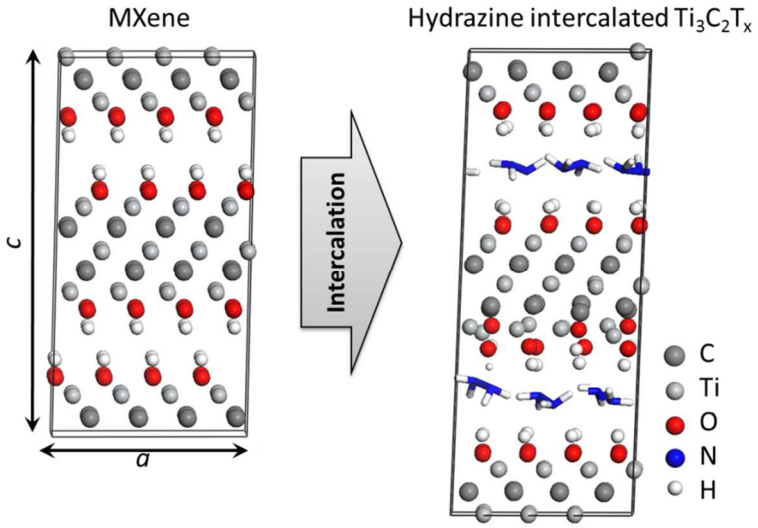

Figure 43. *Schematic of intercalation of $Ti_3C_2T_x$ with HM.[87]*

XRD analysis showed that after intercalation with HM and/or DMF, the (000l) peaks were still present, but shifted to lower 2θ angles (Figure 44A and B). Table 14 summarizes the *c*-LPs values for $Ti_3C_2T_x$ treated with HM and HM in DMF. The initial *c*-LP was 19.5±0.1 Å, a value that did not change much with post-intercalation drying (Table 14). After exposure to HM or HM in DMF at 80 °C for 24 h, the *c*-LPs increased to 25.48±0.02 Å and 26.8±0.1 Å, respectively. The larger *c*-LP increase in the latter case pointed to a synergistic effect when HM was dissolved in DMF, prior to its intercalation.

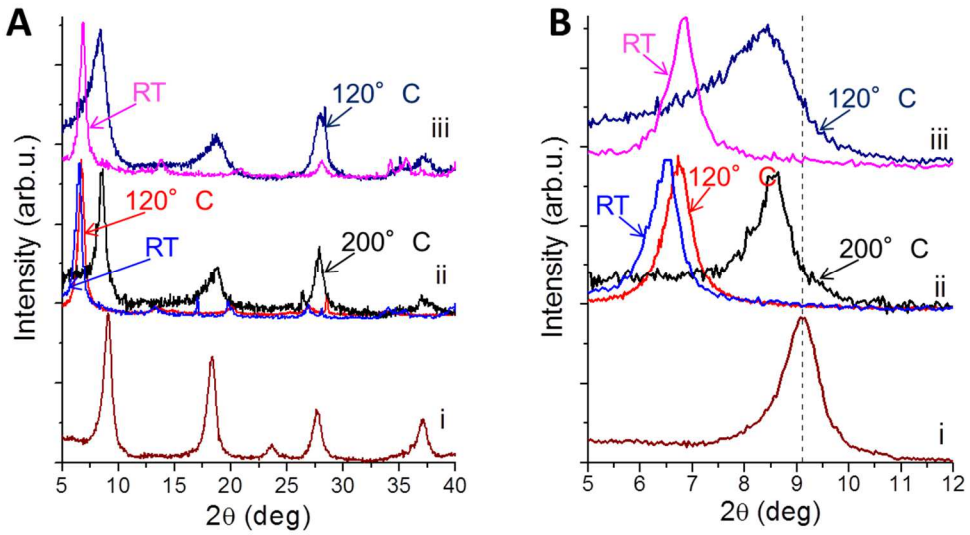

***Figure 44**. (**A**) XRD patterns of $Ti_3C_2T_x$: i) as-received, before any treatment, ii) after hydrazine monohydrate (HM) in N,N-dimethylformamide (DMF) treatment, washed with DMF, iii) after HM treatment, washed with ethanol, and dried at different conditions. (**B**) Zoom-ins of b in the 5-12° 2θ range showing (0002) peaks. [87]*

***Table 14**. c lattice parameters, in Å, for non-intercalated $Ti_3C_2T_x$ and $Ti_3C_2T_x$ powders treated with hydrazine monohydrate (HM), HM and N,N-dimethylformamide (DMF), and dried under different conditions. [87]*

Intercalant	Non-intercalated	MD – non-intercalated	HM (XRD)‡	HM (MD modeled at N/C ratio 0.375)	HM in DMF (XRD)‡
Initial material*	19.5±0.1	19.85±0.01	25.48±0.02	25.31±0.04	26.8±0.1
After drying @ 120 °C	19.5±0.1	**N/A**	20.6±0.3	**N/A**	26.0± 0.2
Vacuum drying @ 200°C	19.3±0.2	**N/A**	**N/A**	**N/A**	20.1± 0.5

* Prior to intercalation, the $Ti_3C_2T_x$ powder was dried in a desiccator under vacuum (< 10 Torr) at RT for 24 h. ‡ Both HM and HM in DMF treatments were carried out at 80 °C for 24 h.

When the HM intercalated powders were heated to 120 °C in a vacuum oven, the *c*-LPs decreased from 25.48±0.02 Å to 20.6±0.3 Å, signifying that the intercalation process was essentially reversible. Heating powders intercalated with HM *and* DMF under the same conditions resulted in small increases in the 2θ angles (Figure 44A-ii and

B-ii). Thus, the HM/DMF combination was more resistant to de-intercalation than HM alone, possibly because of the higher boiling point of DMF (153 °C) compared with that of HM (114 °C). When the latter powder – $Ti_3C_2T_x$ intercalated with HM *and* DMF – was vacuum dried at 200 °C, however, the *c*-LP decreased to 20.1±0.5 Å.

XPS analysis (Figure 45) provided further evidence of intercalation. As previously reported [23], exfoliated $Ti_3C_2T_x$ showed the presence of Ti–C and Ti–O bonds, as well as OH groups suggested by the presence of an O1s peak around 530 eV. An N1s signal was also observed around 400 eV in the XPS spectra of $Ti_3C_2T_x$ treated with HM and HM/DMF (insets in Figure 45A and B, respectively). No nitrogen peaks were detected in $Ti_3C_2T_x$ prior to intercalation.

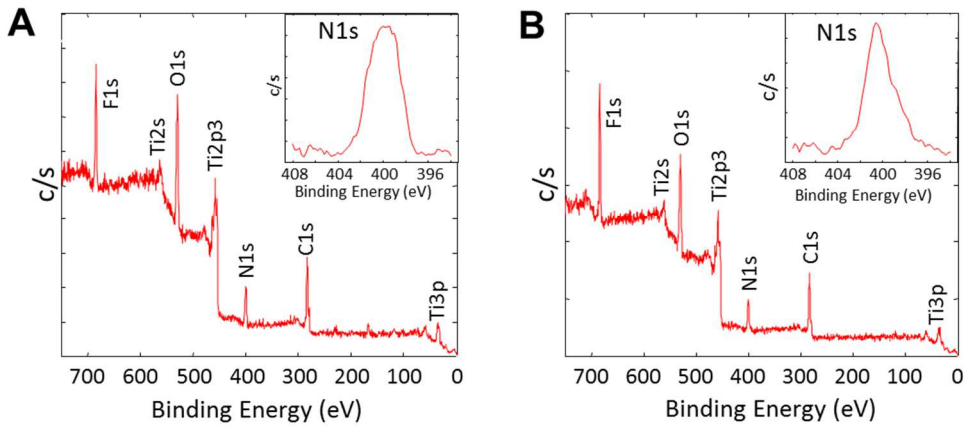

***Figure 45**. XPS spectra of $Ti_3C_2T_x$ intercalated with (**A**) hydrazine monohydrate at 80 °C for 24 h, and (**B**) hydrazine monohydrate and dimethylformamide at 80 °C for 24 h. Both insets showed N1s peaks for corresponding samples. [87]*

SEM images of $Ti_3C_2T_x$, before and after HM treatment in DMF at 80 °C for 24 h, shown in Figure 46A and B, respectively, confirmed that: i) the MXene remained

exfoliated after intercalation, and, ii) the layers thickened (Figure 46B) apparently by gluing monolayers together, forming 20-50 nm thick lamellas. Note that the absence of XRD peaks corresponding to a *c*-LP of 19.5 Å (Figure 44A-i and B-i) implied that intercalation was essentially complete.

TEM images and corresponding SAED patterns of $Ti_3C_2T_x$ intercalated with HM in DMF at 80 ºC for 24 h (Figure 46E and F) showed that the basal plane hexagonal structure remained unchanged (compare inset in Figure 46D with Figure 46F) after intercalation. The interplanar spacing in intercalated $Ti_3C_2T_x$ - 2.648 Å for $(0\bar{1}10)$ and 1.540 Å for $(1\bar{2}10)$ – resulted in an *a*-LP of 3.057 Å, in excellent agreement with the *a*-LP of $Ti_3C_2T_x$ before intercalation and that of the Ti_3AlC_2, *viz.* 3.058 Å [23].

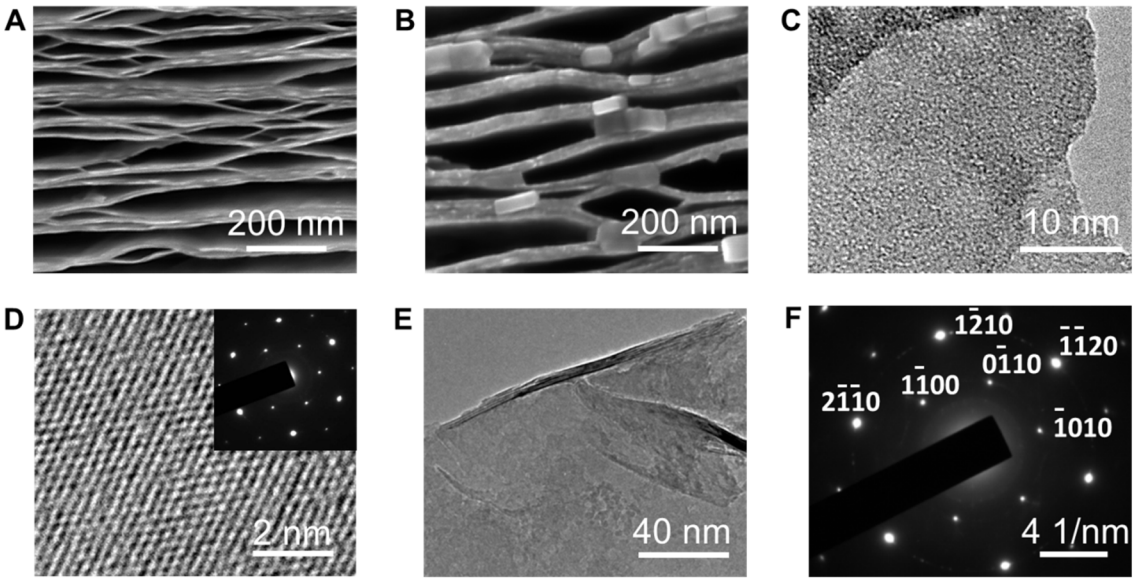

***Figure 46**. SEM images (**A**) before and (**B**) after intercalation of $Ti_3C_2T_x$ with hydrazine monohydrate and N,N-dimethylformamide (24 h at 80 °C), respectively. (**C**) TEM and (**D**) HR-TEM images (inset shows SAED pattern) before intercalation. (**E**) TEM image and (**F**) SAED pattern of intercalated $Ti_3C_2T_x$. [87]*

Interestingly, when hydrazine intercalated $Ti_3C_2T_x$ powder was treated with propylene carbonate (PC), it led to a further increase in the *c*-LP up to 27.0 Å (Figure 47). Considering that (i) secondary co-intercalation was not observed for other organic compounds (for example, ethanol) and (ii) PC cannot be intercalated in pristine $Ti_3C_2T_x$ alone (see Section 4.5.2.2), this suggested that some chemical interactions might be occurring between PC and the primary intercalant, *viz*. N_2H_4.

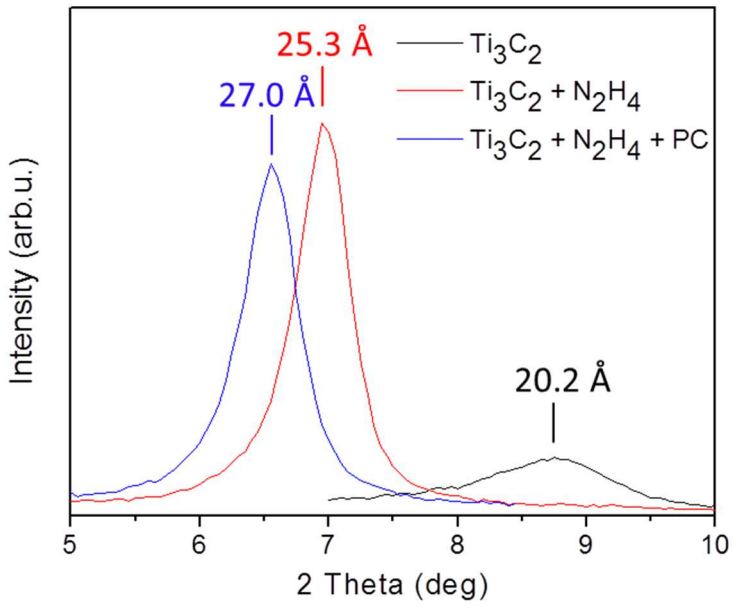

***Figure 47**. XRD patterns of pristine $Ti_3C_2T_x$ (black), hydrazine intercalated $Ti_3C_2T_x$ (red), and hydrazine intercalated $Ti_3C_2T_x$ co-intercalated with propylene carbonate (blue).*

It is possible that a typical reaction of cyclic carbonate with an amino group, known as aminolysis, occurred. In this way, PC reacted with NH_2 group of intercalated hydrazine opening a ring of the former and producing alcohols. The process can thus be described by the following reaction:

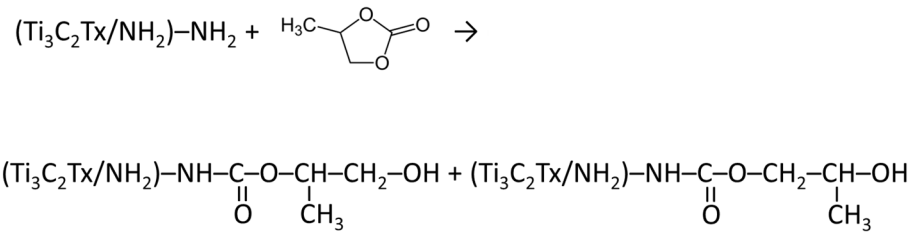

(10)

However, the proposed reaction has not yet been experimentally confirmed for MXene. The increase in *c*-LP value was the only evidence for now. However, it is reasonable to believe that such opening of the interlayer space would make it possible for larger organic molecules to be co- or post-intercalated, opening new avenues to carry out complex chemical reactions – such as catalysis, polymerization (similar to intercalated graphite) [121], etc. – inside the interlayer spaces.

4.5.2.1.2. Molecular dynamics simulations

The properties of intercalated compounds to a large extent are determined by the amount, arrangement and reactions of the guest molecules within the host material. In addition, the structure of the intercalant often provides a key to deciphering the intercalation mechanisms. This problem's complexity was illustrated by the large body of literature on the structure of HM intercalation in clays [112-120]. In the same spirit, it is reasonable to assume that the modeling of intercalated MXenes will likely constitute a large area of future research aimed at predicting the structure and properties of these new materials. The MD study of the intercalation of HM into MXene was thus run to compare models to experimental data.

To further understanding of the structure of intercalated MXene, MD simulations of N_2H_4 inserted between OH-terminated $Ti_3C_2T_x$ layers were carried out (Figure 48A). MXene supercells (4 x 2 x 1 (a x b x c)) with N_2H_4 uniformly spaced between the MXene

layers at different concentrations were constructed for MD studies (see Appendix A). With no N_2H_4 molecules, the MD computed *c*-LP values were reasonably close to the experimental result (Table 14) and DFT calculated values [23]. When two N_2H_4 molecules were introduced (one into each interlayer space), the *c*-LP jumped sharply to 24.93±0.01 Å (Figure 48A). A further increase of the number of N_2H_4 molecules results in only slightly changed *c*-LPs (from 24.93 to 25.31 Å), corresponding to a monolayer formation (Figure 48A) within the widened interlayer MXene space. With 6 N_2H_4 molecules per supercell (3 inside each interlayer space as shown in Figure 48B) the intercalant monolayer was complete and the introduction of the next pair of N_2H_4 molecules resulted in a second sharp increase of *c*-LP from 25.31±0.04 Å (6 N_2H_4

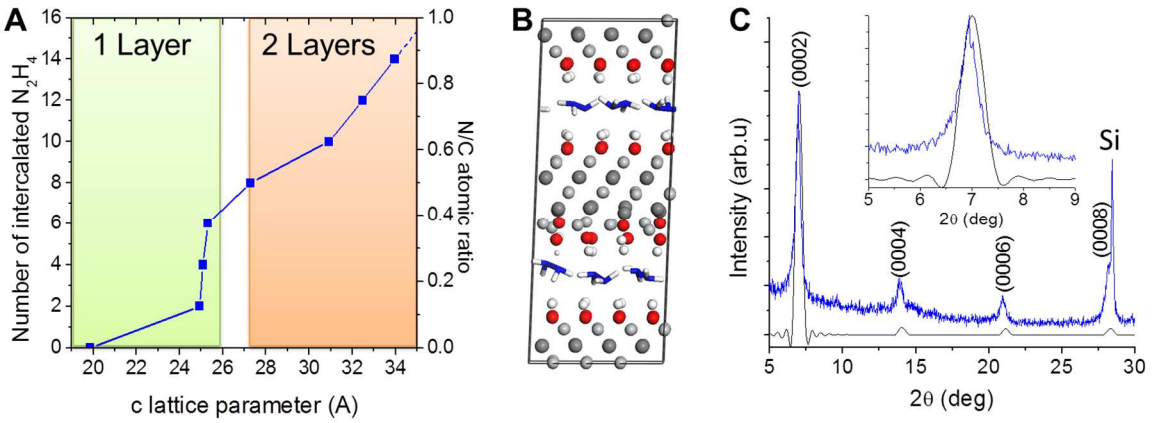

Figure 48. *Molecular dynamic simulations of OH-terminated Ti_3C_2 intercalated with hydrazine. (**A**) Change in $Ti_3C_2T_x$ c-lattice parameter as a function of the number of N_2H_4 intercalated molecules. As the latter was increased, first a monolayer of N_2H_4 molecules was formed, corresponding to the N/C ratio ~ 0.4 (c = 25-26 Å). Further increase in the number of N_2H_4 intercalated molecules results in the onset of the second layer formation, which was not complete up to the maximum N/C ratio employed in the simulations (N/C = 0.875). (**B**) Molecular dynamic snapshot of MXene for N/C ratio 0.375 (6 N_2H_4 per a 4x2x1 MXene supercell) showing a nearly complete N_2H_4 monolayer. For color coding of the elements see Figure 43. (**C**) Comparison of simulated (black) and experimental XRD patterns (blue).[87]*

molecules) to 27.28±0.03 Å (8 N_2H_4 molecules) as shown in Figure 48A, which was evidence for the onset of the formation of a second intercalant layer (see also MD snapshot in Figure 19A).

The experimental *c*-LP value for N_2H_4 intercalated MXene (c = 25.48 Å, Table 14) corresponded to an N/C ratio ~ 0.39 (Figure 48A), i.e., to the formation of a nearly complete monolayer of N_2H_4 molecules in each MXene interlayer space. The N/C ratio, determined by XPS for the HM intercalated MXene dried at RT, was 0.37, in very good agreement with the value deduced from the MD simulations (~0.4) for the situation with a nearly complete monolayer of N_2H_4 molecules (Figure 48B). Furthermore, the computed XRD pattern for the system of this composition is close to the one measured experimentally (Figure 48C).

4.5.2.1.3. Intercalation of other MXenes

To demonstrate that intercalation was a general phenomenon rather than the exclusive property of $Ti_3C_2T_x$, the MXenes Ti_3CNT_x and $TiNbCT_x$ were also treated with HM. Similar to $Ti_3C_2T_x$, the shift of the major XRD peak of these MXenes to lower 2θ values (Figure 49) confirmed their intercalation. It is important to note that one of those phases was a carbonitride with the same general formula as Ti_3C_2 (M_3X_2), whereas the other one represented a different kind of MXene with the formula M_2X (TiNbC) [24]. It is thus reasonable to conclude that multilayered MXenes – like other layered materials - can be readily intercalated by a host of compounds.

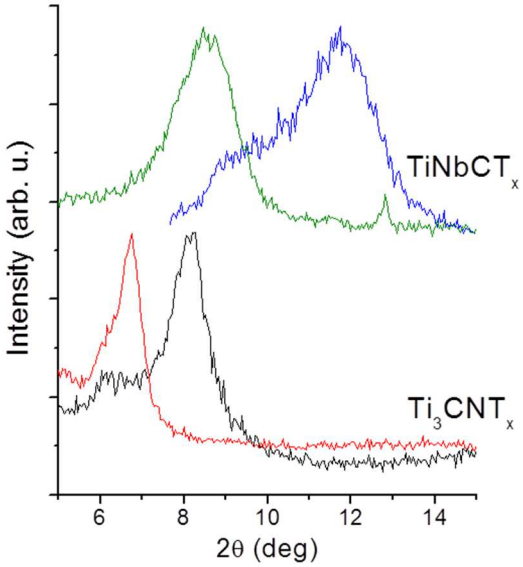

Figure 49. *XRD patterns of Ti_3CNT_x (at the bottom) before (black) and after (red) HM treatment and $TiNbCT_x$ (at the top) before (blue) and after (green) HM treatment. For all samples, initial MXene was dried in a desiccator under vacuum (< 10 Torr).[87]*

In addition, the electrical resistivities of non-intercalated MXenes and MXenes treated with HM were measured and showed to be higher for all intercalated samples compared to those that were not intercalated. As expected, the resistivity values of all intercalated samples were higher than those of non-intercalated MXenes due to the increase of their *c*-LPs after intercalation (Table 15). The difference in the magnitude of the resistivity increase for different intercalated MXenes at relatively the same expansion can be partially explained by the different number of MXene atomic layers. In case of M_3X_2 (5 atomic layers), the resistivity increased by an order of magnitude, whereas an increase by two orders was observed for M_2C (3 atomic layers) compounds.

***Table 15**. Sheet resistivity, resistivity and density of cold-pressed discs for different non-intercalated MXenes and MXenes treated with hydrazine monohydrate (HM).[87]*

MXene	Sheet Resistivity, Ω/□		Resistivity, Ωm		Density, g/cm^3	
	Non-intercalated	HM treated	Non-intercalated	HM treated	Non-intercalated	HM treated
$Ti_3C_2T_x$	61	243	0.016	0.056	2.58	2.71
Ti_3CNT_x	43	711	0.011	0.249	3.22	2.90
Nb_2CT_x	321	12806	0.139	4.977	3.75	3.47
$TiNbCT_x$	230	44661	0.092	17.471	3.67	3.01

4.5.2.2. Intercalation of Organic Molecules

Encouraged by the results of MXene intercalation with HM, a number of organic compounds were tested as potential intercalants using the same intercalation procedure (Table 16). Based on the XRD patterns it was confirmed that only four of them, DMSO, i-PrA, urea, and ACN, could be intercalated into $Ti_3C_2T_x$ resulting in increase of *c*-LP up to 35.03, 27.8, 24.8, and 21.5 Å, respectively. This observation suggested that intercalation was strongly dependent on the properties of the organic compound, and generally a large dipole moment and small size favored the process, as reported for clays [119, 122]. Thus, the dipole moments of $Ti_3C_2T_x$ intercalants – DMSO, urea, and ACN – were all above 3.9D. In contrast, other highly polar compounds such as PC and n-methyl-2-pyrolidone (see Table 16 for comparison) do not directly intercalate $Ti_3C_2T_x$, most likely due to steric limitations.

Table 16. *Changes in c-lattice parameters (c-LPs) after intercalation of $Ti_3C_2T_x$ with hydrazine and organic compounds. Value of Δ (third column) indicates the increase of the c-LP of $Ti_3C_2T_x$ after intercalation compared to initial c-LP of 20.3 Å.*

Organic compound (abbreviation, if any)	Chemical formula	*Δ (c*-LP*), Å*	*Dipole moment, D*
Dimethylsulfoxide (DMSO)	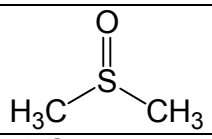	15.9	3.96
Isopropyl amine (i-PrA)	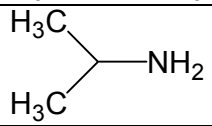	7.6	1.19
Hydrazine	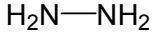	5.9	1.79
Urea	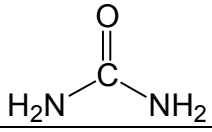	5.0	4.56
Acetonitrile (ACN)	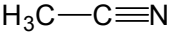	2.3	3.92
Acetone	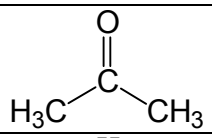	–	2.70
Chloroform	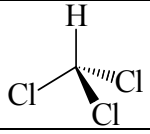	–	1.04
Ethanol	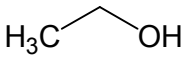	–	1.30
Formaldehyde	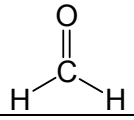	–	2.33
Hexane	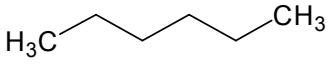	–	0.08
Dimethylformamide (DMF)	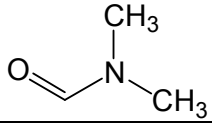	–	3.82
Propylene carbonate (PC)	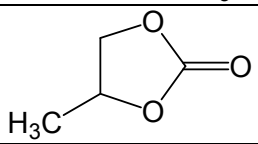	–	4.94
Tetrahydrofuran (THF)	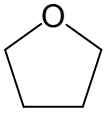	–	1.63

Thiophene	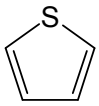	–	0.55
Toluene	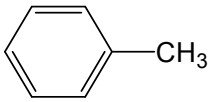	–	0.36
n-Methyl-2-pyrolidone	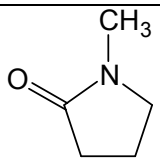	–	4.10

Note: All dipole moments are shown for pure compounds.

However, not all small intercalants followed the high dipole moment principle. Those include i-PrA and hydrazine. In both cases, intercalation occurred from their aqueous solutions (i-PrA- and hydrazine-water ratio were 1:4 and 1:1, respectively) instead from pure liquids for whose dipole moments are shown in Table 16. Both compounds possessed basic behavior and got protonated when mixed with water following the reactions (11) and (12):

$$H_2N–NH_2 + H_2O \leftrightarrow H_2N–NH_3^+ + OH^- \quad (11)$$

$$(CH_3)_2CH–NH_2 + H_2O \leftrightarrow (CH_3)_2CH–NH_3^+ + OH^-. \quad (12)$$

Considering the negative charge at the $Ti_3C_2T_x$ surface, positively charged species formed at equilibrium could potentially intercalate between $Ti_3C_2T_x$ layers with the assistance of electrostatic forces.

It is important to note that compounds which can enter the $Ti_3C_2T_x$ structure do not necessarily intercalate into other MXenes (see Appendix F) which may be explained by differences in their surface chemistries and structures and, consequently, properties – surface charge, elasticity, *etc*. – crucial for successful intercalation.

4.5.3. Delamination

After the discovery of the ability of $Ti_3C_2T_x$ to intercalate a variety of positively charge ions and small molecules, potential routes of its large-scale delamination were explored.

4.5.3.1. Dimethyl Sulfoxide

4.5.3.1.1. Delamination in aqueous solvent

XRD patterns, taken 3 weeks after the initial DMSO intercalation (Figure 50, red curve), showed an even larger downshift of the (0002) peak positions corresponding to a *c*-LP of 44.8±0.1 Å. Based upon this result, combined with the observation that DMSO intercalated MXene powders were highly hygroscopic and become increasingly wet when stored in air over a few weeks, it was reasonable to assume that, over time, co-intercalation or capillary condensation of water from ambient air into the interlayer space, occurred.

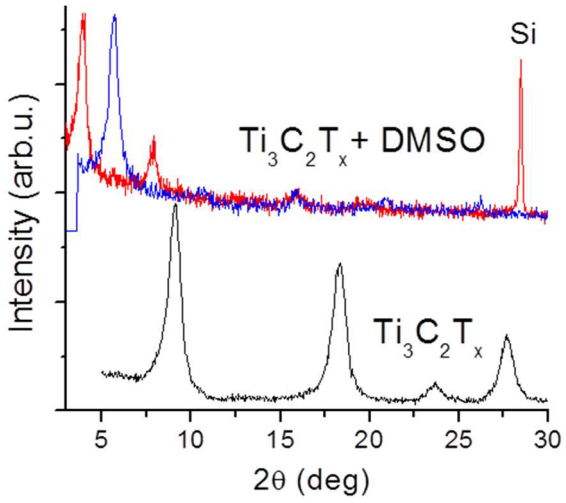

Figure 50. *Intercalation of $Ti_3C_2T_x$ with dimethyl sulfoxide. XRD patterns of $Ti_3C_2T_x$: i) before any treatment, ii) after dimethyl sulfoxide treatment for 30 min (blue) and 3 weeks (red) after drying in a desiccator at room temperature.[87]*

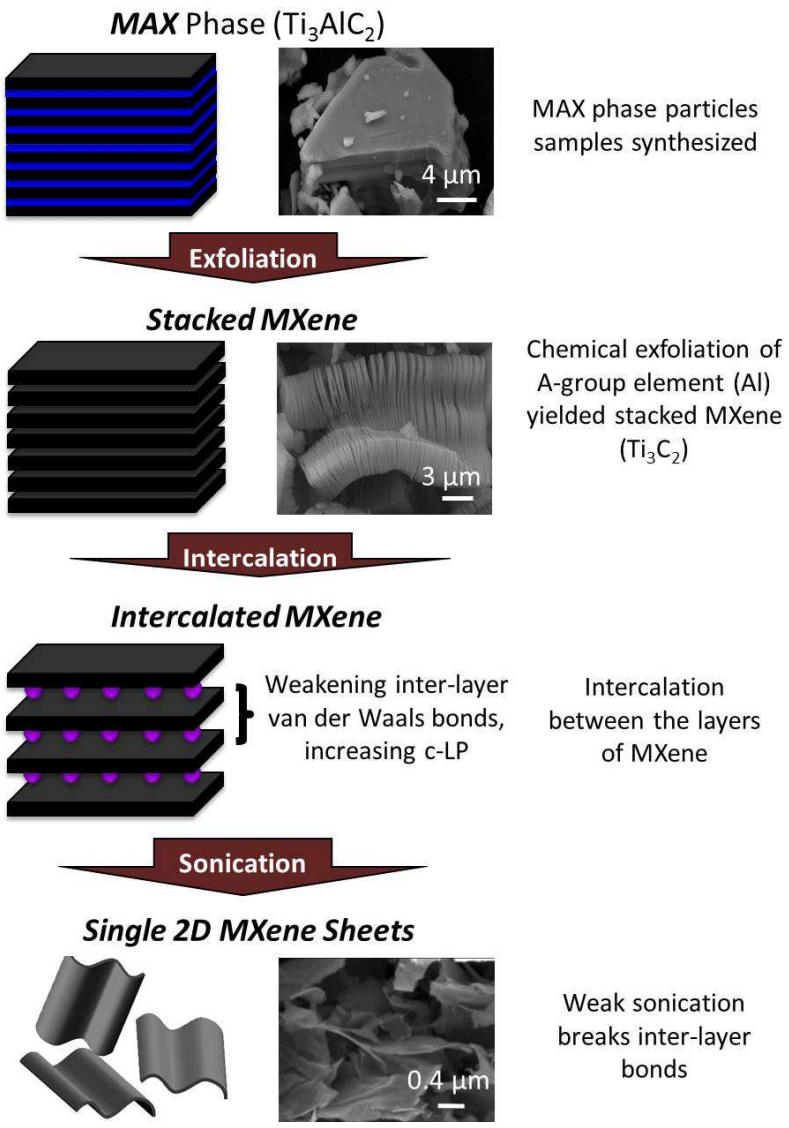

Figure 51. *Schematic of delamination of MXene flakes. [87]*

This discovery, in turn, was exploited to fully delaminate $Ti_3C_2T_x$ sheets (see Figure 51 for schematic). After a sonication of DMSO intercalated multilayered MXene dispersed in deionized water, fully delaminated – hereafter referred to as *d*-$Ti_3C_2T_x$ – flakes were obtained. After removal of coarse particles by centrifuging, the resulting aqueous colloidal solutions of *d*-$Ti_3C_2T_x$ flakes were stable. The majority of flakes were small, with a relatively narrow size distribution (Figure 52A). The colloidal state of the

delaminated MXene flakes in aqueous solutions was also confirmed by the observation of the Tyndall scattering effect when passing a red laser beam through the solution (inset Figure 52A). SEM images clearly showed thin, electron-beam transparent, single MXene flakes precipitated from a drop of colloidal solution placed on a porous alumina membrane surface (Figure 52B). Analysis of an AFM image (Figure 52C) showed that the thickness of delaminated flakes was ~1.0 nm (see profile in Figure 52D) confirming delamination into monolayer sheets.

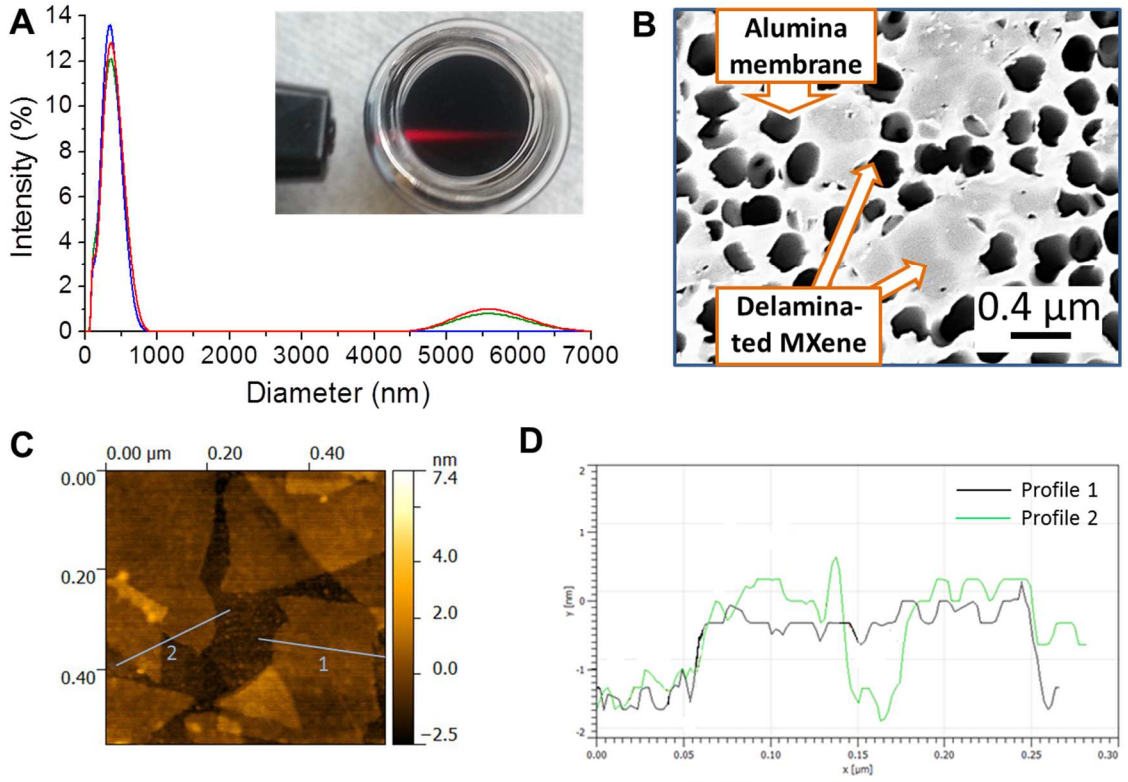

***Figure 52**. Delaminated $Ti_3C_2T_x$. **(A)** Particle size distribution in aqueous colloidal solution; Inset shows Tyndall scattering effect in the solution. **(B)** SEM images of d-$Ti_3C_2T_x$ flakes on the alumina membrane. **(C)** AFM image of d-$Ti_3C_2T_x$ flakes. **(D)** Height profile along the lines 1 and 2 shown in (C). [87]*

Binder-free *d*-$Ti_3C_2T_x$ "paper" (Figure 53A) was produced by filtering the aforementioned colloidal solution through an alumina membrane. XRD patterns of the resulting "paper" (Figure 53B) clearly showed that the non-basal peaks at $2\theta \approx 61°$ vanished after delamination. This result provided compelling evidence for the loss of order along all but the (0001) direction and consequently, full delamination.

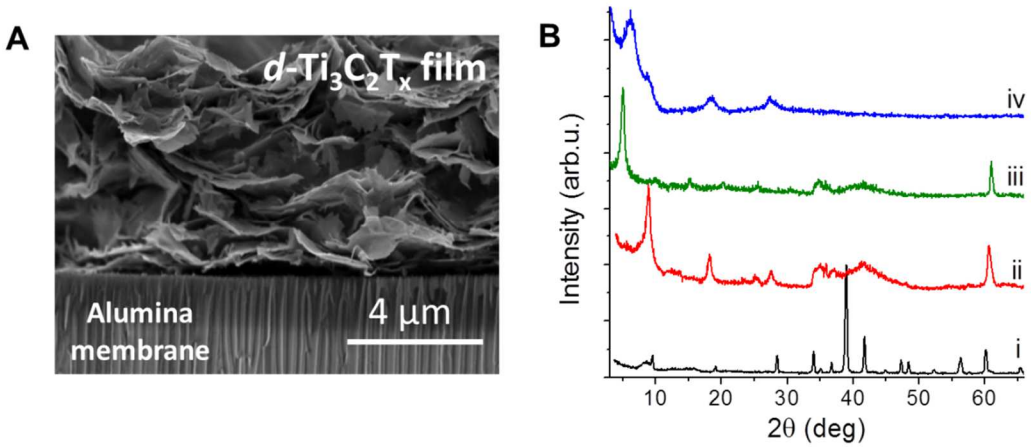

***Figure 53**. (**A**) SEM image of an additive-free film of d-$Ti_3C_2T_x$ filtered through an alumina membrane. (**B**) XRD patterns of, (i) Ti_3AlC_2, (ii) exfoliated $Ti_3C_2T_x$, (iii) dimethyl sulfoxide intercalated $Ti_3C_2T_x$ and (iv) delaminated d-$Ti_3C_2T_x$. Note the disappearance of the peak at 60° in (iv). [87]*

The *d*-$Ti_3C_2T_x$ papers produced by this technique appeared to be very flexible, conductive and hydrophilic [89, 123]. This combination of properties renders it a good candidate for electrodes for energy storage devices – better than its multilayer counterpart due to the much higher accessible surface area. Thus, the SSA of the *d*-$Ti_3C_2T_x$ paper measured using N_2 was 98 $m^2.g^{-1}$, which is significantly higher than SSA before delamination (23 $m^2 \cdot g^{-1}$). It is worth noting that the SSA of the paper was even higher

when CO_2 and Ar (128 and 167 $m^2 \cdot g^{-1}$ respectively) were used that when N_2 was used which can be explained by the presence of small pores.

It was not too surprising when it was later shown that *d*-$Ti_3C_2T_x$ paper electrodes possessed excellent Li-ion capacity of Li-ion batteries at quite high charging rates – 410 $mAhg^{-1}$ at a 1 C cycling rate, which was 5 times higher than as-etched $Ti_3C_2T_x$, and 110 $mAh.g^{-1}$ at 36 C after 700 cycles – which cannot be achieved for commercial graphite electrodes [87]. It was further shown that using $Ti_3C_2T_x$ paper as an electrode in supercapacitors resulted in quite high volumetric capacitances when tested in aqueous electrolytes offering capacitance in excess of 300 F/cm^3 – which was much higher than commercial supercapacitors (about 60 F/cm^3) and the best published carbon electrodes (up to 200 F/cm^3) [89].

4.5.3.1.2. Delamination in organic solvent

Other solvents were investigated as a media to produce delaminated flakes. The goal was to eliminate the presence of water in *d*-$Ti_3C_2T_x$ paper which would be beneficial in some applications, such as Li-ion batteries. The following organic solvents (listed in alphabetical order) were tried: acetone, ACN, chloroform, DMF, formaldehyde, methanol, PC, and THF. After a 4-hour sonication of DMSO intercalated $Ti_3C_2T_x$ in each of these solvents separately, a droplet of each solution was placed on an alumina membrane and analyzed in a SEM (Figure 54). Looking for the samples with the highest amount of residue-free delaminated flakes, it was concluded that ACN, DMF and PC were the most promising. Sonication in other solvents led to complete decomposition

(acetone), partial decomposition and oxidation (THF, chloroform) or minimum flakes formation (formaldehyde).

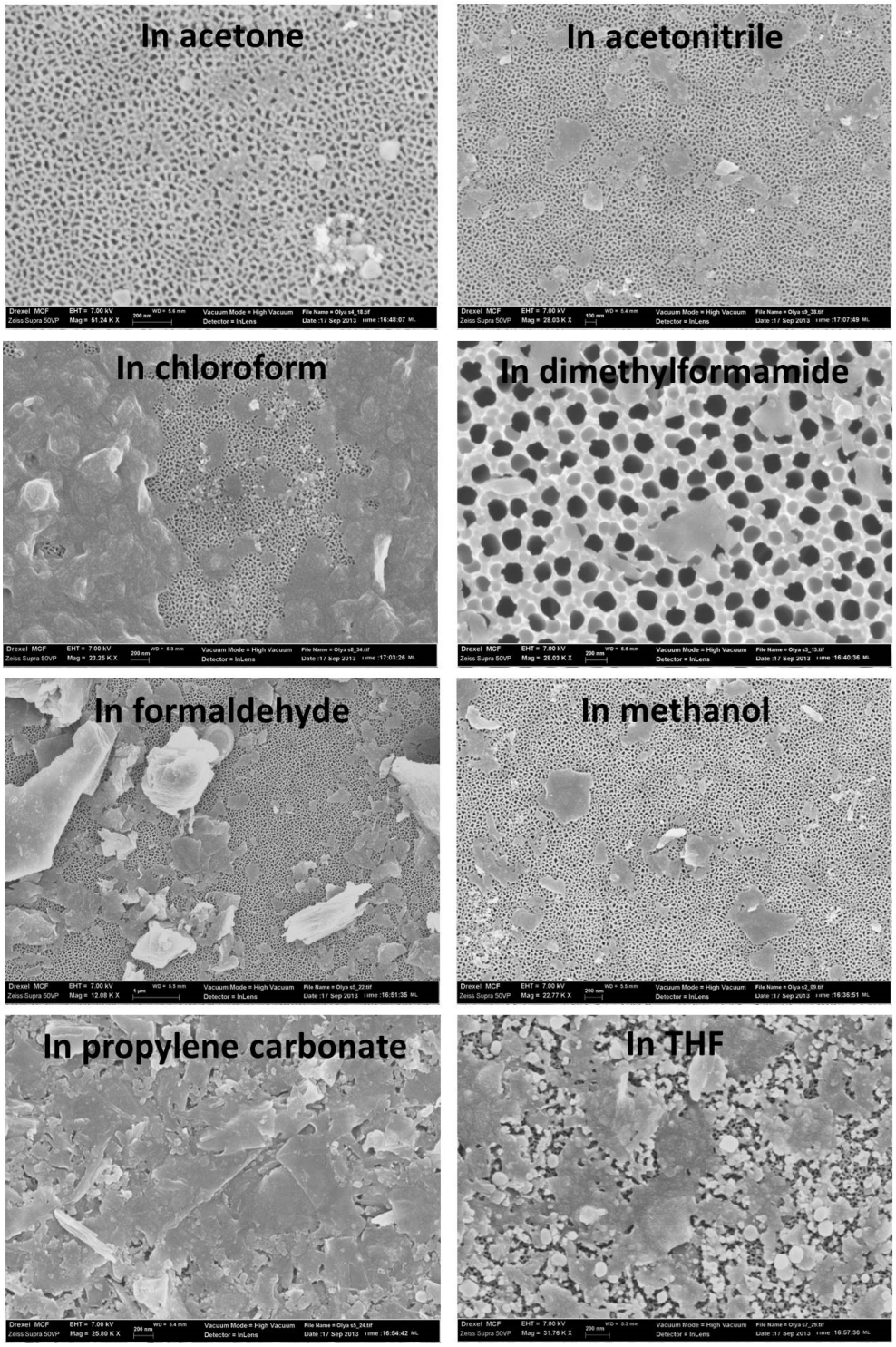

Figure 54. *SEM images of dimethyl sulfoxide intercalated $Ti_3C_2T_x$ sonicated in different solvents (acetone, acetonitrile, chloroform, dimethyl formamide, formaldehyde, methanol, propylene carbonate, and tetrahydrofuran) for 4 h.*

PC was thus chosen for further delamination work and found to be a good media to produce large quantities of 2D $Ti_3C_2T_x$ flakes upon sonication of DMSO intercalated multilayered MXene for 4 h and longer. Interestingly, the yield of delaminated flakes appeared to be dependent on sonication time. This dependence was observed when equal amounts of DMSO intercalated $Ti_3C_2T_x$ powder (1 g of each) were sonicated in 300 ml of PC at RT for 4 and 12 h separately, and then centrifuged for 1.5 h at 3500 rpm. The supernatant solution of the flakes sonicated for 12 h produced much thicker paper (Figure 55C and D) and, consequently, appeared to be more concentrated than that sonicated for 4 h (Figure 55A and B). It may be due to braking the large flakes into smaller pieces which are lighter and do not precipitate that easily during centrifuging. These preliminary results suggest that more work is needed to optimize the delamination conditions using organic solvents.

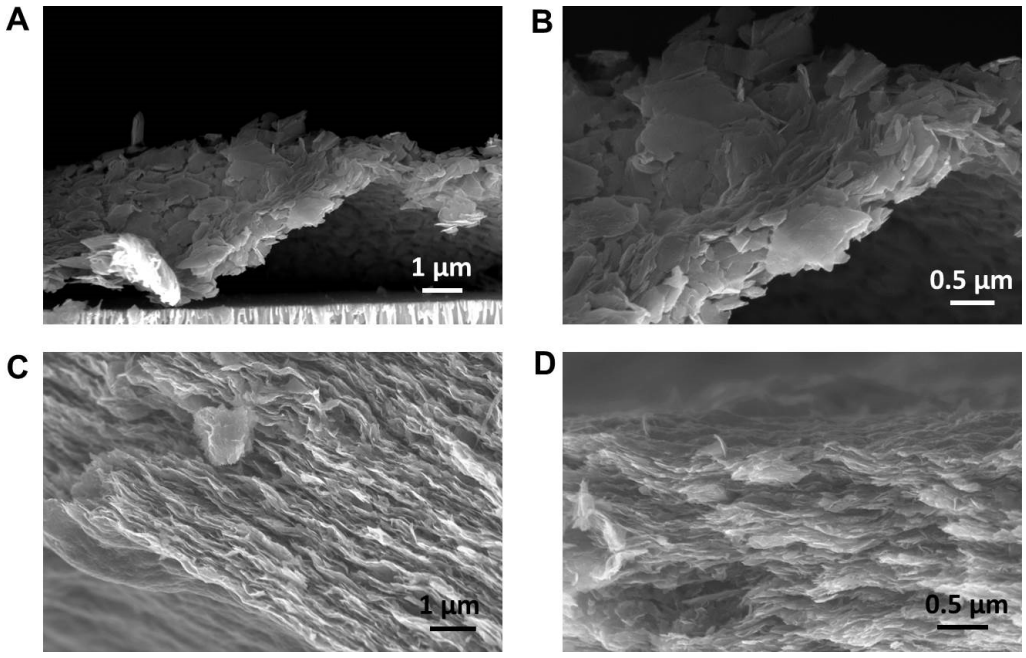

***Figure 55**. SEM images of additive-free films of d-$Ti_3C_2T_x$ produced by sonication of DMSO intercalated $Ti_3C_2T_x$ in PC for (**A** and **B**) 4 h and (**C** and **D**) 12 h followed by centrifuging and filtration through a membrane.*

4.5.3.2. Isopropyl Amine

Other intercalants have also been considered for MXene delamination. Considering its negative surface charge, $Ti_3C_2T_x$ was expected to have acidic behavior and interact with bases and positively charged species. As a result, isopropylamine (i-PrA) was chosen for the following reasons: i) it forms an ammonium cation $R\text{-}NH_3^+$ when mixed with water, and, thus, could potentially intercalate between the Nb_2CT_x layers with the assistance of electrostatic forces; ii) the i-PrA molecule has a 3-carbon-atom alkyl tail that is presumably small enough to overcome the steric hindrance upon intercalation and, simultaneously, large enough to push the MXene layers apart leading to weakened interlayer interactions and, consequently, successful delamination.

XRD patterns of $Ti_3C_2T_x$ before and after exposure to i-PrA (Figure 56A) resulted in a shift of the most intense (0002) $Ti_3C_2T_x$ peak toward lower 2θ angles corresponding to the increase in *c*-LP from an initial value of 19.9 Å before amine treatment to 27.5 Å after treatment. The interlayer distance thus increased by ≈ 7.6 Å, which was large enough to accommodate one layer of i-PrA and/or water molecules between the Nb_2CT_x layers.

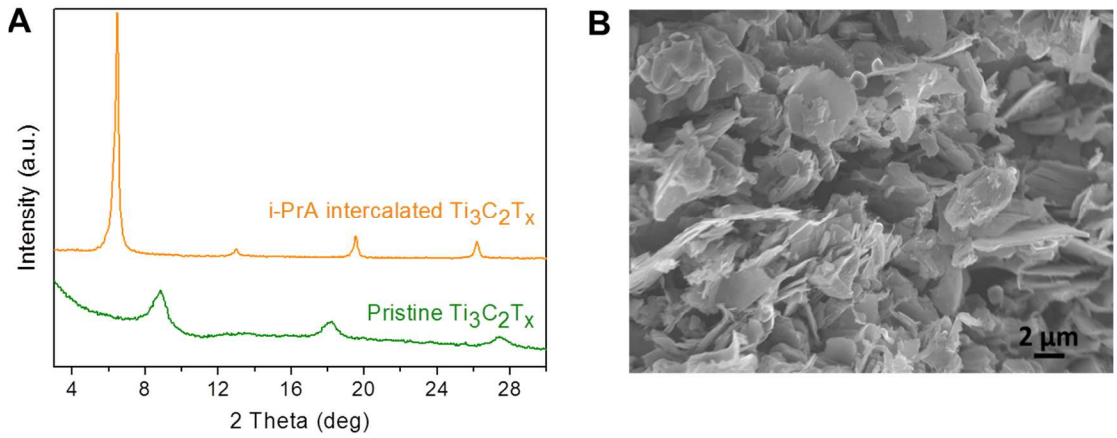

***Figure 56**. (**A**) XRD patterns of pristine (bottom) and isopropylamine intercalated $Ti_3C_2T_x$. (**B**) SEM image of partially delaminated $Ti_3C_2T_x$ powder produced by stirring of initial $Ti_3C_2T_x$ in isopropylamine aqueous solution for 18 h at room temperature (RT), then washed with ethanol and dried at RT in a desiccator. No sonication to enhance delamination or centrifuging to separate larger particles was required.*

The SEM image (Figure 56B) clearly showed that a few layer stacks of $Ti_3C_2T_x$ were delaminated upon i-PrA intercalation even before sonication suggesting improved delamination rate and single layer yield with further sonication.

It is important to note that another MXene, *viz*. Nb_2CT_x, was intercalated (see XRD patterns in Figure 57A) and then delaminated using the i-PrA-based approach. The Nb_2CT_x is the second MXene, separated into single flakes, after $Ti_3C_2T_x$. Its delamination was achieved by mild sonication of the i-PrA intercalated Nb_2CT_x multilayers in DI water. After removal of the larger particles by centrifugation, a stable black-colored colloidal solution of delaminated Nb_2CT_x flakes was obtained. Its colloidal nature was confirmed by the Tyndall effect [124], in which, as a result of light scattering, a green light beam was clearly seen when a laser was shone through it (see photo on the right in Figure 57B).

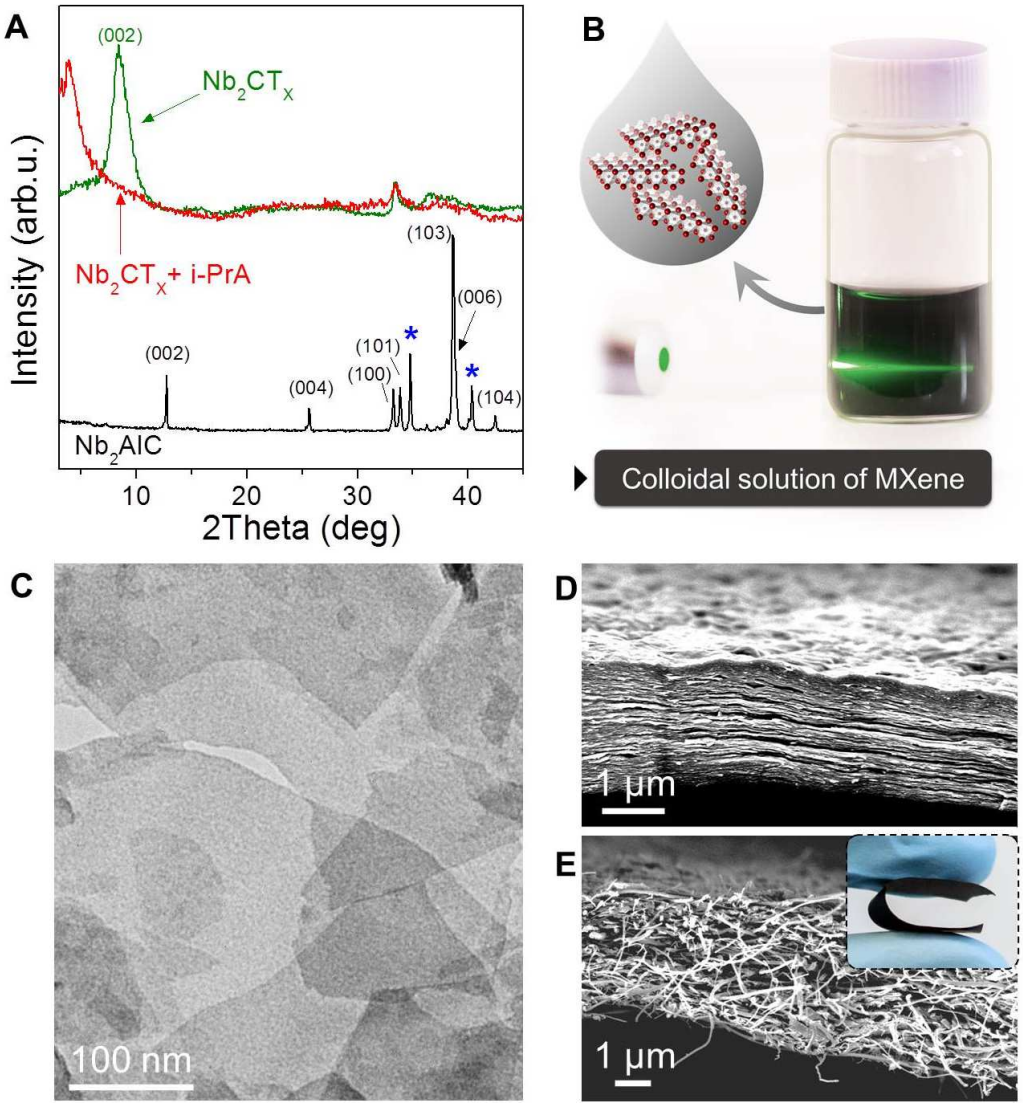

***Figure 57**. (**A**) XRD patterns of initial Nb_2AlC MAX phase (bottom), exfoliated and isopropylamine intercalated Nb_2CT_x (top). (**B**) The photo of Tyndall scattering effect in the colloidal solution of d-Nb_2CT_x flakes (**C**) TEM image of the d-Nb_2CT_x flakes. (**D, E**) Cross-sectional SEM images of pure Nb_2CT_x (D) and Nb_2CT_x/CNT composite paper (E).[125]*

When a drop of the colloidal solution was placed on a lacey carbon TEM copper grid and allowed to dry, electron transparent sheets of different sizes – from tens of nanometers up to few microns (Figure 57C) – were imaged. Their transparency suggested that the sheets were a few layers thick at most. Importantly, similar to delaminated

$Ti_3C_2T_x$, the colloidal Nb_2CT_x solution could be filtered to create free-standing and flexible paper (Figure 57D). The restacking of the MXene flakes was observed when solution was filtered alone. This effect could be eliminated by using 10 wt.%. multiwall carbon nanotubes (CNTs) containing Nb_2CT_x flakes solution. Such CNT/$Ti_3C_2T_x$ film (Figure 57E) showed excellent cyclability and Li capacities of more than 400 mAh/g at 0.5 A/g, significantly improved compared to multilayered (*i.e.*, non-delaminated) material, when tested as an anode material in Li-ion battery, and high volumetric capacitance of 325 F/cm^3 when tested in a Li-ion capacitor configuration.

Beyond $Ti_3C_2T_x$ and Nb_2CT_x, i-PrA appeared to be a universal intercalant for other MXenes. Thus, i-PrA intercalated $Nb_4C_3T_x$ – the first M_4C_3 MXene that has been intercalated with small organic molecules. For this, longer treatments (up to 2 weeks) were required to fully expand the structure (Figure 58). This was important because it implied that the thickness – or stiffness – of the MXene layers is not a limiting factor in the delamination process. It also suggested that other MXenes, which could not be produced as single layers so far, could be delaminated using this technique if the proper amine and delamination conditions (concentration, intercalation time, intensity of sonication, etc.) are determined.

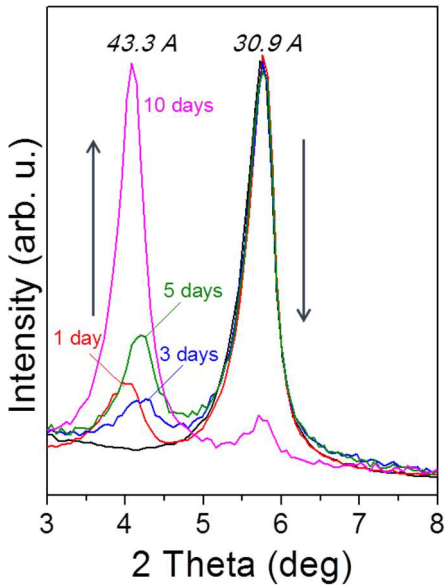

Figure 58. Time dependence of intercalation of isopropylamine into $Nb_4C_3T_x$. With time in the isopropylamine, the initial (0002) (c-LP = 30.9 Å) Nb_2CT_x peak intensity decreased at the expense of a peak at a lower 2Θ angle (c-LP = 43.3 Å) as a result of intercalation.[125]

4.6. Chemical Modification of $Ti_3C_2T_x$

4.6.1. Vacuum Annealing

Vacuum annealing at elevated temperatures was carried out in order to try to reduce the oxygen concentration by removing physisorbed molecules (presumably water) and/or OH surface groups. To do so, $Ti_3C_2T_x$ powder previously dried at 100 °C for 22 h was heated in vacuum (~10^{-6} torr) up to 200 °C and held at this temperature for 24 h. This procedure resulted in a 15.56 wt.% of weight loss. After annealing, *c*-LP of the sample decreased to 19.315 Å compared to 19.622 Å before heating in vacuum; that indicated only a 2% decrease in the *c*-LP after heating in vacuum. EDX results varied depending on the spot where the pattern was taken. In case of focusing on the (100) plane of the

exfoliated particles (spot size ~ 5 μm in diameter), the Ti:C:O:F:Al atomic ratios were around 35:20:20:23:1 and 40:22:10:25:1 for the sample before and after vacuum heating, respectively (Table 17). Taking into account that the XRD pattern showed no peak around 2θ = 39° which would indicate the presence of non-exfoliated Ti_3AlC_2, it was reasonable to suppose that the Al signal appeared due to the presence of AlF_3 crystals which were not removed during filtration. Considering the presence of AlF_3, the Ti:C:O:F atomic ratios of elements were around 35:20:20:20 and 40:22:10:22 for the sample before and after vacuum heating, respectively. It is consistent with the structures written as ≈ $Ti_{3.5}C_2F_2(OH)_2$ and $Ti_{3.6}C_2F_2(OH)_{0.9}$, respectively. However, EDX spectrum taken by focusing on a large spot (~50 μm in diameter), showed that the Ti:C:O:F atomic ratios were around 37:17:21:20 and 31:14:18:21 for the sample before and after vacuum heating (Table 17) which corresponded to $Ti_3C_{1.4}F_{1.6}(OH)_{1.7}$ and $Ti_3C_{1.4}F_{1.7}(OH)_2$, respectively. These numbers indicated a slight increase in oxygen content in the vacuum treated sample, implying that vacuum annealing at 200 °C was not a good way to reduce the $Ti_3C_2T_x$ surface.

Table 17*. EDX analysis of $Ti_3C_2T_x$ powder performed before and after vacuum annealing at 200 °C focused on single particles and on a larger area ~50 μm in diameter.*

Element	Atomic %			
	Before vacuum (single particle)	After vacuum (single particle)	Average before (~ 50 μm spot)	Average after (~ 50 μm spot)
C K	19.85	22.17	17.02	14.16
O K	19.8	10.05	21.27	18.29
F K	23.6	25.73	23.54	32.64
Al K	1.64	1.66	1.08	3.55
Ti K	35.11	40.39	37.1	31.36

4.6.2. Annealing in Different Gaseous Atmospheres

4.6.2.1. N_2

To explore the changes in MXene chemistry in different atmospheres, TGA was carried out. Two samples were heated in N_2 gas for comparison. Figure 59A shows the weight losses of exfoliated powders that were previously dried in air at RT for 72 h. Figure 59B shows the same for powders held under mechanical vacuum at 120 °C for 24 h. The total weight loss for the former was 7.4 % with respect to the original sample weight; for the latter it was 4.5 %. In both cases, the weight loss between 40 and 200 °C could be attributed to the removal of superficial and interstitial water and/or HF residue from the MXene surfaces [126, 127]. Weight losses above 200 °C could result from the dehydroxylation of the remaining isolated OH groups bonded to the Ti-terminated surfaces [128]. It could be also attributed to the elimination of physisorbed water embedded between the layers [126]. In both cases, weight losses in this range were roughly the same (around 2.6 wt.%). This result was not too surprising since both samples were dried at temperatures below 200 °C. At temperatures $>$ 450 °C, no significant weight change was observed in the TGA curves (only ~ 0.4 wt.%), which demonstrated that most volatile species were eliminated at temperatures below this threshold.

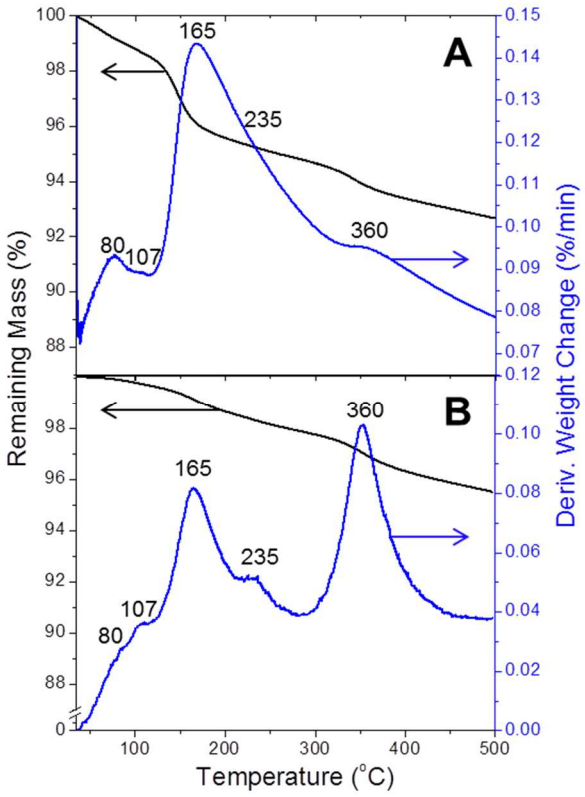

***Figure 59**. TG curves (left axis, black curves) of HF-treated Ti_3AlC_2 powder held, (**A**) in air at RT for 72 h prior to DTA, (**B**) under mechanical vacuum at 120 °C for 24 h prior to TGA. Derivative weight loss curves (right axis, blue curves) identify the temperatures where weight losses were most apparent.[75]*

Comparing the weight losses of samples dried at RT and at 120 °C, in the 30-120 °C temperature range (Figure 59A and B), one can estimate the amount of gas product produced as a result of drying under mechanical vacuum at 120 °C for 24 h. Assuming evaporation of water alone (no HF release), calculations showed evaporating of ~ 0.0007 mole of water per 1 g of exfoliated $Ti_3C_2T_x$ due to drying. This amount of water represented ~16.7 wt.% of the overall weight loss taking place between 40 and 500 °C.

As noted above, the weight loss in the 200-500 °C temperature range that could be attributed to the dehydroxylation of the OH groups was ≈ 2.6 %, viz. ≈ 1/6 of what it

should have been had the initial composition been $Ti_3C_2(OH)_2$. Why this was the case was not entirely clear, but was most probably due to the presence of fluorine termination. EDX of exfoliated samples dried at RT showed that the Ti:C:O:F atomic ratios were 35:25:15:25. In other words, the exfoliated structure could be written as ≈ $Ti_{2.94}C_2F_2O_{0.55}(OH)_{0.65}$. (Note that if the formal valences of the elements are chosen to be: Ti = + 4, C = - 4, etc. – $Ti_{2.94}C_2F_2O_{0.55}(OH)_{0.65}$ is electrically neutral. In other words, the formula assumed would be electrically neutral and was more consistent with the weight loss and EDX results.) Assuming the complete removal of OH surface groups due to treatment at 450 °C, the theoretical weight loss of this composition should be 4.9 %, a value much closer to the experimentally measured 2.6 wt.%. It follows that the less than expected weight loss could be ascribed to the presence of F. Another possibility was the oxidation of the MXene composition to form TiO_2 (rutile), a phase that is known to form if MXene samples are heated to 600 °C in air. Another possibility was the partial substitution of carbon by oxygen in the $Ti_3C_2T_x$ structure, as happens in cubic TiC [129].

4.6.2.2. NH_3

NH_3 annealing at different temperatures was performed to modify the $Ti_3C_2T_x$ structure. XRD analysis of the samples treated in the range from RT up to 450 ˚C showed that intercalation occurred at low temperatures while the formation of TiO_2 was more common at higher temperatures. Thus, Figure 60A shows that (0002) XRD $Ti_3C_2T_x$ peak shifted to lower 2θ angles, implying the *c*-LP increased by up to 25.0 Å upon treatment at RT or 55 ˚C. Interestingly, this shift of 5.4 Å was the same as was reported for $Ti_3C_2T_x$ intercalated in NH_4OH aqueous solutions (Table 11). When the powder was treated with

gaseous NH_3 at 150 ˚C and higher, no shift of the (0002) peaks was observed (Figure 60B) most likely due to deintercalation of gas molecules occurring at those temperatures. Instead, a small peak assigned to anatase appeared at 2θ ≈ 26˚ at 300 ˚C and became pronounced at 450 ˚C. At the same time, MXene still kept its layered structure, evidenced by strong (000*l*) peaks at 2θ = 9.0˚, 18.4˚, 28.0˚, and 37.5˚, corresponding to (0002), (0004), (0006) and (0008) peaks.

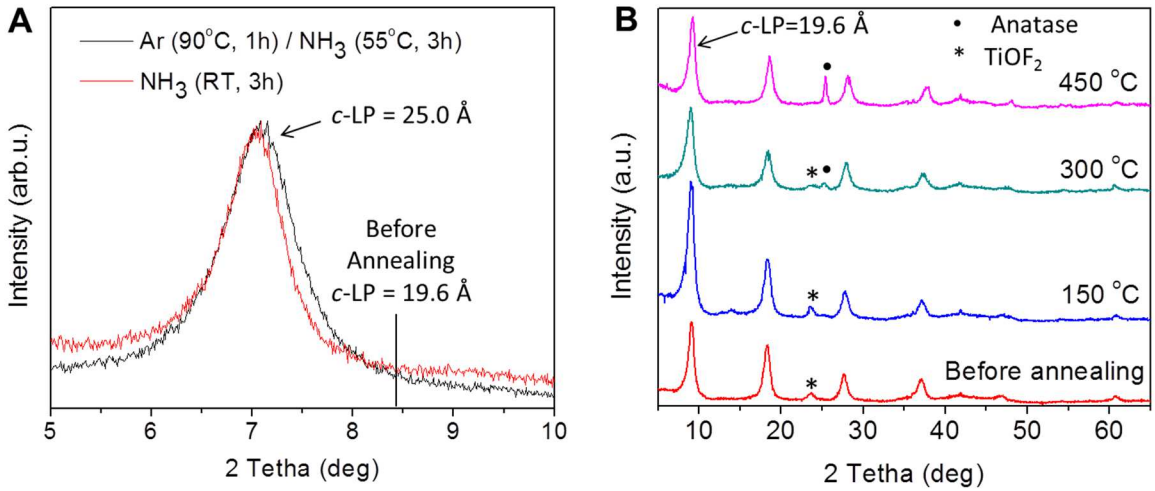

Figure 60. *XRD patterns of NH_3 treated $Ti_3C_2T_x$ powders annealed at (**A**) low (room temperature and 55 ˚C) and (**B**) high (150, 300 and 250 ˚C) temperatures.*

4.6.3. Oxidation

4.6.3.1. Spontaneous Oxidation

When $Ti_3C_2T_x$ was stored in aqueous solutions for prolonged periods of time, it slowly oxidized into TiO_2. This can be easily detected visually by comparing a fresh solution of $Ti_3C_2T_x$ flakes with one stored in air for 2 weeks (Figure 61A). The latter turned white, indicating oxidation. To determine whether the water or oxygen caused the

oxidation, *d*-$Ti_3C_2T_x$ flakes were stored in aerated and de-aerated (by boiling and then bubbling Ar through the water) water. As shown in Figure 61B, the former turned white after about 72 h exposure while the latter remained black for longer times. This result implied that oxygen was one of the factors causing MXene oxidation.

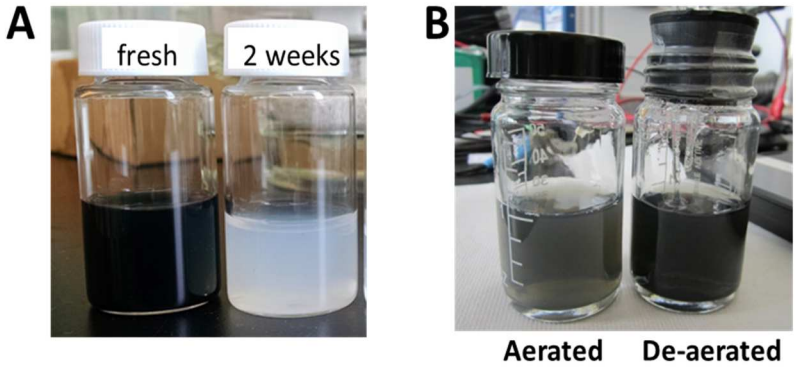

Figure 61. *Photographs of aqueous solutions of delaminated $Ti_3C_2T_x$ flakes showing oxidation.* ***(A)*** *Comparison of fresh solution (left) with one stored in water at ambient conditions for 2 weeks (right).* ***(B)*** *Comparison of flakes suspended in aerated (left) and deaerated by bubbling Ar (right) through deionized water for 72 h.*

To confirm the oxidation and understand its kinetics, the chemical state of $Ti_3C_2T_x$ powders stored in aerated water in the dark – un-sputtered surfaces – was monitored by XPS over time. Aliquots of this solution were taken after certain periods, from which suspended $Ti_3C_2T_x$ powders were separated by centrifugation for analysis. High-resolution XPS spectra in the Ti 2p region of the initial powder and those after being stored in water for 20 h and 1 week are shown in Figure 62A. This spectrum was typical of $Ti_3C_2T_x$, wherein Ti oxides and Ti-F signals were observed, together with Ti-C signals arising from Ti atoms in the interior of the MXene layers (see Section 4.3.2.1 for more details) [85-87]. According to Figure 62A and B, exposure to the water for up to

20 h did not significantly change the chemical state of $Ti_3C_2T_x$ powders. Subtle changes in the spectra (*e.g.*, a more pronounced shoulder at ~457 eV) and an increased contribution from the peak corresponding to Ti(IV) – *viz*. TiO_2 – could be observed after 20 h exposure (Figure 62B) in comparison to the spectra of $Ti_3C_2T_x$ (Figure 62A).

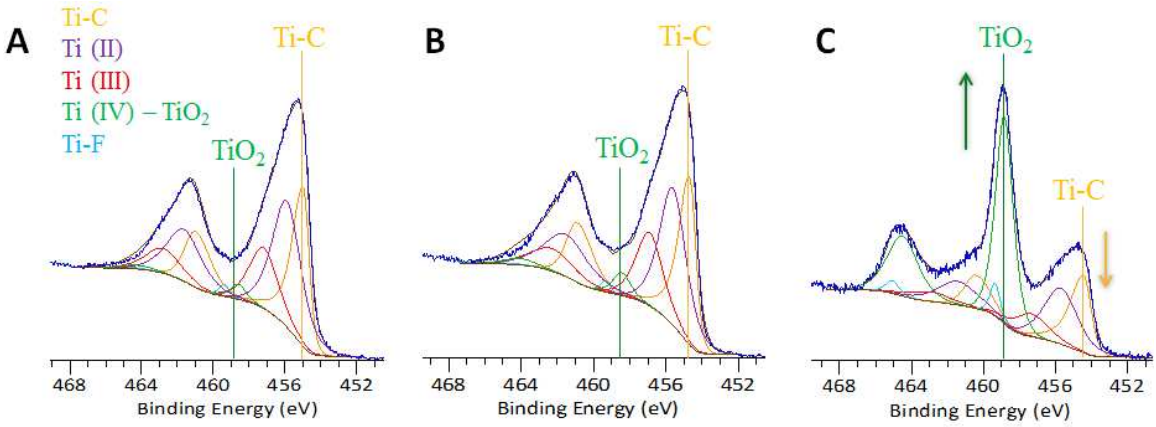

Figure 62. *High-resolution XPS in the Ti2p region for (**A**) initial multilayered $Ti_3C_2T_x$, (**B**) after 20 h, and (**C**) after 1 week in water while being shaken in the dark in aerated conditions. The fits are color-coded; the key is shown on the right of (A). An increase in the Ti $2p_{3/2}$ component corresponding to TiO_2 (green) could be observed at 458.8 eV.*

Although the changes to the spectrum in Figure 62B are slight, after a week of exposure, a peak corresponding to TiO_2 became quite clear (Figure 62C). Concomitant with the increase in the TiO_2 signal, there was a decrease in the Ti-C signal. The component assigned to Ti bound to F also shifted significantly to a lower binding energy (compare Figure 62A and C). All these observations indicated that multilayered $Ti_3C_2T_x$ slowly reacted to form titanium hydroxide and/or TiO_2 [130] on its surface. The slight shift to a lower binding energy for the Ti-C component and the slight shift to higher binding energy for the TiO_2 component over the one week period may indicate the initial

stages of separation of these phases since the local effect of removing oxygen from the MXene into the TiO_2 could cause a shift in electron density. Such long-term oxidation was, most probably, a result of the presence of dissolved oxygen in the solution which acted as an oxidizer, as predicted theoretically [131] and confirmed experimentally herein. This reaction (13) consumes Ti and C, forming TiO_2 and CO_2:

$$Ti_3C_2T_x + O_2 \rightarrow TiO_2 + CO_2 + CO_3^{2-} \quad (13)$$

The oxidation may occur due to O_2 adsorption on under coordinated Ti atoms in $Ti_3C_2T_x$ following the mechanism reported for bulk TiO_x [132]. However, even without dissolved oxygen, delaminated $Ti_3C_2T_x$ single flakes slowly reacted with water, in a fashion reminiscent of the reaction of the topmost 5-30 atomic layers in bulk TiC [133]. It is also in agreement with thermodynamic simulations performed for Ti-C-F-H_2O system at molality of fluorine $m(F^{-1})$ = 0.1 mol/kg at 298.15 K and under 1 atm pressure (Figure 63). A simulated Pourbaix diagram indicated preferential formation of TiO_2, CO_2 and bicarbonate species at typical experimental conditions – 0 eV and nearly neutral pH range. The reaction of $Ti_3C_2T_x$ oxidation in water (14) can thus be suggested as following:

$$Ti_3C_2T_x(s) + H_2O(l) \rightarrow xTiO_2(s) + yHCO_3^- + CO_2(g) \quad (14)$$

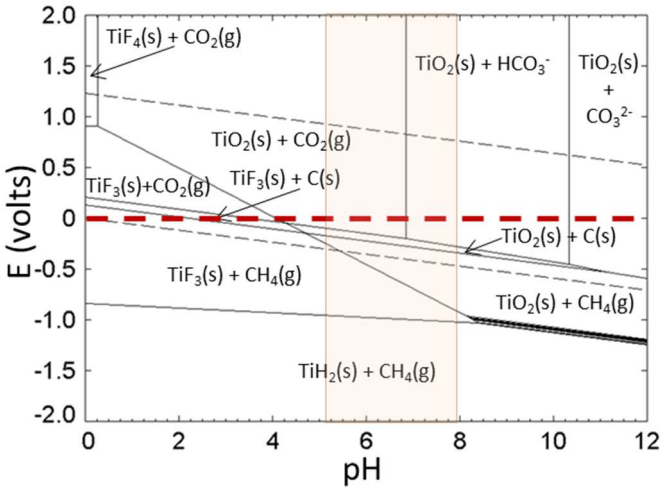

Figure 63. *Pourbaix diagram for Ti-C-F-H_2O system at fluorine molality m(F^{-1}) = 0.1 mol/kg at 298.15K and under 1 atm pressure. Experimental conditions were defined by the line at 0 eV and nearly neutral region highlighted in pink.*

The complete conversion of $Ti_3C_2T_x$ layers into nanoscale TiO_2 was further confirmed by TEM analysis of multilayered $Ti_3C_2T_x$ powder recovered after being kept in aerated water for 3 months. The bright field TEM image (Figure 64A) showed that some MXene particles still retained their planar structure (region I), while others were completely transformed into small crystalline particles (region II). An SAED pattern taken from region I (Figure 64B-I) corresponded to a combination of 3 phases: the original $Ti_3C_2T_x$, and two crystalline forms of TiO_2, anatase and rutile. The calculated d-spacing values of the latter two phases were in a very good agreement with values for anatase and rutile in the JCPDS card PDF#21-1272 and JCPDS PDF#75-1750, respectively (see Table 18). The SAED pattern taken from region II (Figure 64B-II) showed the absence of the $Ti_3C_2T_x$ phase, and brookite (JCPDS PDF#76-1936).

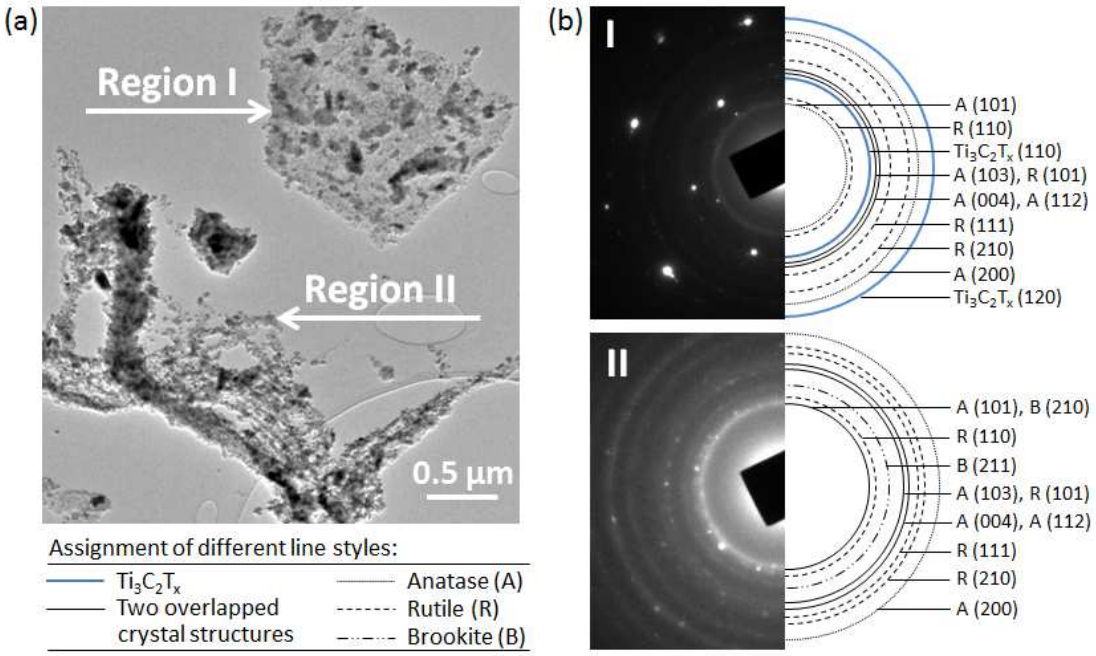

***Figure 64**. (**A**) Bright-field TEM image of multilayer $Ti_3C_2T_x$ powder after 3 months in contact with MB solution in aerated water. (**B**) SAED patterns corresponding to regions I and II shown in (A). A – anatase, R – rutile and B – brookite. [90]*

***Table 18**. Assignment of d-spacing values, d, in Å, calculated from experimental SAED patterns to corresponding crystal lattice plains (hkl) of titanium oxide. Reference values of d-spacings for anatase (A), brookite (B), and rutile (R) were taken from JCPDS database – PDF#21-1272, PDF#76-1936, and PDF#75-1750, respectively.*

Exp. *d* (Å)	TiO_2 (*hkl*)	*d* (Å) from JCPDS database
3.52	A (101) B (210)	3.52 3.52
3.29	R (110)	3.25
2.93	B (211)	2.91
2.46	A (103) R (101)	2.43 2.49
2.37	A (004) A (112)	2.37 2.33
2.23	R (111)	2.19
2.08	R (210)	2.05
1.91	A (200)	1.89
1.72	A (105)	1.69
1.66	A (211) R (220)	1.66 1.62
1.45	R (002)	1.47

At this juncture it is clear that $Ti_3C_2T_x$ undergoes spontaneous oxidation in the presence of oxygen or upon storing in water for prolonged periods of time, showing much faster conversion in the former case and potentially involving parallel processes.

4.6.3.2. Oxidation at Elevated Temperatures

Behavior of $Ti_3C_2T_x$ powder (previously dried in a desiccator at RT for 4 days) in an oxygen atmosphere was also studied using TGA. Figure 65 shows comparison of TG curves for a sample heated in two different environments – air and an inert Ar atmosphere. Similar behavior was observed for both samples up to 200 °C. In both cases, the weight loss was 3.0 wt.%, which could be attributed to the removal of superficial and interstitial water and/or HF residue from the MXene surfaces. Above 200 °C, the $Ti_3C_2T_x$ treated in Ar kept losing weight which could result from the dehydroxylation of the remaining isolated OH groups bonded to the Ti-terminated surface [128] or elimination of physisorbed water embedded between the layers [126]. The total weight loss for this sample was 7.0 %, with respect to the original sample weight.

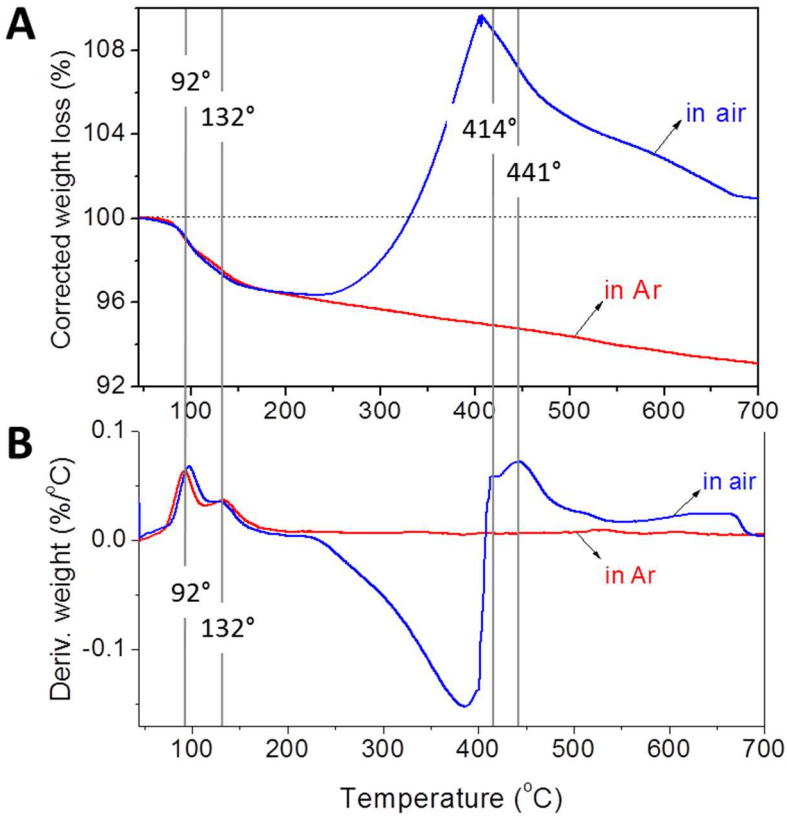

***Figure 65**. (A) TG curves of $Ti_3C_2T_x$ powder analyzed in air (blue curve) and argon (red curve) atmospheres. (**B**) Derivative weight loss curves identified the temperatures where weight losses were most apparent.*

In contrast to the sample treated in Ar, the $Ti_3C_2T_x$ treated in air started gaining weight, reaching its maximum at ~ 400 °C, which was most likely due to O uptake and TiO_2 formation. The further weight loss at higher temperatures may be due to the oxidation of carbon atoms. It was thus suggested that multilayered $Ti_3C_2T_x$ starts oxidizing in air when heated up to 200 ˚C and can be potentially converted into TiO_2 above 400 ˚C. This conclusion is in agreement with other oxidation studies showing that $Ti_3C_2T_x$ can be converted into carbon sheet-supported TiO_2 (rutile) under slow heating up to 450 ˚C in air [134]. It was also found that different crystal structures, particle sizes and morphologies of TiO_2 could be obtained by controlling the heating rate, temperature

range, and exposure time. A schematic of MXene oxidation is shown in Figure 66. *In-situ* TEM study showed that anatase nanocrystals enmeshed in thin sheets of disordered graphitic carbon structures can be obtained *via* flash oxidation at 950 ˚C, while rutile sheets form during slow heating up to 450 ˚C [134, 135].

Figure 66. *Schematic of MXene oxidation and formation of oxide-graphitic disordered carbon hybrid structure.[135]*

4.6.4. Hydrazine Treatment

Figure 67A presents a schematic illustration of the $Ti_3C_2T_x$ layered structure intercalated by hydrazine molecules. Intercalation was evidenced by a shift of the main (0002) XRD peak toward lower 2Θ angles after $Ti_3C_2T_x$ treatment in aqueous HM solution (Figure 67B) that corresponded to the increase of *c*-LP from 20.2 Å to 25.4 Å suggesting – as discussed above in Section 4.5.2.1 – the formation of a nearly complete monolayer of N_2H_4 molecules in each $Ti_3C_2T_x$ interlayer space [136]. The (0002) peak also appeared to be of significantly higher intensity implying the formation of a better organized structure upon intercalation.

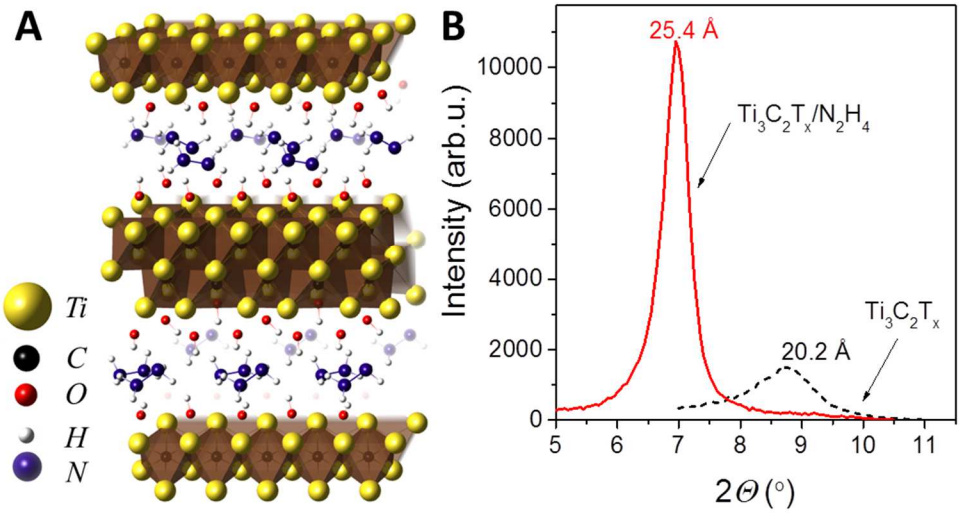

***Figure 67**. (**A**) Structural model of $Ti_3C_2OH+0.5N_2H_4$ (VESTA software was used for visualization). (**B**) XRD patterns around the $Ti_3C_2T_x$ (0002) peak before and after hydrazine treatment; the numbers show corresponding c-lattice parameter values.*

To gain insight into the chemistry changes at the $Ti_3C_2T_x$ surface upon HM treatment, inelastic neutron scattering (INS) analysis, which was highly sensitive to hydrogen atoms (due to their high neutron scattering cross-section compared to other elements), was carried out. In Figure 68, the INS spectrum for the initial $Ti_3C_2T_x$ (black curve) powders revealed the presence of water and hydroxyl groups in the sample. This was evidenced by a broad intermolecular librational band of bound water, extending from 50 to 120 meV, intramolecular H-O-H scissors mode of undissociated H_2O, centered at ~205 meV, and a broad band of superimposed O-H stretching modes in the range 350-460 meV with a maximum at ~415 meV [137, 138]. The latter was a combination of symmetric and asymmetric O-H stretching vibrations coming from water molecules (typically within 390-430 meV) and surface-bound hydroxyl groups at ~450 meV, as reported for hydrated anatase [137]. The extension of stretching modes down to 350 meV implied the formation of a strong O···H-O hydrogen bond network, that caused

weakening of the O-H covalent bonds of the water molecule. In addition, a broad distribution of the translational (below 40 meV) and librational bands (50-120 meV) and absence of distinct peaks within the regions (in particular, no acoustic peak of ice at ~7 meV) suggested that strong hydrogen bonding occurred between the H_2O and OH-terminated $Ti_3C_2T_x$ surfaces, rather than between the water molecules themselves [139].

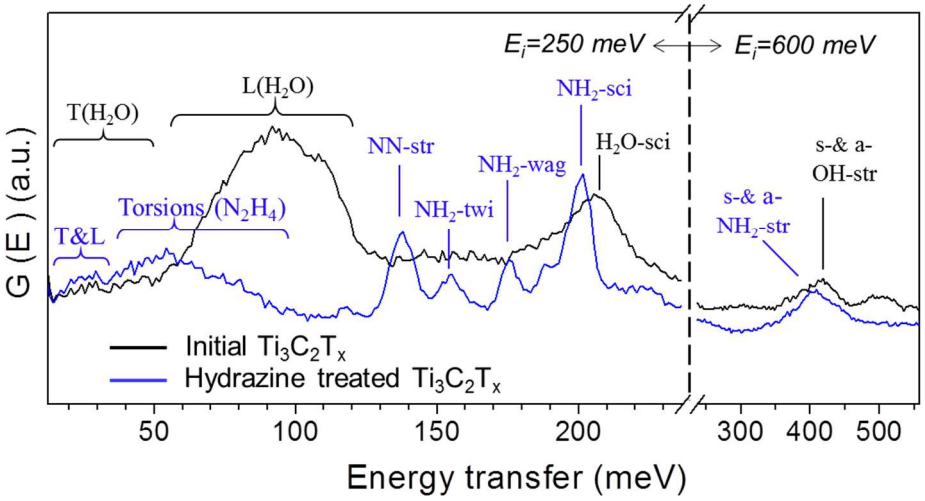

Figure 68. *Inelastic neutron scattering spectra for $Ti_3C_2T_x$ before (black curve) and after (blue curve) hydrazine treatment measured with different E_i, 250 and 600 meV, at 7 K.*

In contrast to the INS spectrum of the initial $Ti_3C_2T_x$, the above H_2O/OH vibration modes mostly disappeared after HM treatment (see blue curve in Figure 68). Thus, librational and bending modes of un-dissociated water and two bands of low intensity at ~300 and 500 meV – overtones due to bending and stretching modes, respectively, [140] – vanished completely. The intensity of the OH stretching modes greatly decreased as well. Instead, sharp peaks, indicative of the stretching and bending modes of hydrazine molecules, appeared. Those included the N-N stretching mode at 137

meV, NH_2 bending modes (rocking, twisting, waging and scissoring at 117, 155, 176, and 200 meV, respectively) and NH_2 stretching modes [141, 142]. The latter appeared as a broad band in the range between 330 and 470 meV which could be resolved into 3 modes – two symmetric stretches at 369 and 402, and one asymmetric stretch at 433 meV, which was in a good agreement with those reported for hydrazine at 10 K (365, 397 and 432 meV, respectively) [142]. Note that this region might be also affected by H_2O/OH stretches found in the sample before intercalation. A low-energy range up to 100 meV may be assigned to T and L (up to 40 meV) and torsional modes (40-100 meV) of hydrazine. The modes appeared to be quite broad, and no peaks could be seen that suggested a low packing density of N_2H_4 within the $Ti_3C_2T_x$ structure, which agreed with the conclusions concerning nearly monolayer intercalation. Thus, comparison of the INS spectra of $Ti_3C_2T_x$ before and after HM treatment confirmed intercalation of hydrazine molecules and also suggested the removal of larger amount of H_2O/OH upon HM treatment.

In order to acquire complementary information about changes in the $Ti_3C_2T_x$ surface chemistry and impurities content after hydrazine treatment, TPD-MS was performed. A spectrum recorded for pristine $Ti_3C_2T_x$ (Figure 69A) revealed a large weight loss in the range of 100-200 °C which – as discussed above – was related to water evolution. Comparison of the TPD-MS data for pristine and hydrazine intercalated $Ti_3C_2T_x$ (Figure 69A and B, respectively) showed a significant decrease in the intensity in this region suggesting removal of a large amount of H_2O upon HM treatment, which was in perfect agreement with the INS data.

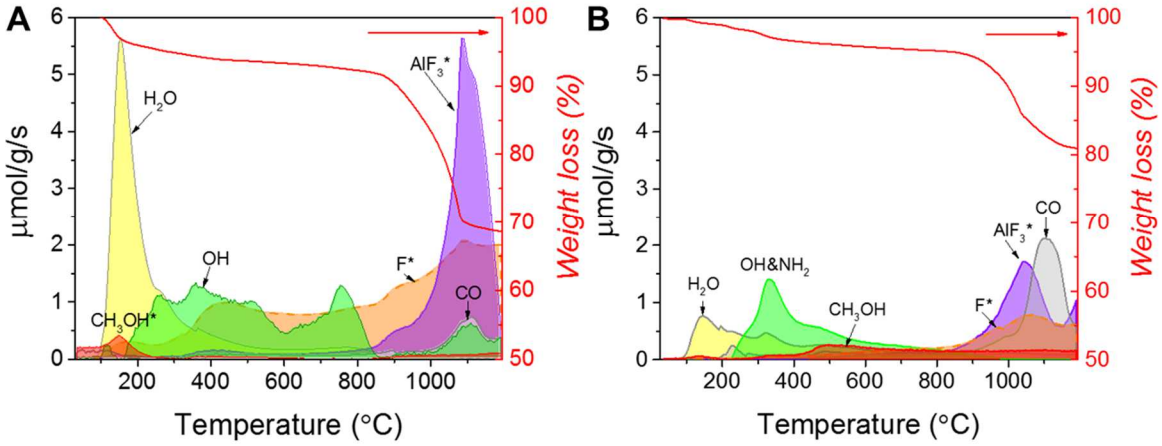

***Figure 69**. Temperature programmed desorption mass spectroscopy data for $Ti_3C_2T_x$ (**A**) before and, (**B**) after hydrazine treatment.*

A second large weight loss occurred in the range 800-1200 °C which could be due to the thermal decomposition of $AlF_3 \cdot nH_2O$ [143] – a byproduct of the Ti_3AlC_2 HF etching during $Ti_3C_2T_x$ synthesis. Similar to water, there was a significant decrease in the peak intensity in the 800-1200 °C region after HM treatment. Considering the solubility of AlF_3 in water, the intensity drop might be a result of salt being washed out during the treatment.

The remaining weight loss was related to the thermal desorption of surface functionalities and possible restructuring products, such as OH, F and oxidized C. By comparing Figure 69A and B, it was confirmed that $Ti_3C_2T_x$ presented a higher amount of hydroxyl and methoxy groups than $Ti_3C_2T_x/N_2H_4$. It is important to note that in case of $Ti_3C_2T_x/N_2H_4$ it was impossible to distinguish the contributions of the hydrazine desorption and the hydroxyl, since both of these yielded species with the same *m/z*. However, considering the differences in OH &NH_2 profiles before and after treatment, it was reasonable to assume that OH was partially removed and exchanged with NH_2.

As an outcome of hydrazine treatment of $Ti_3C_2T_x$, it was found that such treatment led to significant improvements in the performance of supercapacitors compared to pristine non-treated material, doubling gravimetric (up to 200 F/g) and volumetric (up 250 F/cm^3) capacitances in sulfuric acid electrolyte along with excellent rate performance and cyclability.

4.6.5. Noble Metal Particle Deposition

It was found that noble metal particles, *viz*. gold (Au), can be readily deposited on $Ti_3C_2T_x$ surfaces. Two deposition procedures were used. First, deposition of gold nanoparticles (Au-NPs) was performed based on a reduction reaction (15) between Au^{3+} ($HAuCl_4$) and sodium borohydrate ($NaBH_4$):

$$8HAuCl_4 + 3NaBH_4 + 9H_2O \rightarrow 8Au + 3H_3BO_3 + 3NaCl + 29\ HCl \qquad (15)$$

Being positively charged (Figure 70A), the NPs formed readily adsorbed on the negatively charged surfaces of the *d*-$Ti_3C_2T_x$ flakes, as confirmed by the TEM images shown in Figure 70B and C. The deposited Au was of a wide size range, from 30 to 150 nm, and non-uniformly distributed across the *d*-$Ti_3C_2T_x$ surface.

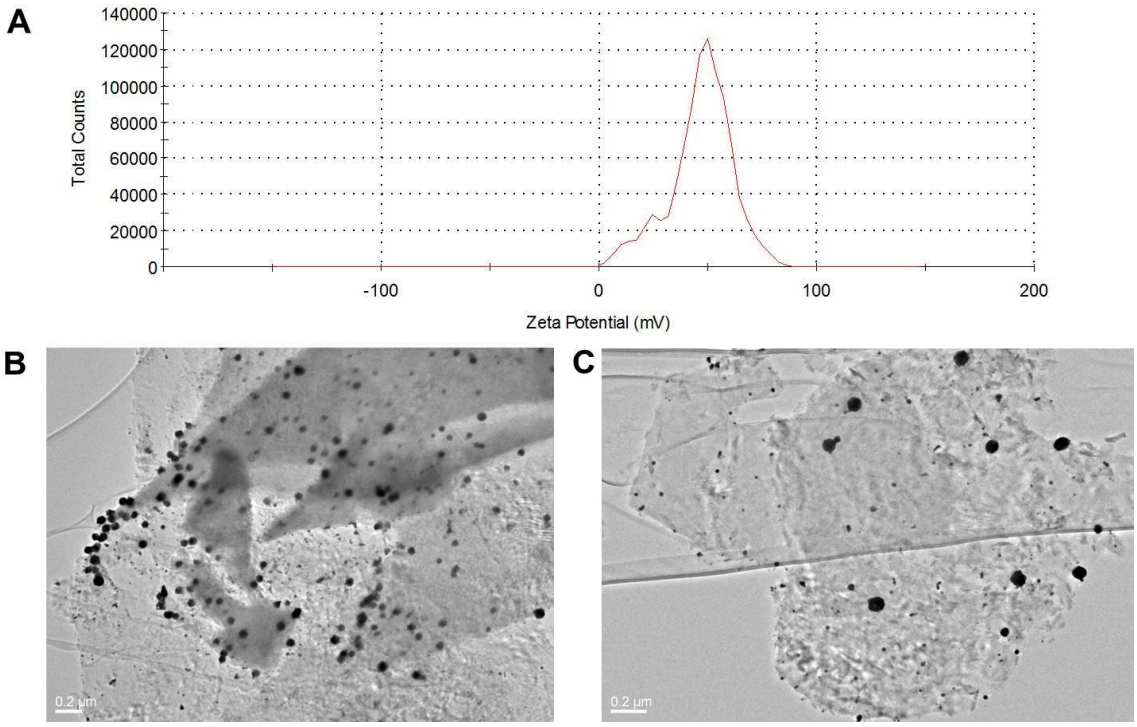

***Figure 70**. (**A**) Zeta potential measurements for colloidal Au-NPs solution. (**B, C**) TEM images of d-$Ti_3C_2T_x$ flakes with Au-NPs on the surface produced by a chemical deposition method. Au deposits appear as dark spots in the images.*

Much better control over the size and distribution was achieved using a photo-assisted deposition method in which $HAuCl_4$ was added directly to a *d*-$Ti_3C_2T_x$ flakes solution and illuminated with UV or kept in the dark. This technique was based on the idea that $Ti_3C_2T_x$ acts as a photocatalyst:

$$AuCl_4^- + 2H_2O \xrightarrow[h\nu]{\text{Photocatalyst}} Au^0 + O_2 + 4H^+ + 4Cl^-. \quad (16)$$

As a result of photodeposition, uniformly distributed Au-NPs were formed on the *d*-$Ti_3C_2T_x$ surfaces. Importantly, it was shown that the size of deposits depend strongly on the wavelength of light used. Small Au-NPs of 2-5 nm in diameter were formed when the reactive solution was irradiated with UV light (Figure 71A and B) whereas much larger particles of 30-50 nm in diameter were deposited when the solution was kept in the dark

(Figure 71C). Such material could be expected to be further used for a variety of applications in catalysis and electrocatalysis.

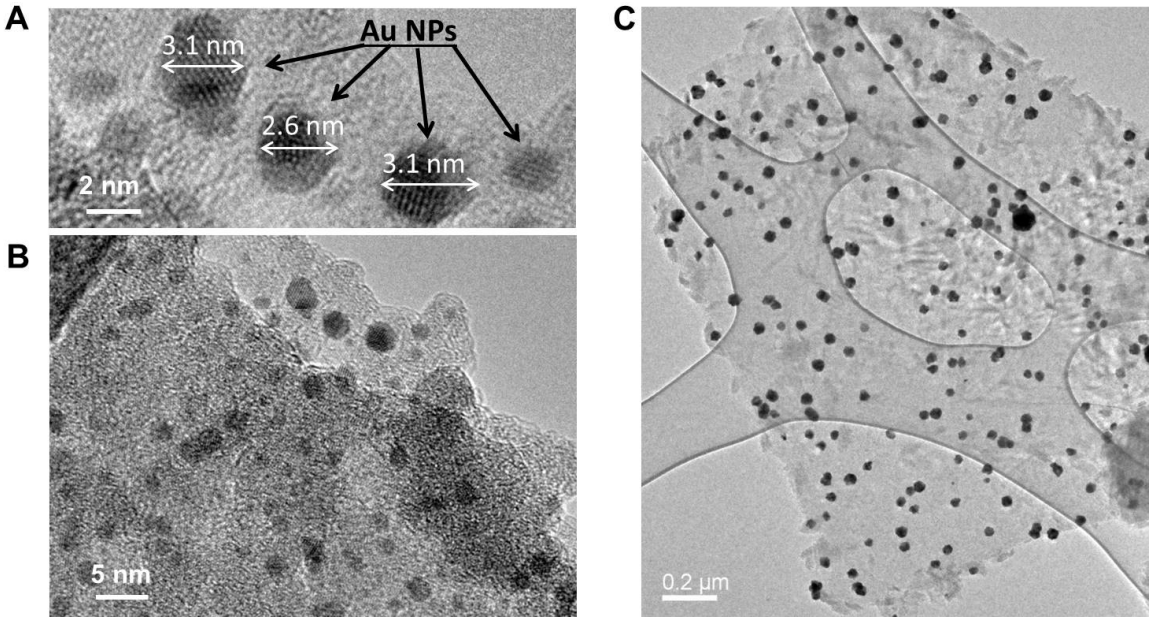

Figure 71. *TEM images of d-$Ti_3C_2T_x$ flakes with Au-NPs on the surface produced by photo-assisted deposition method; (**A**) under UV irradiation and, (**B**) in the dark.*

CHAPTER 5: SUMMARY AND FUTURE WORK

In this work, the chemistry of $Ti_3C_2T_x$, a representative of a new family of 2D materials, known as MXenes, was investigated. Particular attention was given to studying its structure, properties and developing modification routes to improve its performance in energy storage devices as well as understand its potential for other application fields.

Kinetics of the extraction of Al from Ti_3AlC_2 in 50 wt.% HF used to synthesize high quality $Ti_3C_2T_x$ powder was investigated. Three main parameters important in the etching process, *viz*: time, temperature and initial particle size were identified. It was thus found that increasing the temperature and immersion times, and decreasing the Ti_3AlC_2 particle size, led to faster conversion of Ti_3AlC_2 to its 2D $Ti_3C_2T_x$ counterpart.

Exfoliated $Ti_3C_2T_x$ was comprised of multilayered structures consisting of electron transparent sheets, with a morphology that is reminiscent of graphene, such as the formation of arch-shaped edges. The surface of the synthesized $Ti_3C_2T_x$ appeared to be terminated with OH, O and F groups sitting on top of the Ti atom in the layer beneath the next layer of C atom, *viz.* at the (0, 0, *z*) position.

The $Ti_3C_2T_x$ surfaces were found to be negatively charged in aqueous media. As a result, MXene's ability to spontaneously intercalate cations, both metal and organic, was established. Intercalation was found to depend on the cation nature (*i.e.*, size and charge) and was pH-dependent. It was also found that chemical intercalation of small molecules was possible and depended on the intercalant's dipole moment, size and its ability to dissociate in solution to form positively charged species.

Following the idea of intercalation, a procedure for the large-scale delamination of $Ti_3C_2T_x$ into single layers was developed *via* sonication of DMSO intercalated $Ti_3C_2T_x$ in deionized water or propylene carbonate. Filtration of the colloidal solution of delaminated $Ti_3C_2T_x$ layers resulted in a thin, free-standing flexible "paper" which further showed a promise as electrodes for energy storage devices.

Another delamination procedure involving isopropyl amine as an intercalant was also suggested. The latter appeared to be more universal and was used to delaminate other members of the MXene family, *viz*. Nb_2CT_x.

$Ti_3C_2T_x$ was also demonstrated to undergo relatively fast spontaneous oxidation when stored in the presence of dissolved oxygen and in water. It was also suggested to use an inert atmosphere or vacuum as an environment for the MXenes' storage and handling in the future.

$Ti_3C_2T_x$ was tested for its adsorptive and photocatalytic properties. It was shown to exhibit excellent adsorption toward cationic dyes, best described by a Freundlich isotherm, showing exceptionally strong, and irreversible, bonding of the adsorbent to the $Ti_3C_2T_x$ surfaces in aqueous solutions. It was also shown that dyes, both cationic and anionic, could degrade in solutions containing $Ti_3C_2T_x$ under UV light.

A summary of the above mentioned and other ways of $Ti_3C_2T_x$ modification (*Figure 72*) is shown in the schematic below:

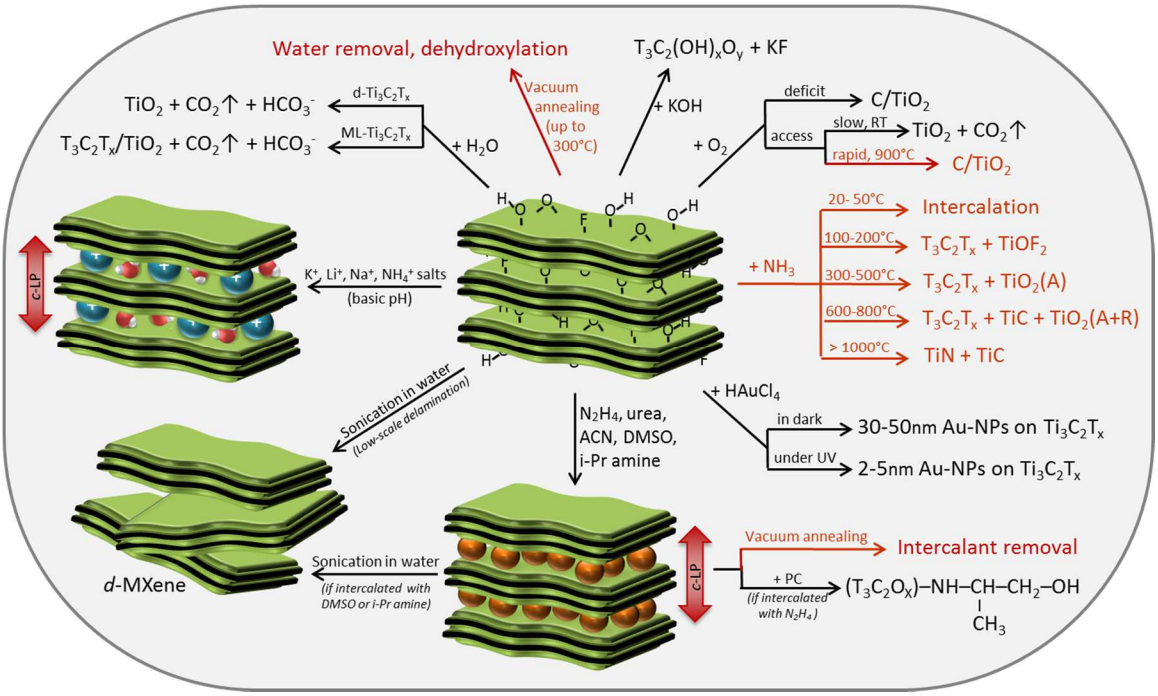

***Figure 72**. Schematic of ways of chemical and structural modification of $Ti_3C_2T_x$.*

Beyond energy storage applications, this work explored the potential use of $Ti_3C_2T_x$ as a catalyst, photo-and electrocatalyst, chemical sensor and an adsorbent for positively charged species.

Future work on this project should pursue the following goals:

- Synthesizing $Ti_3C_2T_x$ with *no* or with a *single type* of surface functional group and exploring its properties.
- Investigating the effect of intercalants on $Ti_3C_2T_x$ properties.
- Optimizing the intercalation and delamination procedures.
- Obtaining a complete understanding of the mechanisms of intercalation, oxidation and photocatalysis.
- Finding other attractive properties of $Ti_3C_2T_x$.

- Developing other routes for $Ti_3C_2T_x$ surface and structure modification (for instance, using plasma treatment).
- Characterizing single-layers of $Ti_3C_2T_x$ including electronic, magnetic, optical, and mechanical properties.
- Developing safer routes of MXene synthesis to avoid using HF in the process.
- Exploring the potential of $Ti_3C_2T_x$ application as a photo- and electrocatalyst.

Appendix A: Molecular Dynamics Simulations for N_2H_4-$Ti_3C_2T_x$

The Universal Force Field (UFF) parameters were estimated from simple relations that depended only on the element, its hybridization, and connectivity and were not parameterized by any experimental data. While UFF precision could be inferior to more specialized force fields, it was necessary to trade accuracy for generality, required for the systems considered here. In future, for more precise computational studies, a force field parameterized by experimental data and including the combination of elements and bonds specific for intercalated MXenes should be developed, similar to those developed for clays (*e.g.*, the Clay Force Field [144]).

To validate the force field and the methodology used for computations, geometry optimization of α-Ti_3AlC_2 (MAX phase) was performed and the optimized structure was compared to the available data. A $P6_3/mmc$ space group α-Ti_3AlC_2 unit cell was constructed using structural parameters from Ref. [48] and then relaxed using UFF, while subjected to an isostatic external pressure of 0.1 MPa (1 atm) and allowing for cell optimization with the following symmetry constrains: $a=b$; $\alpha=\beta=90°$; $\gamma=120°$. Geometry optimization convergence tolerance parameters (Energy = 0.02 cal/mol, Force = 1 cal/mol/Å, Stress = 1 MPa, Displacement = 0.00001 Å) were the same as those used for MD simulations (see Methods in the main text). The optimized α-Ti_3AlC_2 structure is shown in Figure 73. The parameters of this structure are compared to the available literature data in Table 19. The differences in structural parameters were in the range 0.3-6.4 %, with all distances and cell parameters computed in this work being slightly larger

when compared to the literature data. Therefore, UFF was used to model hydrazine intercalated MXene.

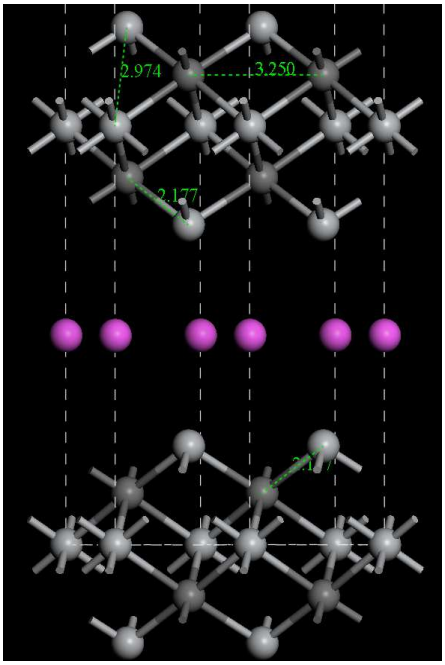

Figure 73. *A bottom part of the Universal Force Field optimized structure of α-Ti_3AlC_2 unit cell. The interatomic distances shown and lattice parameters of the optimized structure are compared to the literature data in Table 19. In this figure carbon is shown in dark grey, titanium in light grey, aluminum in pink.[87]*

Table 19*. Structural parameters of α-Ti_3AlC_2. [87]*

Parameter	This work (UFF)	Literature [145]	Difference, % [a]
Lattice parameters *a* and *b* (Å)	3.250	3.023-3.087	+6.4
Lattice parameter *c* (Å)	19.607	18.287-18.652	+6.2
$d^{Ti\text{-}C}$ (Å)	2.177	2.082	+4.6
$d^{Ti\text{-}Ti}$ (Å)	2.974	2.966	+0.3
$d^{C\text{-}C}$ (Å)	3.250	3.082	+5.5

[a] The difference is calculated as

$$\left(\text{Value}_{\text{This work}} - \text{Average value}_{\text{Literature}}\right)/\text{Average value}_{\text{Literature}} \cdot 100$$

Appendix B: Deconvolution of (0002) XRD Ti_3AlC_2 and $Ti_3C_2T_x$ peaks

To separate the contributions from two superimposed MXene and MAX phase peaks around 2θ ≈ 9°, the crystal lattice parameters and intensity ratios were estimated using a summed Gaussian/Lorentzian peak-fitting after baseline corrections. The peak deconvolution was performed using the LabSpec v4.02 software (see examples in Figure 74).

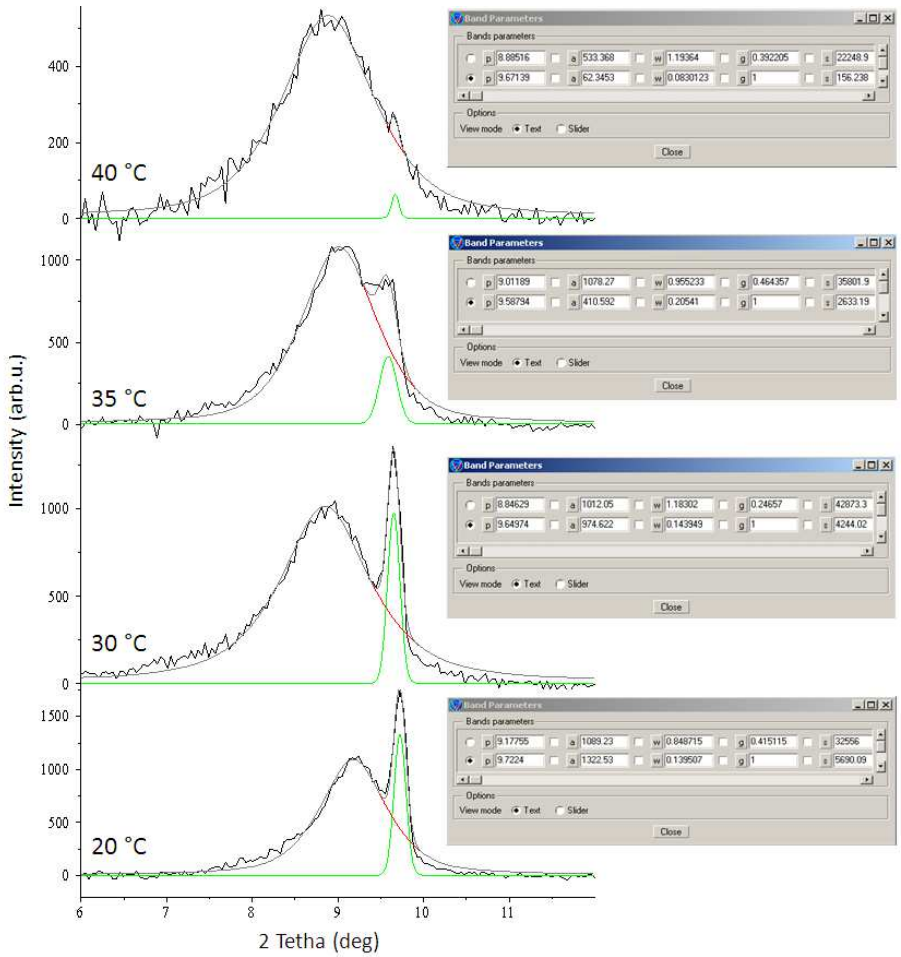

***Figure 74**. Examples of curve fits of (0002) XRD peaks of MAX (narrow peaks) and MXene (broad peaks).*

Appendix C: Small-Angle Neutron Scattering Calculations

Small-Angle Neutron Scattering (SANS) scattering intensity I(Q) was collected as a function of wave vector transfer $Q = \frac{4\pi sin\theta}{\lambda}$, where θ is half the scattering angle and λ is the neutron wavelength. The position of the Q_1 peak observed in the 0.4 – 1.0 $Å^{-1}$ range, was related to the *d-spacing* of material, d, from diffraction by $Q = \frac{2\pi}{d}$. The signal intensity was proportional to the square of the neutron scattering length density (NSLD) contrast between a nanostructured material and its surroundings. The NSLD of a material depends on its composition and density. For a given material phase *j*, the NSLD ρ_j^*, is obtained from

$$\rho_j^* = \sum_{i=1}^{N} b_i \frac{\rho_j N_A}{M_j}, \tag{C-1}$$

where b_i is the coherent scattering length of the i^{th} atom, N is the total number of atoms in the molecule, ρ_j is the mass density, and M_j is the molar mass. In case of $Ti_3C_2T_x$ which is composed of Ti_3C_2 sheets and the interlayer species χ, the scattered intensity at the Q peak can be expressed as:

$$I(Q_1) \propto a_1 * \left(\Delta\rho_{layer}^*\right)^2, \tag{C-2}$$

where $\Delta\rho_{layer}^* = \rho_\chi^* - \rho_{MX}^*$.

To calculate the *skeletal density* of MXene layers in this way, the scattering intensity from Q_1 peak was modeled analytically with a Gaussian term to describe the peak, along with Q^{-2}-dependent and constant background terms:

$$I(Q) = A_1 * \frac{e^{-2((Q-Q_1)/w_1)^2}}{\left(w_{1*}\sqrt{\pi/_2}\right)} + BQ^{-2} + C. \quad \text{(C-3)}$$

The peak intensity is proportional to the square of the NSLD difference:

$$\frac{A_1}{\left(w_{1*}\sqrt{\pi/_2}\right)} = a_1 * \left(\Delta\rho^*_{layer}\right)^2. \quad \text{(C-4)}$$

At the peak maximum, the intensity is related to $\left(\Delta\rho^*_{layer}\right)^2$ by:

$$I(Q_1) = a_1 * \left(\Delta\rho^*_{layer}\right)^2 + BQ_1^{-2} + C, \quad \text{(C-5)}$$

where a_1 is a normalization constant, and BQ_1^{-2} and C are diffuse and incoherent scattering backgrounds, respectively, and do not contribute to the interlayer structure. Comparison of $I(Q)$ for the MXene samples with different interlayer species allows to calculate skeletal density of a single MXene layer.

The *Porod scattering* at low Q was modeled with the expression:

$$I(Q) = A\left(\Delta\rho^*_{particle}\right)^2 Q^{-p}, \quad \text{(C-6)}$$

with A constant and $\Delta\rho^*_{particle}$ representing the NSLD difference between the micron sized particle and air, and thus the particle's overall composition.

The average $Ti_3C_2T_x$ individual *sheet thickness* and *lateral dimensions* of the nanosized domains were modeled using a parallelepiped form factor [84, 146] with edge lengths A, B, and C. In this model the length A gives a measure of the size of the $Ti_3C_2T_x$ stack size, and thus the number of layers which comprise each individual sheet. B and C give a measure of the size of the domains that extend throughout a sheet. The scattering data was modeled from 0.01 to 0.2 $Å^{-1}$ using an expression that accounts for the Porod scattering, the parallelpiped form factor, and a constant background term:

$$I_{P,F}(Q) = AQ^{-p} + F_{pp}(Q) + C \quad \text{(C-7)}$$

Appendix D: Pair Distribution Function Technique

The rapid acquisition pair distribution function (PDF) technique [147] was used with an X-ray energy of 67.4194 keV (λ = 0.1839 Å). A large area 2 D Perkin Elmer detector (2048 × 2048 pixels and 200 × 200 μm pixel size) was mounted orthogonal to the beam path with a sample-to-detector distance of 204.099 mm. The raw 2D data were azimuthally integrated and converted to 1D intensity versus 2θ using FIT2D [148]. PDFGETX3 [149] was used to correct and normalize the diffraction data and then Fourier transform them to obtain the experimental PDF, *G(r)*, according to *G(r)* = $2/\pi \int_{Q_{min}}^{Q_{max}} Q[S(Q)-1]\, sinQr\mathrm{d}Q$. Here, Q was the magnitude of the momentum transfer on scattering and *S(Q)* was the properly corrected and normalized powder diffraction intensity measured from Q_{min} to Q_{max} [150]. *G(r)* gives the probability of finding a pair of atoms separated by a distance of *r*. Nickel was also measured as a standard material to calibrate the sample-detector distance and to determine the Q_{damp} and Q_{broad} parameters which were the parameters used to correct the PDF envelope function for the instrument resolution effects [151, 152]. The refined values of Q_{damp} = 0.0416 $Å^{-1}$ and Q_{broad} = 0.0172 $Å^{-1}$ were allowed to vary in the subsequent model fits to PDF data. Structural modeling was carried out using the PDFGUI and SRFIT programs [152].

Appendix E: Adsorption Models and Isotherms

Two models, Langmuir and Freundlich, were used to fit the experimental dye adsorption data. Both models are commonly used to describe adsorption processes at liquid-solid interfaces. The Langmuir model assumes that there is only a monolayer of adsorbate on the adsorbent surface and that all adsorption sites are equivalent, each accommodating only one adsorbate molecule. This model also assumes that all adsorbate molecules are identical (and so this model was not applicable to mixtures of competitive adsorbates) and do not interact with each other. With these assumptions, the Langmuir isotherm equation can be written as [91]:

$$A = A_{max} \frac{K_L C_{Eq}}{1+K_L C_{Eq}}, \quad \text{(E-1)}$$

where A and A_{max} are the adsorbent adsorption capacity and the maximum adsorption capacity of a monolayer of adsorbate, respectively. Both are expressed as the mass of adsorbate per mass of adsorbent in mg/g. The constant, K_L, characterizes the strength of adsorbate binding to the adsorbent, in mL/mg, and C_{Eq} is the concentration of the adsorptive in solution (in mg/mL) in equilibrium with the adsorbate and adsorbent. To estimate whether adsorption was favorable, the separation factor, or equilibrium parameter, R_L has been proposed [92]:

$$R_L = \frac{1}{1+K_L C_0}, \quad \text{(E-2)}$$

where C_0 is the initial concentration of adsorptive, in mg/mL.

The Freundlich isotherm corresponds to a situation where adsorption sites of different adsorption energies and affinities toward an adsorbate are involved. At the same

time, the adsorbate molecules need not be identical. This empirical model had no limitations on the number of the adsorbate layers on the surface of the substrate and can be expressed by the equation [93]:

$$A = K_F C_{Eq}^{(1/\nu)}, \tag{E-3}$$

where A is the adsorption capacity of adsorbent in mg/g, K_F and ν are empirical constants related to the adsorption capacity of the adsorbent and the favorability of adsorption process, respectively. C_{Eq} is the concentration of the adsorptive in solution (in mg/mL) in equilibrium with the adsorbate and adsorbent.

Appendix F: Intercalation of Different MXenes

Table 20. *Intercalants for MXenes of different chemistry.*

Intercalant	MXene						
	$Ti_3C_2T_x$	**Nb_2CT_x**	**$TiNbCT_x$**	**V_2CT_x**	**Ti_3CNT_x**	**$Nb_4C_3T_x$**	**$Ta_4C_3T_x$**
Hydrazine	+	NA	+	NA	+	NA	-
DMSO	+	-	-	+	-	-	-
i-PrA	+	+	NA	-	NA	+	NA
TMAH	+	-	+	-	-	NA	NA
NaOAc	+	-	-	+	-	NA	+

Note: "+" and "-" stand for good and bad intercalant–host match, respectively. "NA" stands for Not Available.

LIST OF REFERENCES

1. Stoller, M.D., et al., *Graphene-based ultracapacitors.* Nano Letters, 2008. **8**(10): p. 3498-502.

2. Bizeto, M.A., A.L. Shiguihara, and V.R.L. Constantino, *Layered niobate nanosheets: building blocks for advanced materials assembly.* Journal of Materials Chemistry, 2009. **19**(17): p. 2512-2525.

3. Sato, K., et al., *A mechanism of lithium storage in disordered carbons.* Science, 1994. **264**(5158): p. 556-558.

4. Yoo, E., et al., *Large reversible Li storage of graphene nanosheet families for use in rechargeable lithium ion batteries.* Nano Letters, 2008. **8**(8): p. 2277-2282.

5. Schwierz, F., *Graphene transistors.* Nature Nanotechnology, 2010. **5**(7): p. 487-496.

6. Radisavljevic, B., et al., *Single-layer MoS_2 transistors.* Nature Nanotechnology, 2011. **6**(3): p. 147-150.

7. Novoselov, K.S., et al., *Electric field effect in atomically thin carbon films.* Science, 2004. **306**(5696): p. 666-669.

8. Stankovich, S., et al., *Graphene-based composite materials.* Nature, 2006. **442**(7100): p. 282-286.

9. Dresselhaus, M.S. and G. Dresselhaus, *Intercalation compounds of graphite.* Advances in Physics, 1981. **30**(2): p. 139-326.

10. Pinnavaia, T.J., *Intercalated clay catalysts.* Science, 1983. **220**(4595): p. 365-371.

11. Ogawa, M. and K. Kuroda, *Photofunctions of intercalation compounds.* Chemical Reviews, 1995. **95**(2): p. 399-438.

12. Podsiadlo, P., et al., *Ultrastrong and stiff layered polymer nanocomposites.* Science, 2007. **318**(5847): p. 80-83.

13. Ma, R.Z. and T. Sasaki, *Nanosheets of oxides and hydroxides: Ultimate 2D charge-bearing functional crystallites.* Advanced Materials, 2010. **22**(45): p. 5082-5104.

14. McKelvy, M.J. and W.S. Glaunsinger, *Molecular intercalation reactions in lamellar compounds.* Annual Review of Materials Science, 1990. **41**(1): p. 497-523.

15. Novoselov, K.S., et al., *Two-dimensional atomic crystals.* Proceedings of the National Academy of Sciences of the United States of America, 2005. **102**(30): p. 10451-10453.

16. Shih, C.J., et al., *Bi- and trilayer graphene solutions.* Nature Nanotechnology, 2011. **6**(7): p. 439-445.

17. Eda, G. and M. Chhowalla, *Chemically derived graphene oxide: Towards large-area thin-film electronics and optoelectronics.* Advanced Materials, 2010. **22**(22): p. 2392-2415.

18. Kumar, A., et al., *Direct synthesis of lithium-intercalated graphene for electrochemical energy storage application.* ACS Nano, 2011. **5**(6): p. 4345-4349.

19. Coleman, J.N., et al., *Two-dimensional nanosheets produced by liquid exfoliation of layered materials.* Science, 2011. **331**(6017): p. 568-571.

20. Zhang, Z., et al., *Two-dimensional tetragonal TiC monolayer sheet and nanoribbons.* Journal of the American Chemical Society, 2012. **134**(47): p. 19326-19329.

21. Terrones, M., *Materials science: Nanotubes unzipped.* Nature, 2009. **458**(7240): p. 845-846.

22. Eda, G., et al., *Photoluminescence from chemically exfoliated MoS_2.* Nano Letters, 2011. **11**(12): p. 5111-5116.

23. Naguib, M., et al., *Two-dimensional nanocrystals produced by exfoliation of Ti_3AlC_2.* Advanced Materials, 2011. **23**(37): p. 4248-4253.

24. Naguib, M., et al., *Two-dimensional transition metal carbides.* ACS Nano, 2012. **6**(2): p. 1322-1331.

25. Naguib, M., et al., *MXene: a promising transition metal carbide anode for lithium-ion batteries.* Electrochemistry Communications, 2012. **16**(1): p. 61-64.

26. Come, J., et al., *A Non-aqueous asymmetric cell with a Ti_2C-based two-dimensional negative electrode.* Journal of the Electrochemical Society, 2012. **159**(8): p. A1368-A1373.

27. Tang, Q., Z. Zhou, and P.W. Shen, *Are MXenes promising anode materials for Li ion batteries? Computational studies on electronic properties and Li storage capability of Ti_3C_2 and $Ti_3C_2X_2$ (X = F, OH) monolayer.* Journal of the American Chemical Society, 2012. **134**(40): p. 16909-16916.

28. Orlita, M., et al., *Approaching the Dirac point in high-mobility multilayer epitaxial graphene.* Physical Review Letters, 2008. **101**(26): p. 267601.

29. Balandin, A.A., *Thermal properties of graphene and nanostructured carbon materials.* Nature Materials, 2011. **10**(8): p. 569-581.

30. Lee, C., et al., *Measurement of the elastic properties and intrinsic strength of monolayer graphene.* Science, 2008. **321**(5887): p. 385-388.

31. Nair, R.R., et al., *Fine structure constant defines vsual transparency of graphene.* Science, 2008. **320**(5881): p. 1308.

32. Pacile, D., et al., *The two-dimensional phase of boron nitride: Few-atomic-layer sheets and suspended membranes.* Applied Physics Letters, 2008. **92**(13).

33. J.A. Wilsona, A.D.Y., *The transition metal dichalcogenides discussion and interpretation of the observed optical, electrical and structural properties.* Advances in Physics, 1969. **19**(73): p. 193-335.

34. Takahashi, N., H. Hata, and K. Kuroda, *Exfoliation of layered silicates through immobilization of imidazolium groups.* Chemistry of Materials, 2010. **23**(2): p. 266-273.

35. Luckham, P.F. and S. Rossi, *The colloidal and rheological properties of bentonite suspensions.* Advances in Colloid and Interface Science, 1999. **82**(1-3): p. 43-92.

36. Watanabe, K., T. Taniguchi, and H. Kanda, *Direct-bandgap properties and evidence for ultraviolet lasing of hexagonal boron nitride single crystal.* Nature Materials, 2004. **3**(6): p. 404-409.

37. Lin, Y. and J.W. Connell, *Advances in 2D boron nitride nanostructures: nanosheets, nanoribbons, nanomeshes, and hybrids with graphene.* Nanoscale, 2012. **4**(22): p. 6908-6939.

38. Tang, Q. and Z. Zhou, *Graphene-analogous low-dimensional materials.* Progress in Materials Science, 2013. **58**(8): p. 1244-1315.

39. Liu, Z., et al., *Direct growth of graphene/hexagonal boron nitride stacked layers.* Nano Letters, 2011. **11**(5): p. 2032-2037.

40. Zhan, Y., et al., *Large-area vapor-phase growth and characterization of MoS_2 atomic layers on a SiO_2 substrate.* Small, 2012. **8**(7): p. 966-971.

41. Nicolosi, V., et al., *Liquid exfoliation of layered materials.* Science, 2013. **340**(6139): p. 1226419.

42. Zhou, K.G., et al., *A mixed-solvent strategy for efficient exfoliation of inorganic graphene analogues.* Angewandte Chemie International Edition, 2011. **50**(46): p. 10839-10842.

43. Joensen, P., R. Frindt, and S.R. Morrison, *Single-layer MoS_2.* Materials Research Bulletin, 1986. **21**(4): p. 457-461.

44. Walker, G. and W. Garrett, *Chemical exfoliation of vermiculite and the production of colloidal dispersions.* Science, 1967. **156**(3773): p. 385-387.

45. Barsoum, M.W., *The M(N+1)AX(N) phases: A new class of solids; Thermodynamically stable nanolaminates.* Progress in Solid State Chemistry, 2000. **28**(1-4): p. 201-281.

46. Barsoum, M.W. and T. El-Raghy, *The MAX phases: Unique new carbide and nitride materials - Ternary ceramics turn out to be surprisingly soft and machinable, yet also heat-tolerant, strong and lightweight.* American Scientist, 2001. **89**(4): p. 334-343.

47. Sun, Z.M., *Progress in research and development on MAX phases: a family of layered ternary compounds.* International Materials Reviews, 2011. **56**(3): p. 143-166.

48. Eklund, P., et al., *The $M_{n+1}AX_n$ phases: Materials science and thin-film processing.* Thin Solid Films, 2010. **518**(8): p. 1851-1878.

49. Barsoum, M.W. and M. Radovic, *Elastic and mechanical properties of the MAX phases.* Annual Review of Materials Research, Vol 41, 2011. **41**: p. 195-227.

50. Barsoum, M.W., et al., *Dislocations, kink bands and room temperature plasticity of Ti_3SiC_2.* Metallurgical and Materials Transactions, 1999. **30A**: p. 1727-1738

51. Barsoum, M.W. and T. El-Raghy, *Room temperature ductile carbides.* Metallurgical and Materials Transactions, 1999. **30A**: p. 363-369.

52. Barsoum, M.W. and M. Radovic, *Mechanical properties of the MAX phases*, in *Encyclopedia of Materials: Science and Technology*, K.H.J. Buschow, et al., Editors. 2004, Elsevier: Oxford. p. 1-16.

53. El-Raghy, T. and M.W. Barsoum, *Diffusion kinetics of the carburization and silicidation of Ti_3SiC_2.* Journal of Applied Physics, 1998. **83**(1): p. 112-119.

54. Barsoum, M.W., et al., *The topotactic transformation of Ti_3SiC_2 into a partially ordered cubic $Ti(C_{0.67}Si_{0.06})$ phase by the diffusion of Si into molten cryolite.* Journal of the Electrochemical Society, 1999. **146**(10): p. 3919-3923.

55. El-Raghy, T., M.W. Barsoum, and M. Sika, *Reaction of Al with Ti_3SiC_2 in the 800-1000 degrees C temperature range.* Materials Science and Engineering a-Structural Materials Properties Microstructure and Processing, 2001. **298**(1-2): p. 174-178.

56. Gogotsi, Y., et al., *Nanoporous carbide-derived carbon with tunable pore size.* Nature Materials, 2003. **2**(9): p. 591-594.

57. Yushin, G., et al., *Mesoporous carbide-derived carbon with porosity tuned for efficient adsorption of cytokines.* Biomaterials, 2006. **27**(34): p. 5755-5762.

58. Tzenov, N.V. and M.W. Barsoum, *Synthesis and characterization of Ti_3AlC_2.* Journal of the American Ceramic Society, 2000. **83**(4): p. 825-832.

59. Pietzka, M. and J. Schuster, *Summary of constitutional data on the Aluminum-Carbon-Titanium system.* Journal of Phase Equilibria, 1994. **15**(4): p. 392-400.

60. Presser, V., et al., *First-order Raman scattering of the MAX phases: Ti_2AlN, $Ti_2AlC_{0.5}N_{0.5}$, Ti_2AlC, $(Ti_{0.5}V_{0.5})_2AlC$, V_2AlC, Ti_3AlC_2, and Ti_3GeC_2.* Journal of Raman Spectroscopy, 2012. **43**(1): p. 168-172.

61. Rao, C.N.R. and et al., *A study of the synthetic methods and properties of graphenes.* Science and Technology of Advanced Materials, 2010. **11**(5): p. 054502.

62. Schmidt, M. and S.G. Steinemann, *XPS studies of amino acids adsorbed on titanium dioxide surfaces.* Fresenius' Journal of Analytical Chemistry, 1991. **341**(5): p. 412-415.

63. Naguib, M., et al., *Two-dimensional transition metal carbides.* ACS Nano, 2012.

64. Kurtoglu, M., et al., *First principles study of two-dimensional early transition metal carbides.* MRS Communications, 2012. **2**(04): p. 133-137.

65. Viculis, L.M., J.J. Mack, and R.B. Kaner, *A chemical route to carbon nanoscrolls.* Science, 2003. **299**(5611): p. 1361-1361.

66. Savoskin, M.V., et al., *Carbon nanoscrolls produced from acceptor-type graphite intercalation compounds.* Carbon, 2007. **45**(14): p. 2797-2800.

67. Enyashin, A.N. and A.L. Ivanovskii, *Atomic structure, comparative stability and electronic properties of hydroxylated Ti_2C and Ti_3C_2 nanotubes.* Computational and Theoretical Chemistry, 2012. **989**: p. 27-32.

68. M. Khazaei, et al., *Novel electronic and magnetic properties of two-dimensional transition metal carbides and nitrides.* Advanced Functional Materials, 2013. **23** (17): p. 2185-2192.

69. Granroth, G.E., et al., *SEQUOIA: A newly operating chopper spectrometer at the SNS.* Journal of Physics: Conference Series, 2010. **251**(1): p. 012058.

70. Klein, M.V., J.A. Holy, and W.S. Williams, *Raman scattering induced by carbon vacancies in TiC.* Physical Review B, 1978. **17**(4): p. 1546-1556.

71. Bergmann, K. and C.T. O'Konski, *A spectroscopic study of methylene blue monomer, dimer, and complexes with montmorillonite.* Journal of Physical Chemistry, 1963. **67**(10): p. 2169-2177.

72. *Optical absorption of methylene blue*. by Scott Prahl, Oregon Medical Laser Center; Available from: http://omlc.org/spectra/mb/.

73. Rappe, A.K., et al., *UFF, a full periodic-table force-field for molecular mechanics and molecular-dynamics simulations.* Journal of the American Chemical Society, 1992. **114**(25): p. 10024-10035.

74. Naguib, M., et al., *Two-dimensional nanocrystals produced by exfoliation of Ti_3AlC_2.* Advanced Materials, 2011. **23**(37): p. 4248-4253.

75. Mashtalir, O., et al., *Kinetics of aluminum extraction from Ti3AlC2 in hydrofluoric acid.* Materials Chemistry and Physics, 2013. **139**(1): p. 147-152.

76. Naguib, M., et al., *MXene: A promising transition metal carbide anode for lithium-ion batteries.* Electrochemistry Communications, 2012. **16**(1): p. 61-64.

77. McAllister, M.J., et al., *Single sheet functionalized graphene by oxidation and thermal expansion of graphite.* Chemistry of Materials, 2007. **19**(18): p. 4396-4404.

78. Wang, X.R., S.M. Tabakman, and H.J. Dai, *Atomic layer deposition of metal oxides on pristine and functionalized graphene.* Journal of the American Chemical Society, 2008. **130**(26): p. 8152-+.

79. Xiao, J., et al., *Hierarchically porous graphene as a lithium-air battery electrode.* Nano Letters, 2011. **11**(11): p. 5071-5078.

80. Gogotsi, Y., et al., *Graphite polyhedral crystals.* Science, 2000. **290**(5490): p. 317-320.

81. Murayama, H. and T. Maeda, *A novel form of filamentous graphite.* Nature, 1990. **345**(6278): p. 791-793.

82. Rotkin, S.V. and Y. Gogotsi, *Analysis of non-planar graphitic structures: From arched edge planes of graphite crystals to nanotubes.* Materials Research Innovations, 2002. **5**(5): p. 191-200.

83. Pinsker, Z.G.e., *Dynamical scattering of X-rays in crystals*. Vol. 3. 1978: Springer-Verlag Berlin.

84. Mittelbach, P. and G. Porod, Acta Physica Austriaca, 1961. **14**: p. 185-211.

85. Wilhelmsson, O., et al., *Deposition and characterization of ternary thin films within the Ti-Al-C System by DC magnetron sputtering.* Journal of Crystal Growth, 2006. **291**(1): p. 290-300.

86. Myhra, S., J.A.A. Crossley, and M.W. Barsoum, *Crystal-chemistry of the Ti_3AlC_2 and Ti_4AlN_3 layered carbide/nitride phases - Characterization by XPS.* J. Phys. Chem. Solids, 2001. **62**(4): p. 811-817.

87. Mashtalir, O., et al., *Intercalation and delamination of layered carbides and carbonitrides.* Nature Communications, 2013. **4**: p. 1716.

88. Shi, C., et al., *Structure of Nanocrystalline Ti_3C_2 MXene using atomic pair distribution function.* Physical Review Letters, 2014. **112**(12).

89. Lukatskaya, M.R., et al., *Cation intercalation and high volumetric capacitance of two-dimensional titanium carbide.* Science, 2013. **341**(6153): p. 1502-1505.

90. Mashtalir, O., et al., *Dye adsorption and decomposition on two-dimensional titanium carbide in aqueous media.* Journal of Materials Chemistry A, 2014.

91. Langmuir, I., *The constitution and fundamental properties of solids and liquids. Part I. Solids.* Journal of the Americal Chemical Society, 1916. **38**(11): p. 2221-2295.

92. Hall, K.R., et al., *Pore- and solid-diffusion kinetics in fixed-bed adsorption under constant-pattern conditions.* Industrial & Engineering Chemistry Fundamentals, 1966. **5**(2): p. 212-223.

93. Freundlich, H., *Colloid & capillary chemistry*. 1922, New York, NY, USA: E.P. Dutton & Co. 883.

94. Rafatullah, M., et al., *Adsorption of methylene blue on low-cost adsorbents: A Review.* Journal of Hazardous Matererials, 2010. **177**(1-3): p. 70-80.

95. Ghosh, D. and K.G. Bhattacharyya, *Adsorption of methylene blue on kaolinite.* Applied Clay Science, 2002. **20**(6): p. 295-300.

96. Almeida, C.A.P., et al., *Removal of methylene blue from colored effluents by adsorption on montmorillonite clay.* Journal of Colloid and Interface Science, 2009. **332**(1): p. 46-53.

97. Bradder, P., et al., *Dye adsorption on layered graphite oxide.* Journal of Chemical and Engineering Data, 2011. **56**(1): p. 138-141.

98. Liu, P. and L.X. Zhang, *Adsorption of dyes from aqueous solutions or suspensions with clay nano-adsorbents.* Separation and Purification Technology, 2007. **58**(1): p. 32-39.

99. Hang, P.T. and G.W. Brindley, *Methylene blue absorption by clay minerals. determination of surface areas and cation exchange capacities (Clay-Organic Studies XVIII).* Clays Clay Minerals, 1970. **18**(4): p. 203-212.

100. Nakata, K. and A. Fujishima, *TiO_2 Photocatalysis: Design and applications.* Journal of Photochemistry and Photobiology C: Photochemistry Reviews, 2012. **13**(3): p. 169-189.

101. Houas, A., et al., *Photocatalytic degradation pathway of methylene blue in water.* Applied Catalysis B: Environmental, 2001. **31**(2): p. 145-157.

102. Stewart, T.A., M. Nyman, and M.P. deBoer, *Delaminated titanate and peroxotitanate photocatalysts.* Applied Catalysis B, 2011. **105**(1–2): p. 69-76.

103. Zhang, D.Q., G.S. Li, and J.C. Yu, *Inorganic materials for photocatalytic water disinfection.* Journal of Materials Chemistry, 2010. **20**(22): p. 4529-4536.

104. Halim, J., et al., *Transparent conductive two-dimensional titanium carbide epitaxial thin films.* Chemistry of Materials, 2014. **26**(7): p. 2374-2381.

105. Štengl, V., D. Popelková, and P. Vláčil, *TiO_2–graphene nanocomposite as high performace photocatalysts.* The Journal of Physical Chemistry C, 2011. **115**(51): p. 25209-25218.

106. Jiang, G., et al., *TiO_2 nanoparticles assembled on graphene oxide nanosheets with high photocatalytic activity for removal of pollutants.* Carbon, 2011. **49**(8): p. 2693-2701.

107. Fan, W., et al., *Nanocomposites of TiO_2 and reduced graphene oxide as efficient photocatalysts for hydrogen evolution.* The Journal of Physical Chemistry C, 2011. **115**(21): p. 10694-10701.

108. Wang, D., et al., *Self-assembled TiO_2–graphene hybrid nanostructures for enhanced Li-Ion insertion.* ACS Nano, 2009. **3**(4): p. 907-914.

109. Petkov, V., et al., *High real-space resolution measurement of the local structure of $Ga_{1-x}In_xAs$ using X-ray diffraction.* Physical Review Letters, 1999. **83**(20): p. 4089-4092.

110. Jeong, I.K., et al., *Local structure of $In_xGa_{1-x}As$ semiconductor alloys by high-energy synchrotron X-ray diffraction.* Physical Review B, 2001. **63**(20): p. 205202.

111. Park, S., et al., *Colloidal suspensions of highly reduced graphene oxide in a wide variety of organic solvents.* Nano Letters, 2009. **9**(4): p. 1593-1597.

112. Ledoux, R.L. and J.L. White, *Infrared studies of hydrogen bonding interaction between kaolinite surfaces and intercalated potassium acetate, hydrazine, formamide, and urea.* Journal of Colloid and Interface Science, 1966. **21**(2): p. 127-152.

113. Costanzo, P.M. and R.F. Giese, *Ordered and disordered organic intercalates of 8.4-Å synthetically hydrated kaolinite.* Clays and Clay Minerals, 1990. **38**(2): p. 160-170.

114. Boufatit, M., H. Ait-Amar, and W.R. Mc Whinnie, *Development of an algerian material montmorillonite clay - Intercalation with selective long chain alkylammonium cations (Octadecytrimethylammonium, Cetylpyridium and Tetrabutylammonium) and with tellerium complexes.* Desalination, 2008. **223**(1-3): p. 366-374.

115. Frost, R.L., et al., *Complexity of intercalation of hydrazine into kaolinite - A controlled rate thermal analysis and DRIFT spectroscopic study.* Journal of Colloid and Interface Science, 2002. **251**(2): p. 350-359.

116. Johnston, C.T. and D.A. Stone, *Influence of hydrazine on the vibrational modes of kaolinite.* Clays and Clay Minerals, 1990. **38**(2): p. 121-128.

117. Frost, R.L., et al., *Role of water in the intercalation of kaolinite with hydrazine.* Journal of Colloid and Interface Science, 1998. **208**(1): p. 216-225.

118. Frost, R.L., et al., *Deintercalation of hydrazine-intercalated low-defect kaolinite.* Clays and Clay Minerals, 1999. **47**(6): p. 732-741.

119. Deng, Y.J., J.B. Dixon, and G.N. White, *Molecular configurations and orientations of hydrazine between structural layers of kaolinite.* Journal of Colloid and Interface Science, 2003. **257**(2): p. 208-227.

120. Barrios, J., et al., *Qualitative and quantitative study of stacking faults in a hydrazine treated kaolinite - relationship with infrared spectra.* Clays and Clay Minerals, 1977. **25**(6): p. 422-429.

121. Shioyama, H. and T. Akita, *A new route to carbon nanotubes.* Carbon, 2003. **41**(1): p. 179-181.

122. Olejnik, S., A. Posner, and J. Quirk, *The intercalation of polar organic compounds into kaolinite.* Clay Minerals, 1970. **8**(4): p. 421-434.

123. Ling, Z., et al., *Flexible and conductive MXene films and nanocomposites with high capacitance.* Proceedings of the National Academy of Sciences, 2014. **111**(47): p. 16676–16681.

124. Kerker, M., *The scattering of light, and other electromagnetic radiation*. 1969: Academic Press.

125. Mashtalir, O., et al., *Amine-assisted delamination of Nb_2C MXene for Li-ion energy storage devices.* Advanced Materials, 2015. **27**(23): p. 3501–3506.

126. Pedraza, F. and A. Vazquez, *Obtention of TiO_2 rutile at room temperature through direct oxidation of $TiCl_3$.* Journal of Physics and Chemistry of Solids, 1999. **60**(4): p. 445-448.

127. Chen, Y.J. and D.D. Dionysiou, *Effect. of calcination temperature on the photocatalytic activity and adhesion of TiO_2 films prepared by the P-25 powder-modified sol-gel method.* Journal of Molecular Catalysis a-Chemical, 2006. **244**(1-2): p. 73-82.

128. Lee, W.G., et al., *Preparation and properties of amorphous TiO_2 thin-films by plasma-enhanced chemical-vapor-deposition.* Thin Solid Films, 1994. **237**(1-2): p. 105-111.

129. Shimada, S. and M. Kozeki, *Oxidation of TiC at low-temperatures.* Journal of Materials Science, 1992. **27**(7): p. 1869-1875.

130. Yamamoto, S., et al., *In situ X-ray photoelectron spectroscopy studies of water on metals and oxides at ambient conditions.* Journal od Physics: Condensed Matter, 2008. **20**(18): p. 184025.

131. Gan, L.Y., D. Huang, and U. Schwingenschlogl, *Oxygen adsorption and dissociation during the oxidation of monolayer Ti_2C.* Journal of Materials Chemistry A, 2013. **1**(43): p. 13672-13678.

132. Lira, E., et al., *The importance of bulk Ti^{3+} defects in the oxygen chemistry on titania surfaces.* Journal of the American Chemical Society, 2011. **133**(17): p. 6529-6532.

133. Avgustinik, A.I., G.V. Drozdetskaya, and S.S. Ordan'yan, *Reaction of titanium carbide with water.* Soviet Powder Metallurgy and Metal Ceramics, 1967. **6**(6): p. 470-473.

134. Ghassemi, H., et al., *In situ environmental transmission electron microscopy study of oxidation of two-dimensional Ti_3C_2 and formation of carbon-supported TiO_2.* Journal of Materials Chemistry A, 2014. **2**(35): p. 14339.

135. Naguib, M., et al., *One-step synthesis of nanocrystalline transition metal oxides on thin sheets of disordered graphitic carbon by oxidation of MXenes.* Chemical communications (Cambridge, England), 2014. **50**(56): p. 7420-3.

136. Mashtalir, O., et al., *Intercalation and delamination of layered carbides and carbonitrides.* Nature Communications, 2013. **4**: p. 1716.

137. Levchenko, A.A., et al., *Dynamics of water confined on a TiO_2 (anatase) surface.* The Journal of Physical Chemistry A, 2007. **111**(49): p. 12584-12588.

138. Spencer, E.C., et al., *Inelastic neutron scattering study of confined surface water on rutile nanoparticles.* The Journal of Physical Chemistry A, 2009. **113**(12): p. 2796-2800.

139. Kumar, N., et al., *Hydrogen bonds and vbrations of water on (110) rutile.* The Journal of Physical Chemistry C, 2009. **113**(31): p. 13732-13740.

140. Wang, H.-W., et al., *Vibrational density of states of strongly H-bonded interfacial water: Insights from inelastic neutron scattering and theory.* The Journal of Physical Chemistry C, 2014. **118**(20): p. 10805-10813.

141. Tipton, T., et al., *Experimental and theoretical studies of the infrared spectra of hydrazines: N_2H_4, N_2H_3D, $N_2H_2D_2$, N_2HD_3, and N_2D_4.* The Journal of Physical Chemistry, 1989. **93**(8): p. 2917-2927.

142. Raja, C., et al., *High pressure spectroscopic studies of hydrazine (N_2H_4).* Journal of Physics: Conference Series, 2014. **500**(5): p. 052008.

143. Yang, G.Y., et al., *TG-DTG analysis of chemically bound moisture removal of $AlF_3 \cdot 3H_2O$.* Drying Technology, 2007. **25**(4): p. 675-680.

144. Cygan, R.T., J.J. Liang, and A.G. Kalinichev, *Molecular models of hydroxide, oxyhydroxide, and clay phases and the development of a general force field.* Journal of Physical Chemistry B, 2004. **108**(4): p. 1255-1266.

145. Shein, I.R. and A.L. Ivanovskii, *Graphene-like titanium carbides and nitrides $Ti_{n+1}C_n$, $Ti_{n+1}N_n$ (n=1, 2, and 3) from de-intercalated MAX phases: First-principles probing of their structural, electronic properties and relative stability.* Computational Materials Science, 2012. **65**: p. 104-114.

146. Kline, S., *Reduction and analysis of SANS and USANS data using IGOR Pro.* Journal of Applied Crystallography, 2006. **39**(6): p. 895-900.

147. Chupas, P.J., et al., *Rapid-acquisition pair distribution function (RA-PDF) analysis.* Journal of Applied Crystallography, 2003. **36**: p. 1342-1347.

148. Hammersley, A., et al., *Two-dimensional detector software: from real detector to idealised image or two-theta scan.* International Journal of High Pressure Research, 1996. **14**(4-6): p. 235-248.

149. Juhas, P., et al., *PDFgetX3: a rapid and highly automatable program for processing powder diffraction data into total scattering pair distribution functions.* Journal of Applied Crystallography, 2013. **46**: p. 560-566.

150. Egami, T. and S.J. Billinge, *Underneath the Bragg peaks: structural analysis of complex materials*. Vol. 16. 2003: Elsevier.

151. Proffen, T. and S.J.L. Billinge, *PDFFIT, a program for full profile structural refinement of the atomic pair distribution function.* Journal of Applied Crystallography, 1999. **32**: p. 572-575.

152. Farrow, C.L., et al., *PDFfit2 and PDFgui: computer programs for studying nanostructure in crystals.* Journal of Physics-Condensed Matter, 2007. **19**(33).

VITA

Olha Mashtalir • o.mashtalir@gmail.com

EDUCATION

Drexel University (Philadelphia, PA, USA):
PhD in Materials Science and Engineering, 01/2011 – 06/2015 GPA: 3.99

National University of Kyiv-Mohyla Academy (Kyiv, Ukraine):
MS in Chemistry , 09/2005 – 06/2007
BS in Chemistry, 09/2001 – 06/2005

AWARDS/HONORS

- Best Poster Award, 6th PCGMR-NCKU Symposium "Nano-Technology/Materials for Future Devices, BioMedical Applications", Taiwan, 2014.
- Graduate Student Award, E-MRS Spring Meeting, Lille, France, 2014.
- 2014 JALA Top-Ten Honoree
- Ross Coffin Purdy Award 2013

PUBLICATIONS

- **O Mashtalir**, *et al.*, Structural Studies and High Rate Supercapacitor Performance of the Hydrazine Intercalated Two Dimensional Titanium Carbide, 2015. [in preparation]
- **O Mashtalir**, MR Lukatskaya, M-Q Zhao, MW Barsoum, Y Gogotsi, Amine Assisted Delamination of Nb_2C MXene for Li-Ion Energy Storage Devices, *Advanced Materials*, 2015, 27(23), 3501
- M-Q Zhao, M Sedran, Z Ling, **O Mashtalir**, M Ghidiu, B Dyatkin, MW Barsoum, Y Gogotsi, Synthesis of Carbon/Sulfur Nanolaminates by Electrochemical Extraction of Titanium from Ti_2SC, *Angewandte Chemie International Edition*, 2015, 54(16), 4810.
- **O Mashtalir**, KM Cook, VN Mochalin, M Crowe, MW Barsoum, Y Gogotsi, Dye Adsorption and Decomposition on Two-Dimensional Titanium Carbide in Aqueous Media, *Journal of Materials Chemistry A*, 2014, 2(35), 14334.
- H Ghassemi, W Harlow, **O Mashtalir**, M Beidaghi, MR Lukatskaya, Y Gogotsi, ML Taheri, *In Situ* Environmental Transmission Electron Microscopy Study of Oxidation of Two-Dimensional Ti_3C_2 and Formation of Carbon-Supported TiO_2, *Journal of Materials Chemistry A*, 2014, 2(35), 14339.
- M Ghidiu, M Naguib, C Shi, **O Mashtalir**, LM Pan, B Zhang, J Yang, Y Gogotsi, SJL Billinge, MW Barsoum, Synthesis and Characterization of Two-Dimensional Nb_4C_3 (MXene), *Chemical Communications*, 2014, 50 (67), 9517.
- M Naguib, **O Mashtalir**, MR Lukatskaya, B Dyatkin, C Zhang, V Presser, Y Gogotsi, MW Barsoum, One-step synthesis of nanocrystalline transition metal oxides on thin sheets of disordered graphitic carbon by oxidation of MXenes, *Chemical Communications*, 2014, 50, 7420.
- C Shi, M Beidaghi, M Naguib, **O Mashtalir**, Y Gogotsi, SJL Billinge, Structure of Nanocrystalline Ti_3C_2 MXene Using Atomic Pair Distribution Function, *Physical Review Letters*, 2014, 112 (12), 125501.
- Y Yu, JM Noël, MV Mirkin, Y Gao, **O Mashtalir**, G Friedman, Y Gogotsi, Carbon Pipette-Based Electrochemical Nanosampler, *Analytical Chemistry*, 2014, 86 (7), 3365
- MR Lukatskaya, **O Mashtalir**, CE Ren, Y Dall'Agnese, P Rozier, PL Taberna, M Naguib, P Simon, MW Barsoum, Y Gogotsi, Cation Intercalation and High Volumetric Capacitance of Two-Dimensional Titanium Carbide, *Science*, 2013, 341 (6153), 1502
- **O Mashtalir**, M Naguib, VN Mochalin, Y Dall'Agnese, M Heon, MW Barsoum, Y Gogotsi, Intercalation and Delamination of Layered Carbides and Carbonitrides, *Nature Communications*, 2013, 4, 1716.
- **O Mashtalir**, M Naguib, B Dyatkin, Y Gogotsi, MW Barsoum, Kinetics of Aluminum Extraction From Ti_3AlC_2 in Hydrofluoric Acid, *Materials Chemistry and Physics* 2013, 139 (1), 147.
- P Ruvinskiy, IV Barsukov, **O Mashtalir**, CM Reid, JJ Wu, Y Gogotsi, Nano-Silicon Containing Composite Graphitic Anodes with Improved Cycling Stability for Application in High Energy Lithium-Ion Batteries, *ECS Journal of Solid State Science and Technology*, 2013, 2 (10), M3028.
- **O Mashtalir**, M Kurtoglu, S Pogulay, A Gogotsi, M Naguib, Y Gogotsi, Photocatalytic WO_3 and TiO_2 Films on Brass, *International Journal of Applied Ceramic Technology*, 2013, 10 (1), 26.

M Naguib, **O Mashtalir**, J Carle, V Presser, J Lu, L Hultman, Y Gogotsi, MW Barsoum, Two-Dimensional Transition Metal Carbide, *ACS Nano*, 2012, 6 (2), 1322.